Technical Report
TR-19-11
November 2019

Bentonite homogenisation

Laboratory study, model development and modelling of homogenisation processes

Ann Dueck
Lennart Börgesson
Ola Kristensson
Daniel Malmberg
Mattias Åkesson
Jan Hernelind

SVENSK KÄRNBRÄNSLEHANTERING AB

SWEDISH NUCLEAR FUEL
AND WASTE MANAGEMENT CO

Box 3091, SE-169 03 Solna
Phone +46 8 459 84 00
skb.se

SVENSK KÄRNBRÄNSLEHANTERING

ISSN 1404-0344
SKB TR-19-11
ID 1704165
November 2019

Bentonite homogenisation

Laboratory study, model development and modelling of homogenisation processes

Ann Dueck, Lennart Börgesson, Ola Kristensson,
Daniel Malmberg, Mattias Åkesson
Clay Technology AB

Jan Hernelind, Scanscot Technology AB

Abstract

Swelling and homogenization of bentonite materials are important functions of the bentonite to fulfill the requirements of the buffer in a deposition hole and the backfill in the tunnels after full water saturation. It is important to understand and be able to predict the final condition of the bentonite after the swelling and homogenization, which occurs both during the initial saturation and homogenisation of the blocks and pellets and also after possible loss of bentonite caused by for example erosion. How well the bentonite self-seals and homogenises have been studied in this project. The study has included a laboratory testing programme with tests at different scales and complexity, analyses of the results with different material models and calculation tools, evaluation of mechanical parameters for the material models and also development of a new hydro-mechanical bentonite material model.

In this report the test results from fundamental laboratory tests in smaller scale have been compiled and analysed. The results show that still after a long time and with negligible changes in stress, density gradients remained, and that they were influenced by time, water pressure and initial density distribution. The results also show that the average stress and the average density after swelling agree well with the expected relationships from constant volume swelling pressure tests. The laboratory test results also show that friction between bentonite and a raw steel surface, evaluated as a friction angle at peak stress, agree well with a model of the bentonite internal friction angle and that the corresponding friction angle when more smooth surfaces were used yielded lower values.

The FE-program Abaqus has been used to model three very different types of homogenisation tests with two different mechanical material models. The models have the same porous elastic model for simulating the non-linear isotropic elastic part of the swelling and compression of bentonite, but they have different plastic models for simulating the effect of deviatoric stresses. The Drucker-Prager model is a classic material model included in the model library of Abaqus. The other model (Claytech Plastic Cap model) has been implemented in Abaqus.

At first some tests with only axial or radial swelling were modelled to check the models and calibrate the parameters of the models. Both these tests were very well modelled with the Cap model but less good with the Drucker-Prager model. However, the models did not work well for the extreme scenarios of pure isotropic swelling and closing of a circular cavity.

The Cap Model was then used to model (true prediction) the Self-healing Test SH1 in larger scale and with complicated geometry, which included homogenisation of a large bentonite block with two cavities. The calculation worked well but the model underestimated the self-healing ability by yielding too high void ratio (20 %) and thereby logically too low stresses (40 %) in the former cavity. The Drucker-Prager plastic model captured the void ratio distribution better (although still a little too high) but also this model yielded the same too low stresses in the cavity.

Ten almost identical tests of the homogenisation of bentonite with large density difference placed in long tubes with raw grooved inner surfaces have been running for 4–5 years, with the purpose to study the long term homogenisation process. One of those has been terminated and sampled. The results showed that the homogenisation process can be well modelled with remaining unaffected initial densities at both ends of the tube, if the average residual friction angle evaluated from friction tests is used.

An important conclusion from these tests and calculations is that it is the residual friction angle (in these cases with the average value $\phi = 7.2°$) and not the peak value that is valid between a bentonite and a surface even when the surface is so raw that the slip takes place in the bentonite itself.

A new hydro-mechanical (HM) material model, intended for bentonite-based components, has been developed and implemented into the COMSOL Multiphysics platform. When evaluating and testing the HM-model performance by using laboratory experiments within this project, it was found that the model response agreed well with experimental data. However, the new material model is in its initial state of development and more work remains to make it general.

Sammanfattning

Svällning och homogenisering av bentonitmaterial är viktiga egenskaper för att kunna garantera att bufferten i deponeringshålen och återfyllningsmaterialet i tunnlarna uppfyller uppställda krav efter full vattenmättnad. Det är viktigt att förstå och kunna prediktera sluttillståndet hos bentoniten efter svällning och homogenisering, som sker både under den ursprungliga vattenmättnaden och homogeniseringen av block och pellets och även efter möjliga förluster av bentonit som orsakats t ex av erosion. Hur väl bentonitmaterial kan självläka och homogenisera har studerats i detta projektet. Studien har inkluderat ett laboratorieprogram med försök i olika skala och komplexitet, analyser av försöksresultaten med olika materialmodeller och beräkningsredskap, utvärdering av mekaniska parametrar till materialmodellerna och även utveckling av en ny hydro-mekanisk bentonit-material-modell.

I denna rapport har resultat från de grundläggande laboratorieförsöken i mindre skala sammanställts och analyserats. Resultaten visar att trots långa försökstider och inga eller små förändringar i uppmätta spänningar, fanns kvarstående densitetsgradienter som dock påverkades av tid, vattentryck och densitetsfördelning vid start. Resultaten visar också att medelspänning och medeldensitet efter svällning överensstämmer med motsvarande samband för svälltryck som bestämts från försök där volymen varit konstant. Resultaten från laboratorieförsöken visar också att friktionen mellan bentonit och en rå stålyta, utvärderad som friktionsvinkel vid maximal skjuvspänning, överensstämmer väl med en modell för den inre friktionsvinkeln i bentonit och att motsvarande friktionsvinkel för andra plana ytor gav lägre värde.

FE-programmet Abaqus har använts för att modellera tre mycket olika homogeniseringsfall med två olika materialmodeller. Modellerna har samma elsticitetsmodell (Porous Elastic) för att simulera den icke-linjära isotropa elastiska delen av svällningen men olika plasitcitetsmodeller för att simulera effekten av deviatoriska plastiska spänningar. Drucker-Prager är en klassisk materialmodell som finns i Abaqus modellbibliotek medan den andra modellen (Claytech Plastic Cap model) har utvecklats för bentonit och implementerats i Abaqus.

Först modellerades några tester med enbart axiell eller radiell svällning för att kontrollera modellerna och kalibrera materialparametrarna. Båda dessa tester gav mycket god överensstämmelse med mätresultat när Cap-modellen användes men inte så bra med Drucker-Prager. Emellertid, fungerade modellerna mindre bra för de extrema fallen med helt isotrop svällning och igensvällning av ett cirkulärt hål.

Cap-modellen användes sedan för att modellera (true prediction) självläkningsförsöket i större skala med komplicerad geometri SH1, som innebar homogenisering av ett stort bentonitblock med två hålrum. Beräkningen fungerade bra men modellen underskattade självläkningsförmågan något genom att ge för högt portal (20 %) och därmed även för låga spänningar (40 %) i de ursprungliga hålrummen.

Tio nästan identiska försök med homogenisering av bentonit med stor skillnad i ursprunglig densitet placerade i långa rör med råa ytor har pågått i 4–5 år med syfte att studera långtidseffekter av homogenisering. En av dessa försök har avslutats och provtagits. Resultaten visade att homogeniseringen kunde modelleras med god överensstämmelse med opåverkad ursprunglig densitet i båda ändarna av röret, om medelrestfriktionsvinkeln (efter stora förskjutningar) utvärderad från friktionsförsök användes.

En viktig slutsats från dessa försök och beräkningar är att det är restfriktionsvinkeln (i dessa fall med ett medelvärde på $\phi = 7.2^{o}$) mellan bentonit och en rå yta och inte maxvärdet som skall användas även när ytan är så rå att skjuvningen äger rum i själva bentoniten.

Inom projektet har en ny hydro-mekanisk (HM) materialmodell, avsedd för komponenter bestående av bentonit, utvecklats och implementerats i programvaran COMSOL Multiphysics. Utvärdering och tester av den nya modellen visade på att denna överensstämde väl med de experimentella laboratorieexperiment som simulerades. Men den nya materialmodellen befinner sig i början av utvecklingen och mer arbete behövs för att göra den mer generellt användbar.

Contents

1 Introduction

1.1 Background

Swelling of the buffer blocks and buffer homogenization are important functions to guarantee the requirements of the buffer in a deposition hole and the backfill in the tunnels after full water saturation. It is important to understand and be able to predict the final condition of the buffer after the swelling and homogenization, which occurs both during the initial saturation and homogenisation of the blocks and pellets and also after possible loss of bentonite caused by for example erosion.

To increase the knowledge of the homogenisation process an SKB project was initiated and has been running during more than ten years. The project consists of several parts; theoretical studies and modelling, fundamental laboratory swelling tests in small scale (with the height 40–80 mm and the diameter 50–100 mm), laboratory study of the influence of friction, medium scale tests (with the height 100 mm and the diameter 300 mm) of a scenario involving loss of bentonite and long tubes tests with large density gradients.

The first laboratory tests series started in 2008 and in 2016 most test series were completed. The test results referred to in this report have been presented in four status reports; TR-12-02, TR-14-25, TR-16-04 and TR-17-04 (Dueck et al. 2011, 2014, 2016, 2018). In addition, two posters were presented at the conferences on Clays in Natural and Engineered Barriers for Radioactive Waste Confinements in Montpellier 2012 (Gm/Ex/32) and in Brussels 2015 (P-12-04).

Material models have been developed and verified with some of the laboratory test results from this project. Modelling of the bentonite swelling based on and compared to test results from the buffer homogenisation project has been presented by Börgesson et al. (2019) as a part of the SKB project Task Force on Engineered Barriers (TF EBS). Modelling of the bentonite swelling has also been presented as a poster at the conferences on Clays in Natural and Engineered Barriers for Radioactive Waste Confinements in Brussels 2015 (P-12-02).

A new hydro-mechanical material model, denoted the Hysteresis Based Material model (HBM), has been developed and implemented into the COMSOL Multiphysics platform. The work has been carried out within this project and in parallel with the EU project BEACON. Of vital importance for a proper prediction of the mechanical evolution of bentonite is the capability to capture the swelling pressure and the shear strength at different dry densities. The HBM model was based on a body of empirical data, as well as a thermodynamic relation for the chemical potential of the clay water, which means that the fundamental properties (i.e. swelling pressure and shear strength), as well as the hysteresis behaviour, are at the core of the material model and that no parameter value adoption is needed for specific void ratios. As a starting point the model was limited to water saturated conditions and stresses and strains in the principal directions. Laboratory results from this project were used to evaluate and test the performance of the HBM model.

1.2 Objective of the report

The main objective of the laboratory tests made in this project was to provide results that could be used for modelling some well-defined benchmark tests in order to improve the hydro-mechanical models of bentonite materials. The objective with this report is to compile the results and findings of the project, which include 1) pointing out the most important test results from the laboratory tests, 2) evaluation of mechanical parameters for modelling the behaviour of bentonite buffer material, 3) analysing the laboratory test results with the material models and 4) development and implementation of a new hydro-mechanical bentonite material model.

1.3 Content of the report

In Chapter 2 the importance of studying buffer homogenisation in general is described together with the main purpose of the project. In Chapter 3 the fundamental laboratory tests and the friction tests made in the project are briefly described and some important results and comments are presented. In Chapter 4 analyses of some of the more complex laboratory tests are made with existing models, mainly a material model implemented in Abaqus. The new hydro-mechanical bentonite material model is presented in Chapter 5 together with the implementation in COMSOL and model evaluation using some of the fundamental laboratory tests from this project. In Chapter 6 conclusions regarding buffer homogenisation and the models used for the analyses are given.

2 Studies of the homogenisation process

Gaps, holes or inhomogeneous density distributions may be present in the buffer or backfill material due to loss of bentonite material by piping and erosion during the installation and saturation phases or by colloid erosion during glacial groundwater conditions. Heterogeneous initial conditions prevail due to installation techniques with blocks with gaps between them, gaps filled with pellets, and mechanical interaction between e.g. buffer/backfill. How well the bentonite self-seals and homogenises has been studied in this project. The laboratory tests have mainly been made on specimens that have been water saturated or close to water saturated from start, which means that the saturation process has not been included in the tests.

The purposes of the homogenisation project and the tests have been to:

- Understand how homogenisation evolves and ends.
- Investigate the different factors influencing homogenisation.
- Understand how much inhomogeneity remains within the bentonite.
- Be a base for creating hydro-mechanical models for the homogenisation process.
- Evaluate models, model parameters and modelling tools.

The laboratory tests made in this project have been divided into four parts:

- Fundamental swelling tests to increase the knowledge about material parameters.
- Measurement of friction between bentonite and other surfaces.
- Homogenisation after loss of bentonite in the self-healing tests.
- Homogenisation in long tubes where the effect of time can also be studied.

The modelling related to the laboratory test results from this project has included comparison with measured results and has mainly been concentrated on:

- Evaluation of models and model parameters and verification of the models by modelling the fundamental swelling tests.
- Modelling of one of the self-healing tests.
- Analyses and modelling of one test from the series with long tubes.

The development of a new hydro-mechanical bentonite material model can be described as:

- Theoretical development of a basic model and generalization of this.
- Reformulation to a format suitable for implementation into COMSOL Multiphysics and writing of the c-code containing the implementation.
- Testing and evaluation of the implementation.

3 Laboratory tests

3.1 Introduction

In the previous reports on laboratory test results from this project different test types have been described and the test procedure, test series and test results have been presented (Dueck et al. 2011, 2014, 2016, 2018). In those reports some observations and discussions regarding the test results have also been mentioned.

In this chapter, the objective and a brief description of each test type are given together with important results and observations regarding the fundamental laboratory tests and the friction tests.

3.2 Laboratory testing programme – description of tests

Different test types have been used in order to analyse homogenisation from different perspectives:

- Fundamental swelling tests.
- Measurement of friction between bentonite and other surfaces.
- Homogenisation after loss of bentonite – the self-healing tests.
- Homogenisation in long tubes.

The results from the different test types consist of measured stresses during the tests and final distributions of density and water content determined on the specimens after dismantling.

The materials used for the tests have been the bentonites MX-80 (Wyoming bentonite from American Colloid Company) and Calcigel (Bavarian bentonite from Süd-Chemie AG) further described by Karnland et al. (2006) or Svensson et al. (2011). The water supply during saturation and homogenisation consisted of de-ionized water or water with a low salt content. All tests made in this project are compiled in Appendix 1.

3.2.1 The fundamental swelling tests

The fundamental swelling of water saturated bentonite specimens with access to water has been studied in three different test series (Dueck et al. 2011, 2014, 2016, 2018). The principles are illustrated in Figure 3-1:

- Axial swelling in a device with constant radius and limited height and with variation of the height of the gap.
- Radial swelling of the outer surface in a device with constant height and limited radius and with variation of the radial gap.
- Radial swelling into a cylindrical cavity in a device with constant height and radius and with variation of the radius of the cavity.

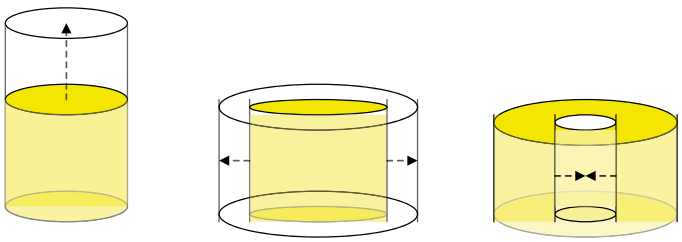

Figure 3-1. *Illustration of the geometry of the test types carried out.*

Tests of this type have been run in two series: the basic-series and the so called HR-series (High Resolution). In the basic-series small specimens with the height 20–40 mm and the diameter 50 mm were used which were saturated in the test device before the subsequent swelling. To improve this test type and to increase the resolution of the results, the HR-series were run with dimensions of the specimens doubled compared to the basic series, i.e. the height was 40–80 mm and the diameter 100 mm. With the larger dimensions the density and stress gradients were possible to study in more detail. The specimens used in the HR-series were basically water saturated at start and no saturation took place in the test device before the swelling. The number of tests of each type are given in Table 3-1 where the swelling s is calculated from the initial dry density ρ_{di} and the final dry density ρ_{df} according to Equation 3-1.

$$s = \frac{\rho_{di}}{\rho_{df}} - 1 \tag{3-1}$$

Table 3-1. Number of tests of each type of the fundamental swelling tests in the Basic and HR-series on MX-80 and Calcigel. All tests from the last three reports are included but only the most important tests from the very first report.

Type of swelling	Swelling s (%)	Basic-series MX-80	Basic-series Calcigel	HR-series MX-80	HR-series Calcigel	Total number
Axial	0–46	7	2	4	3	16
Radial outward	3–45	10	2	1	2	15
Radial inward	3–110	6	2	1	1	10
Swelling in all directions	43			1		1

In addition, so called wetting tests have also been run, where the influence of the location of the water supply on the final distribution of the dry density was studied. In these tests no free volume was present, but the specimens consisted initially of two parts having different densities and the difference between the tests was mainly how the water was supplied. The water was supplied either from the outer surface of the high density part or from the outer surface of the low density part. Three tests were run on Calcigel.

Some of the fundamental swelling tests have been modelled and are further described in Sections 4.2 and 5.4.

3.2.2 Measurement of friction between bentonite and other surfaces

Friction between bentonite and other surfaces has been studied in the friction test series (Dueck et al. 2014, 2016, 2018). In these test series the specimens were saturated with a minimum of swelling in a swelling pressure device consisting of a confining ring, pistons and plates. After saturation was completed the friction tests were run by displacing the bentonite in relation to the confining ring, which had an inner surface prepared in different ways. The tested surfaces were either smooth steel surfaces, steel surfaces with machined grooves, a plastic filter surface or a surface of acrylic plastic. The results were presented as an interpreted friction angle as a function of measured swelling pressure. In these series mainly MX-80 specimens were used (18 tests) but two tests were also run on Calcigel.

3.2.3 Homogenisation after loss of bentonite – the self-healing tests

Buffer homogenisation involving loss of bentonite has been studied by two medium scale laboratory tests, called Self-Healing tests (SH1 and SH2) (Dueck et al. 2016, 2018). A test device with the inner diameter 300 mm and the height 100 mm was used for the tests and a simulated canister with the outer diameter 100 mm was included in the centre. The water was provided to the bentonite from the outer radial surface. In each bentonite block two larger cavities were cut out, in two diametrical positions, to simulate loss of material. In the set-up of SH1 nine transducers for measuring swelling pressure and two for measuring suction were included.

The two tests, SH1 and SH2, had the same boundary conditions and consisted of a block of MX-80 bentonite and they both started in December 2012. The non-instrumented SH2 was finished and dismantled after 17 months, in May 2014, and the instrumented SH1 was finished and dismantled after 33 months, in September 2015. One of the tests has been modelled and is further described in Section 4.3.

3.2.4 Homogenisation in long tubes

Swelling and homogenisation has been studied in 10 tests performed in a series of long tubes with similar design and content (Dueck et al. 2018). The length of the tubes is 250–350 mm and the diameter is 25–35 mm and while the lower half of each tube is filled with highly compacted MX-80 bentonite the upper half is filled with MX-80 pellets. Water is added from the upper end, i.e. above the pellets. Swelling pressure is determined in some of the tests by measuring radial and axial stresses exerted on pistons. By using different test durations before sampling the influence of time and creep on the distribution of density and on the evolution of swelling pressure can be studied. One test was finished after 2 years while nine are still ongoing.

The purpose of this test type is to study the effect of friction for limiting homogenisation and the influence of time on the remaining density gradients after completed swelling and compression. The results can also be applied to evaluate to what extent the so called "transition zones" in tunnels can be used to downshift the swelling pressure against e.g. a plug. One of the tests has been modelled and is further described in Section 4.4.

3.3 Laboratory test results

The discussion in this section is mainly based on test results from the fundamental swelling tests and the friction tests. The discussion is focused on the following:

- Swelling pressure – dry density relation.
- Gradients in dry density after swelling.
- Influence of water pressure.
- Friction angles from measured friction forces.
- Accuracies, uncertainties and limitations.

3.3.1 Swelling pressure – dry density relation

The swelling pressure has been determined as a measured stress on a piston placed axially or radially in contact with a specimen. The final value was measured after completed swelling and equilibrium when no, or only small, changes in pressure with time were seen over a couple of hours or days. The water in equilibrium with the specimens was in the earlier part of the project stagnant water with a pressure of less than 5 kPa while in the later part of the project higher water pressure was applied during shorter time periods and water circulation was used in order to get rid of air bubbles.

An important question is if the average stress and corresponding average density represent the conditions of the buffer after swelling and homogenisation, i.e. to what extent the conditions agree with existing models of swelling pressure. The average stress $P_{average}$ is then calculated from the axial P_{axial} and radial stresses P_{radial} according to Equation 3-2.

$$P_{average} = \frac{P_{axial} + 2 \cdot P_{radial}}{3} \quad (3\text{-}2)$$

In Figure 3-2 the results from the fundamental swelling tests on MX-80 in the basic and the HR-series show that the average stresses after swelling and homogenisation agree well or are slightly higher compared to the model of MX-80 presented by Börgesson et al. (1995) when plotted with the corresponding average dry density. In Figure 3-2 an additional model of MX-80 is also shown, a model presented by Åkesson et al. (2010b) and based on laboratory results from Karnland et al. (2006). Compared to this model the measured swelling pressures are lower. The test results represent swelling mainly between 0 and 50 % but also with a few tests between 90 and 110 %. Test R11-21 is put in brackets since it deviated from the other tests both regarding swelling pressure and density distribution. Since there was some uncertainty of this specimen a similar test was run, R11-22, and the deviating behaviour was not observed from the new test (Dueck et al. 2016).

The results from the same test series but on specimens of Calcigel are plotted in similar diagrams in Figure 3-3 together with a model of a Ca-dominated bentonite presented by Börgesson et al. (2010). Lower swelling pressure is seen on several specimens compared to both the results of MX-80 and

the model. At lower density calcium dominated bentonites (e.g. Calcigel) are expected to have lower swelling pressure compared to sodium dominated bentonites (e.g. MX-80) (Karnland et al. 2006). The results indicate that for the actual condition the swelling pressure of Calcigel are less than that of MX-80 at dry density less than approximately 1 200 kg/m^3.

In Figure 3-2 and Figure 3-3 the markers (circle, diamond) denote the test series (basic-series, HR-series) and the colours (red, yellow, blue) denote the type of swelling (axial, radial outward, radial inward). Marker lines are used for tests on MX-80 and no marker lines denote tests on Calcigel. The results from the different test series are shown in separate diagrams in previous reports (Figures 5-16 to 5-21 in the report by Dueck et al. 2016 and in Figures 4-24 and 4-25 in the report by Dueck et al. 2018).

In Figure 3-2 it can be observed that the average stresses of MX-80 plotted as a function of the average dry densities after swelling and homogenisation are limited to values between the two models shown.

In Figure 3-4 the test results from the HR-series are shown again and in this plot the differences in stresses and densities in each test are marked with bars. For MX-80 correspondence with the solid line is seen when conditions representing the highest dry density and highest measured stress from the tests are considered (i.e. the upper right corner of the square formed by the two bars given for each test) while conditions representing the lowest dry density and the lowest measured stress from each test are located far to the left of the solid line (lower left corner of the square formed by the bars given). This can be interpreted as different parts of the specimens are subjected to different stress paths, i.e. where the former condition corresponds to swelling at unloading the latter corresponds to consolidation at loading.

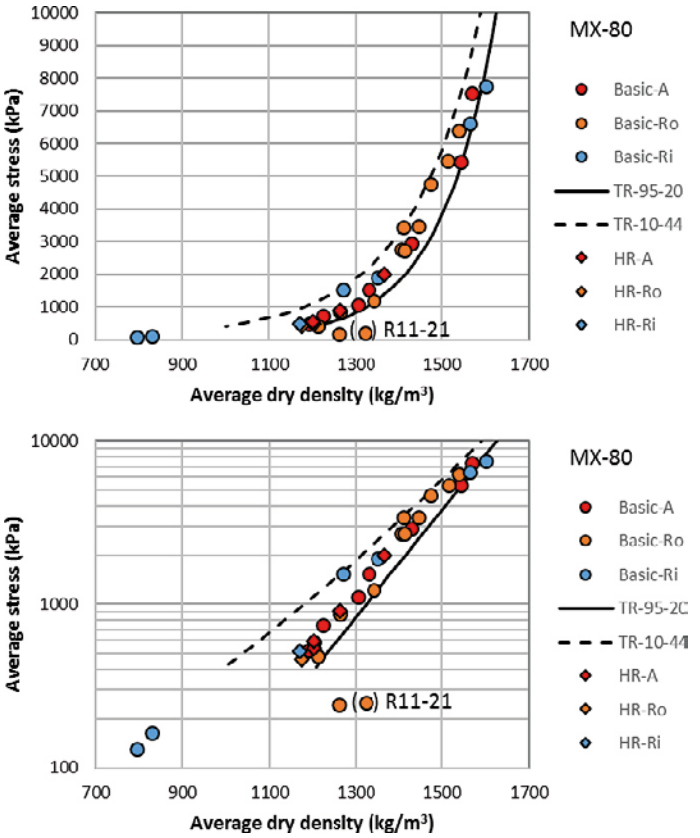

Figure 3-2. *Average stress versus average dry density from almost all tests (i.e. according to Table 3-1) in the basic- and HR-series on MX-80. The results are plotted both with linear (upper) and logarithmic (lower) y-axis. The markers (circle, diamond) denote the test series (basic, HR) and the colours (red, yellow, blue) denote the type of swelling (axial, radial outward, radial inward).*

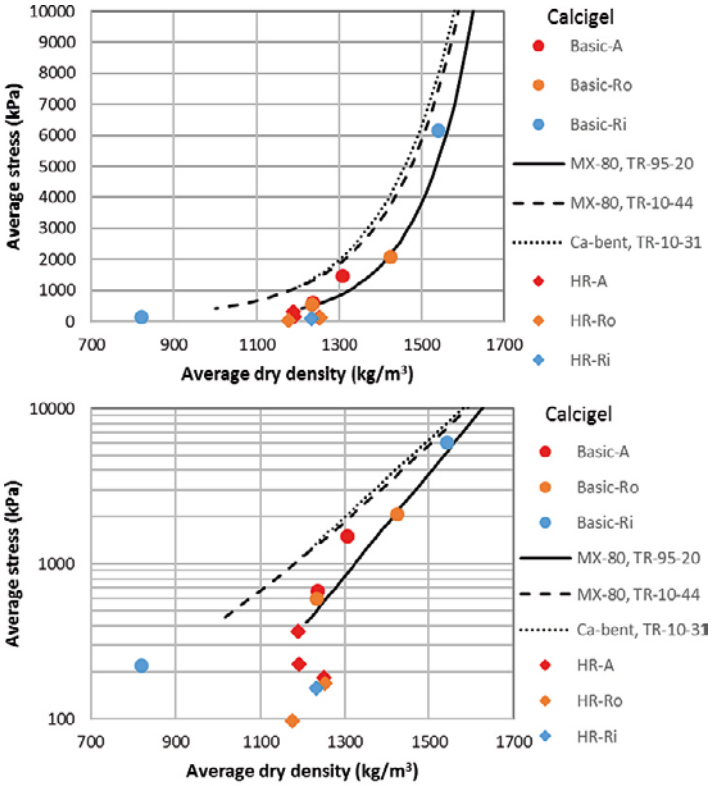

Figure 3-3. *Average stress versus average dry density from all tests in the basic- and HR-series on Calcigel. Models of MX-80 and a Ca-bentonite are also plotted. The results are plotted both with linear (upper) and logarithmic (lower) y-axis. The same markers as in Figure 3-2 are used but without marker lines.*

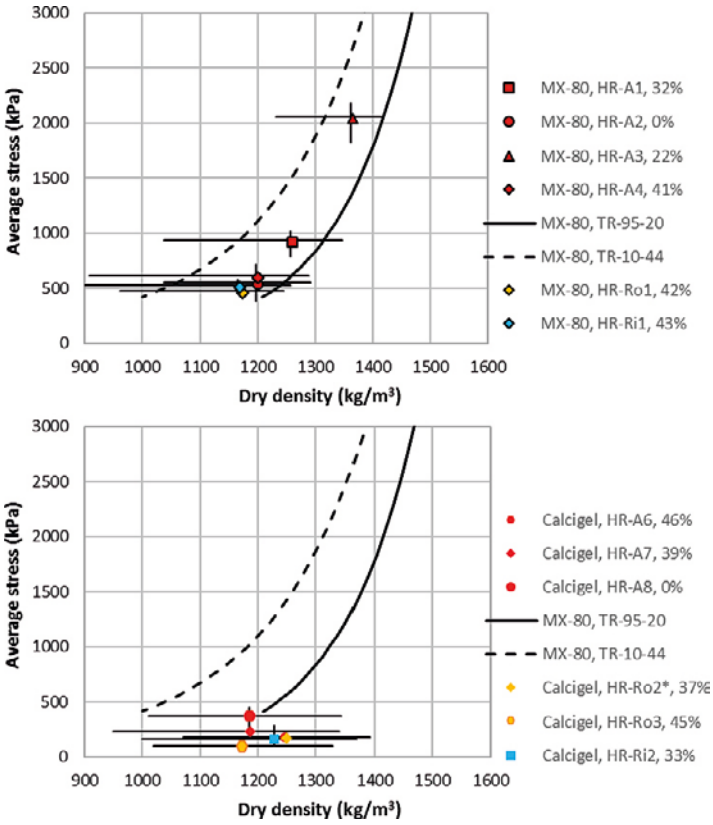

Figure 3-4. *Results from all HR-tests of MX-80 (upper) and Calcigel (lower). The colours denote the type of swelling and the bars show the maximum stresses and dry densities measured in each test. Two models of MX-80 are also shown.*

The dependence of stress paths has been seen earlier in oedometer test (e.g. test KMXAR2 presented by Börgesson et al. 1995) where the density at equilibrium is higher when resulting from unloading, i.e. swelling from a higher stress state, compared to the density resulting from loading, i.e. consolidation from a lower stress state. However, while a specimen in an oedometer test is exposed to either loading or unloading, a specimen exposed to large swelling strains into an open void, as in this project, is exposed to both unloading and later also loading, in some positions, within the same specimen.

The test results could be further studied by considering measured stresses and dry densities determined in specific positions. In Figure 3-5 the radially measured stresses at different levels after axial swelling in the HR-series are plotted as a function of the dry density measured at the corresponding levels, i.e. not the average density. Results from seven tests in the HR-series, four on MX-80 and three on Calcigel, with axial swelling are shown. In addition to the previous used models the results from the HR-series are plotted together with test results from previous studies on MX-80 and constant volume tests in the lower range of stresses (Karnland et al. 2008, Börgesson et al. 1995).

In Figure 3-5 the specimens of Calcigel show swelling pressure less than the model of MX-80 which agree with the results commented above and shown in Figure 3-3 and Figure 3-4.

Most of the measured results on MX-80 from the HR-series correspond to the previous measurements and the solid line in Figure 3-5. However, the three red diamonds with marker lines located at the upper dotted line clearly deviate from the other measurements and all three are measurements from the uppermost position of three HR-A specimens of MX-80 (HR-A1, HR_A2, HR-A4, Dueck et al. 2014, 2016). Thus, the deviating and somewhat extreme stress paths of these three specimens seem to have influenced the final condition. Different paths to saturation, hysteresis effect, is also a possible explanation to the difference between the two models (dotted and solid lines) shown in Figure 3-2 to Figure 3-5.

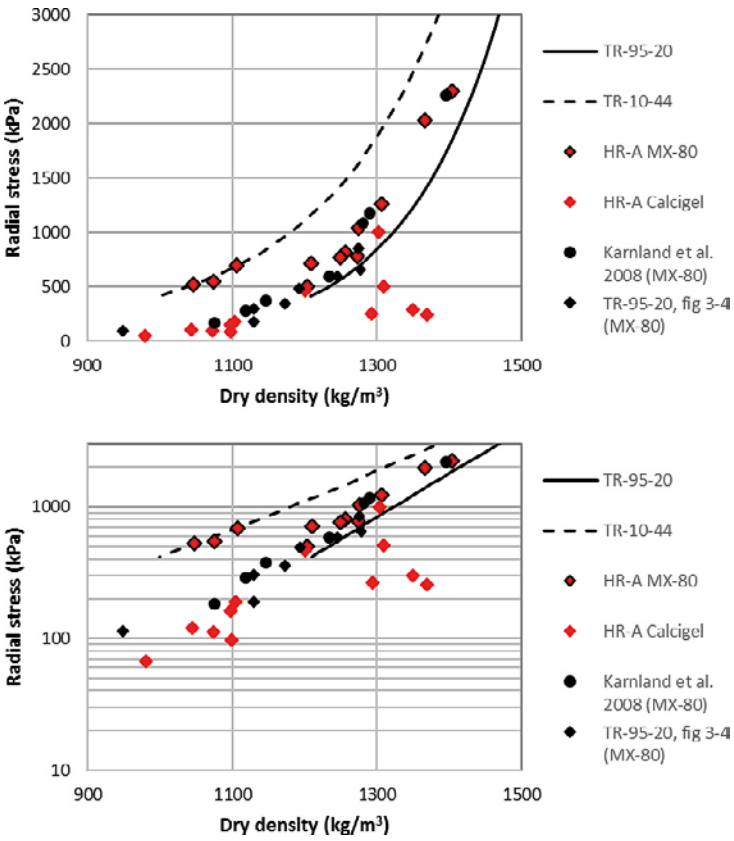

Figure 3-5. *Radially measured stresses from tests on MX-80 (red markers with marker lines) and Calcigel (red markers without marker lines) in the HR-A series, i.e. axial swelling in the HR-series. The results are plotted as a function of dry density and both with linear (upper) and logarithmic (lower) y-axis. Results from other studies on MX-80 are also plotted.*

3.3.2 Gradients in dry density after swelling

Time seems to slightly influence the density gradient after swelling but still after long time density gradients were observed. The remaining density gradients after swelling and homogenisation are plotted as a function of the swelling in Figure 3-6. In the diagram the density gradients have been normalized with the actual initial dry density and the specimen height or radius in the direction of swelling and plotted as a function of swelling *s* according to Equation 3-1. The markers (circles, diamonds) denote results from different test series (basic-series, HR-series) with specimens having different sizes (H/D = 20–40/50, H/D = 40–80/100). The different colours of the markers (red, yellow and blue) show the different type of swelling (axial swelling, radial outward swelling, and radial inward swelling). The tests were completed when no or only small changes with time were measured and different total time was therefore used for the tests (in the Basic series between 11–137 days and in the HR-series between 49–172 days). The total time may have influenced the size of the gradients but is not further commented here.

Figure 3-6 indicates that the dry density gradient in the swelling direction seems to have similar dependence on the magnitude of the swelling, irrespective of the type of swelling, although the scatter is larger for the radial swelling tests. No clear difference between the results from the smaller specimens (in the basic series marked with circles) and the larger specimens (in the HR-series marked with diamonds) can be observed. As an example the results show a normalized dry density gradient of 6 m^{-1} after 40 % swelling. With an initial dry density of 1 660 kg/m^3, the final density gradient will then be 10 (kg/m^3)/mm and the dry density difference over a 30 mm specimen will be 300 kg/m^3 (as in A01-10) or 400 kg/m^3 over a 40 mm specimen (as in HR-A4).

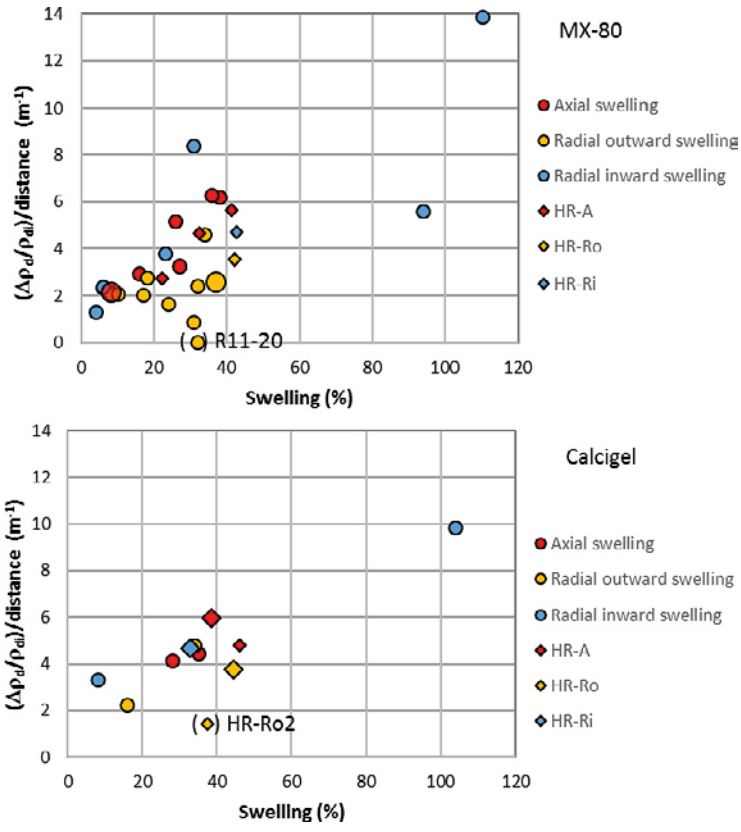

Figure 3-6. *Gradients of dry density normalized with the initial dry density over the specimen height or radius in the direction of swelling with results of MX-80 (upper) and of Calcigel (lower). The different series Basic and HR are marked with circles and diamonds, respectively, and the colours (red, yellow, blue) denote the type of swelling (axial, radial outward, radial inward). Larger marks are given where water pressure was used for some time. Somewhat uncertain test results from specimens R11-20 and HR-Ro2 are put in brackets.*

The results of two specimens deviate and those are put in brackets in Figure 3-6, one in the basic series which swelled 30 % radially (R11-20, Dueck et al. 2014) and one specimen in the HR-series which swelled 37 % (HR-Ro2, Dueck et al. 2016). Both specimens showed very low density gradients after dismantling. One possible explanation for the deviations could be insufficient and unevenly distributed water supply but since this cannot be fully explained these results should not be considered as representative.

Gradients in dry density were also studied in tests where the specimens initially consisted of two parts having quite different densities but where no swelling occurred. Five tests with these conditions were run; two specimens in the HR-series, HR-A2 (Dueck et al. 2016) and HR-A8 (Dueck et al. 2018), and three specimens in the Wetting series, W1-2, W1-3 and W1-4 (Dueck et al. 2018). The final normalized dry density gradients of these specimens, expressed as in Figure 3-6 i.e. $(\Delta\rho_d/\rho_{di})$/distance, is approximately 6 m^{-1} from the HR-series and between 3.3 m^{-1} and 4 m^{-1} in the W-series. Thus, in addition to swelling, the initial density distribution will influence the remaining density gradients.

The increase in density gradient with swelling, shown in Figure 3-6, is an illustration of the behaviour in the small scale since there is a limit to the possible density difference at a specific average stress and geometry. The results cannot be extrapolated to large scales and the effect of creep has not been considered.

3.3.3 Influence of water pressure

Water pressure was applied in the final part of several tests in order to investigate its influence; two in the basic series (A01-16, R11-24, Dueck et al. 2016), four in the HR-series (HR-A7, HR-A8, HR-Ro3, HR-Ri2, Dueck et al. 2018) and one in the W-series, (W1-4, Dueck et al. 2018). In general, the influence of water pressure was small and after removal of the water pressure the stresses mainly increased compared to the stresses before the water pressure was applied. This is in agreement with previous studies (Birgersson and Karnland 2015) where hysteresis effects were referred to.

Examples of the test results are shown in Figure 3-7 and Figure 3-8 with the evolution of the total stress (to the left) and the effective stresses (to the right) from the tests HR-A8 and HR-Ro3, respectively. The effective stress was calculated as the measured total stress minus the applied water pressure. While test HR-A8 started with two blocks having different densities the specimen used in test HR-Ro3 swelled 45 % radially. The material used in the two tests was Calcigel and the maximum water pressure was in both tests 100 kPa. As can be seen in Figure 3-7 and Figure 3-8 the measured total stresses increased or were approximately the same compared to the stresses measured before the water pressure was applied. Thus, the effective stresses were approximately the same or less when the water pressure was applied. From the test series there is also an example of a remaining decrease in effective stress after removal of the water pressure and the use of a small water pressure has therefore been recommended to measure the final stresses as correct as possible.

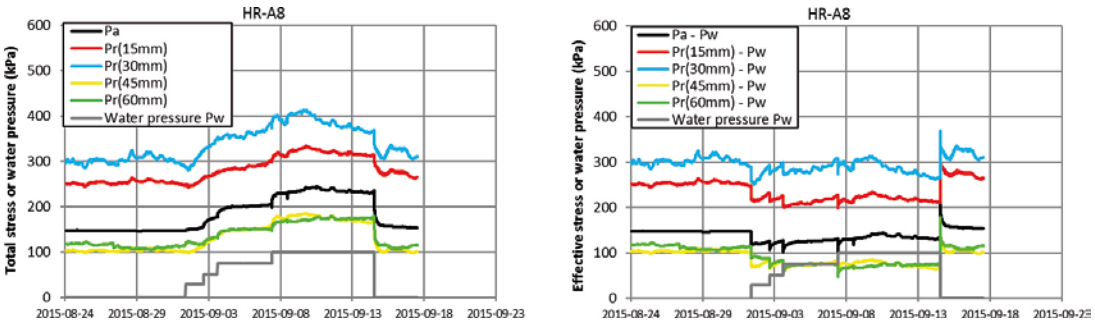

Figure 3-7. *Total stress and water pressure (left) and effective stress (right) as a function of time from test HR-A8 in the HR-series where the specimen consisted of two blocks having quite different densities but no swelling into an empty space. The effective stress was calculated as the measured stress minus water pressure and the water pressure varied between 0 and 100 kPa.*

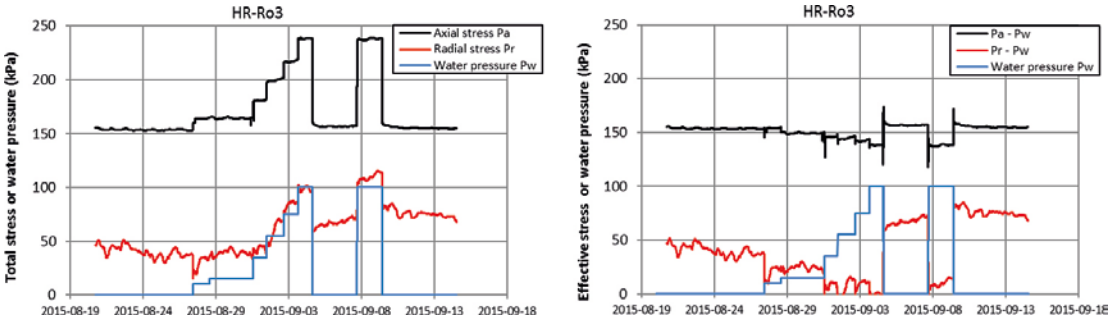

Figure 3-8. *Total stress and water pressure (left) and effective stress (right) as a function of time from test HR-Ro3 exposed to radial swelling in the HR-series. The effective stress was calculated as measured stress minus water pressure and the water pressure varied between 0 and 100 kPa.*

The main part of the specimens exposed to water pressure showed no large or obvious influence on the final density gradient after the use of water pressure. The test results where water pressure was introduced are marked with larger symbols in Figure 3-6 and the results from the actual specimens, two specimens of MX-80 and three specimens of Calcigel, do not deviate from the other results. However, an indication of better homogenisation after the use of water pressure is given when two similar tests with Calcigel in the W-series are compared (W1-2 and W1-4 from Dueck et al. 2018). The specimen exposed to water pressure showed a normalized dry density gradient ($(\Delta\rho_d/\rho_{di})/H$) of 3.3 m^{-1} while the corresponding value from the specimen not exposed to water pressure was 4 m^{-1}, cf. Section 3.3.2. This indication of an improved homogenisation is another example where the use of water pressure could be beneficial in this type of test.

3.3.4 Influence of friction

The friction angles in the friction tests were interpreted as a function of the swelling pressure according to Figure 3-9 (Figure 5-67 in Dueck et al. 2016 and Figure 4-27 in Dueck et al. 2018). The friction angle was evaluated from Equation 3-3 where F is the measured force, A_s is the radial surface area of the specimen, P_r is the radial stress perpendicular to the ring, and ϕ is the friction angle between the ring and the bentonite specimen.

$$F = A_s \cdot P_r \cdot \tan(\phi) \qquad (3\text{-}3)$$

The results show that, the friction angle evaluated at peak strength between the bentonite and the surfaces that had grooves corresponds well to the model of the bentonite internal friction angle ϕ_n presented by Åkesson et al. (2010b). The peak values when other surfaces were used yield lower friction angles. The largest difference between the peak and residual values are seen in the tests with grooves on the surface towards the bentonite and at low swelling pressure.

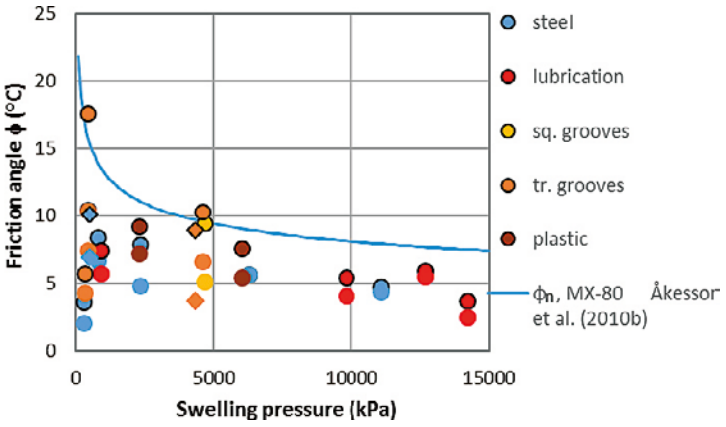

Figure 3-9. *Friction angle as a function of swelling pressure from tests on MX-80 (circles) and Calcigel (diamonds) in the series with friction tests. The swelling pressure was measured radially. Marker lines around the symbols represent peak values and no marker lines represent residual values.*

The results can also be plotted as the measured shear stress as a function of the dry density, which is shown in Figure 3-10. In this diagram the line represents half of the maximum deviatoric stress, evaluated from a model presented by Börgesson et al. (1995), which is a measure of the shear strength. The results show that the main part of the evaluated peak stresses follows the model and the residual values are lower. In one of the tests on MX-80 where triangular groves were used (light brown circles) the dry density determined after the test was uncertain and too low compared to the measured swelling pressure (see Table 5-8 in Dueck et al. 2016). This yields that in spite of that the results from this test fit well into Figure 3-9, where only stresses are considered, they deviate in Figure 3-10, where the uncertain density is used, and are therefore put in brackets.

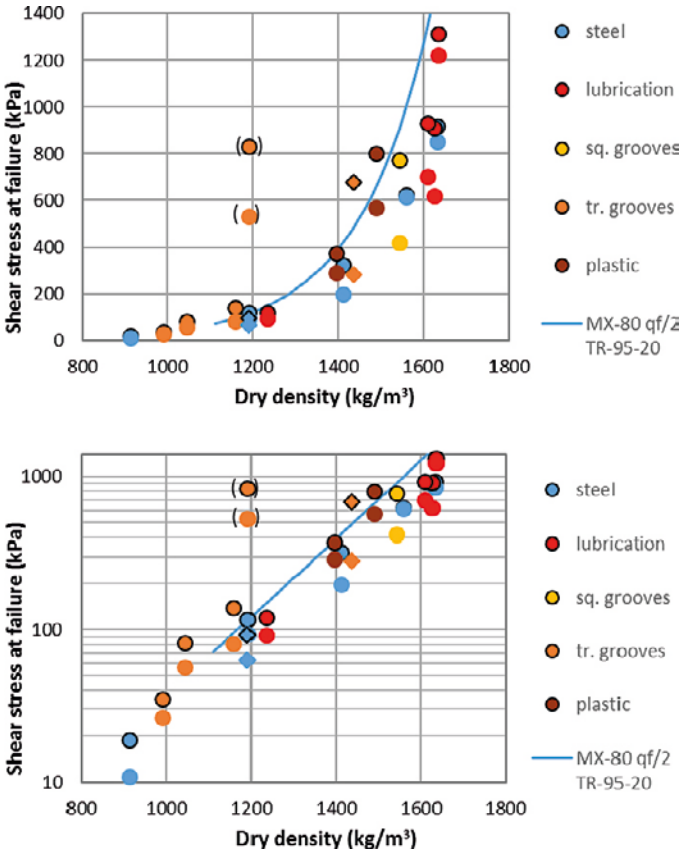

Figure 3-10. *Shear strength as a function of dry density from the friction tests in the Fr-series on specimens of MX-80 (circles) and of Calcigel (diamonds). The values in brackets represent a test where the density was uncertain (see Dueck et al. 2016). The diagram is plotted with a linear y-axis (upper) and a logarithmic y-axis (lower).*

3.3.5 Accuracies, uncertainties and limitations

Measurements and results often suffer from a scatter that could be caused by e.g. inaccurate devices and uncertain properties of the specimens. Such uncertainties put a limit to the usefulness of the results; for predictions and extrapolations. Below some examples from the actual laboratory test series are given.

The accuracy of the sensors used as load cells, pressure and deformation transducers are relatively high, the error is generally less than 5 %, and since they are calibrated and controlled regularly this will not limit the usefulness of the results. However, the radially measured stresses were done by use of small pistons and the measured stresses are thus representative for relatively small volumes. In addition, the small pistons measure towards a very stiff material that requires a small deformation, which means that small irregularities may affect the results, but the swelling ability of the bentonite puts a limit to these errors. The axially measured stresses, on the other hand, were measured by use of a piston with larger cross section area, of the same size as the specimens. However, in tests involving radial swelling the measured axial stress did not represent a specific position but an average of the stresses at different radii. The use of pistons for the measurements of stresses might have introduced friction forces which in the actual tests were minimized by use of lubrication.

The accuracy of the measured base variables after dismantling is very high but the results from some tests showed large scatter in the calculated degree of saturation which usually is a measure of the uncertainty in the determination. However, in this study the relatively large scatter in the degree of saturation was mainly observed in tests involving large density gradients over small distances. Since degree of saturation requires two different samples that may differ in density and water content the scatter could be regarded as a measure of the difficulties to take representative specimens for determination of both water content and density from a small volume, see e.g. HR-Ri1 (Dueck et al. 2016). Another variable where some uncertainty was noted was the initial density before swelling, especially when it was determined on trimmed specimens having somewhat uneven circumference. This influenced also the accuracy of the calculated swelling in these tests.

Limitations to generalize the test results from this study are mainly coupled to the equilibrium at termination of the tests and the uniqueness of the tests. One important result from the test series is the remaining density gradients. Time seems to influence this but still after a long time, and with the requirement of small or no stress change at termination, density gradients were observed. However, constant stress with time will not guarantee that the specimen is in equilibrium which means that extrapolation of the density gradients with time is uncertain.

4 Application of test results for modelling with the FE-program Abaqus and with simplified analytical solutions

4.1 Introduction

Some of the homogenisation tests included in the project have been modelled with the finite element code Abaqus in order to fulfil the purposes of the project to evaluate models, model parameters and modelling tools. Some tests have been used as modelling tasks in the TF EBS (Task Force for modelling engineered barrier systems) and some other tests have been modelled as a part of this project. The modelling tasks presented in Section 4.2 (Fundamental swelling tests) and Section 4.3 (Self Healing Test SH1) are summaries of this work for TF EBS and are in detail described in Börgesson et al. (2019).

4.2 Fundamental swelling tests from the HR-series. Evaluation of models and model parameters and verification of the models

4.2.1 General

This section is a summary of the calibration and verification exercises done for the Homogenisation task (Task 1) in the TF-EBS. The tasks, the material models, the test results and the modelling are reported in Börgesson et al. (2019). The tests and some results are also described earlier in Section 3.2.1 and in Dueck et al. (2014).

The original tests included in the task descriptions, intended to be used for the calibration, were made in cells with the diameter 5 cm. Measurements and sampling with high enough accuracy were difficult due to the small test size. Therefore tests in a larger scale in cells with the diameter 10 cm were also made. These larger tests were used for modelling instead of the tests in smaller scale.

Four different test types have been modelled, namely axial swelling, radial outwards swelling, radial inwards swelling and isotropic swelling. The axial swelling test was used for checking and calibrating the material models and the other tests were used to evaluate the derived model.

The models used are elastic-plastic models. The elastic part of the model is a so called porous elastic model that has a logarithmic relation between void ratio and average stress. Two different models have been used for the plastic part of the model, a Drucker-Prager plasticity model and Claytech plastic cap model.

4.2.2 Axial swelling

The axial swelling test was at first used to check and calibrate the models. The Drucker-Prager model could not yield an acceptable result regarding the swelling pressure evolution and the final gradient in density that occurred after equilibrated swelling as described by Börgesson et al. (2019). Instead the Claytech model described already by Börgesson et al. (1995) was used with parameter values derived at that time. However, in order to get the best agreement between measured and modelled results the parameters of the elastic model, the plastic model and the hydraulic conductivity had to be somewhat changed.

In this test the axial swelling pressure was measured on the upper piston and the radial pressure was measured in three points. After termination of the test the specimen was sliced and the density distribution in axial direction determined. Figure 4-1 shows the test set-up and Figure 4-2 and Figure 4-3 show comparison between modelling results and measured results. The results agree rather well although both the density and logically also the stresses are a little higher in the test.

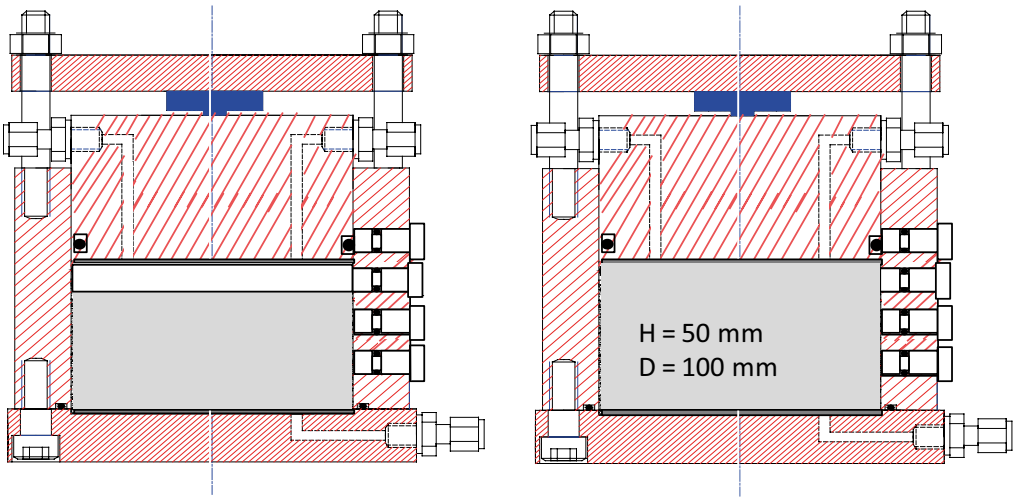

Figure 4-1. *Set-up used for the axial swelling tests (HR-A). Water is only supplied from a filter placed above the specimen. Radial swelling pressure was measured 15 mm, 30 mm and 45 mm from the bottom of the oedometer.*

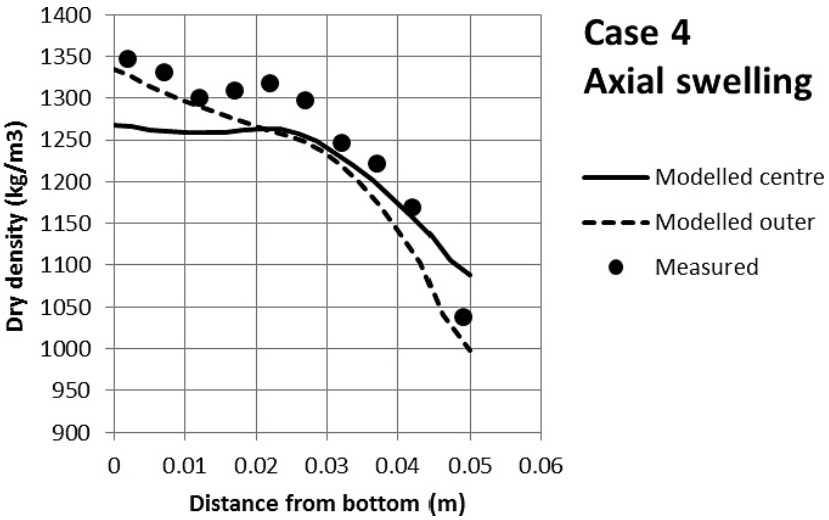

Figure 4-2. *Calibrated Claytech plastic cap model. Modelled density distribution along the centre axis and along the periphery (outer) and measured average density distribution.*

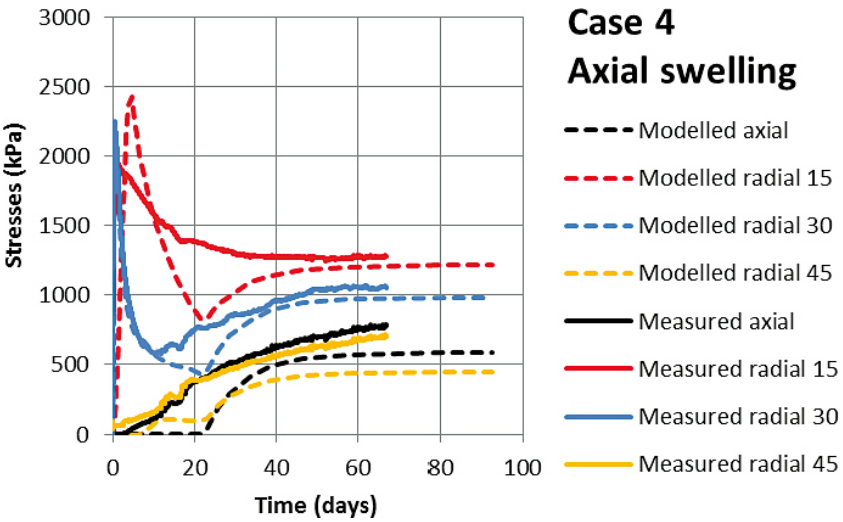

Figure 4-3. *Calibrated Claytech plastic cap model. Modelled and measured evolution of normal stress.*

4.2.3 Radial outwards swelling

Then the calibrated model was checked by modelling the radial outwards swelling test and good agreement was achieved, which confirmed the model. Figure 4-4 shows the test set-up and Figure 4-5 and Figure 4-6 show comparison between modelled and measured results.

The comparison shows that although the calibration was done for the axial swelling test the agreement for the radial swelling is very good, even better than for the axial test.

The models were 2D axial symmetric element meshes and included contact surfaces between the bentonite material and the restraining outer cell surfaces. These contacts were applied with simulated friction with a friction angle of 7°, which was taken as an average of the friction angle of the bentonite at the actual density divided by two (see Section 3.3.4).

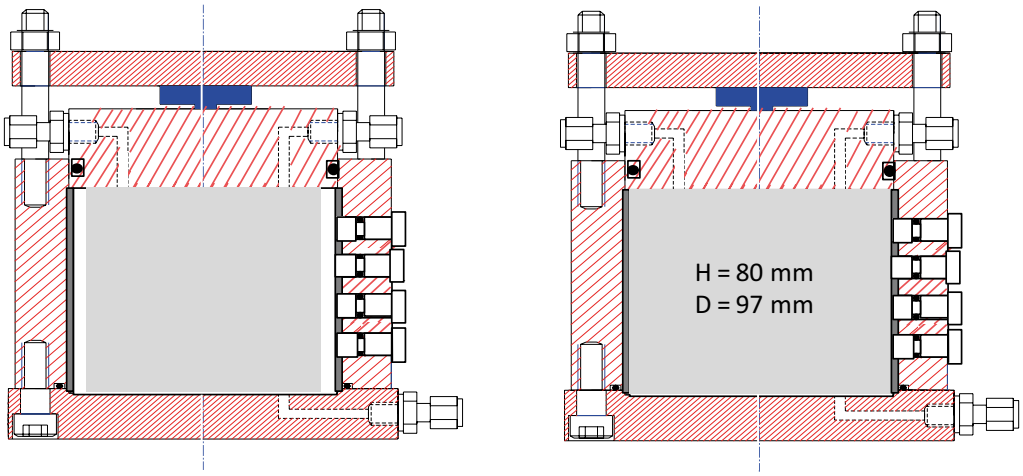

Figure 4-4. *Set-up used for the radial outward swelling tests (HR-Ro). Water is supplied from a radial filter between the surrounding steel ring and the specimen. Axial swelling pressure was measured on the top lid and radial swelling pressure was measured 15 mm, 30 mm, 45 mm and 60 mm from the bottom of the oedometer.*

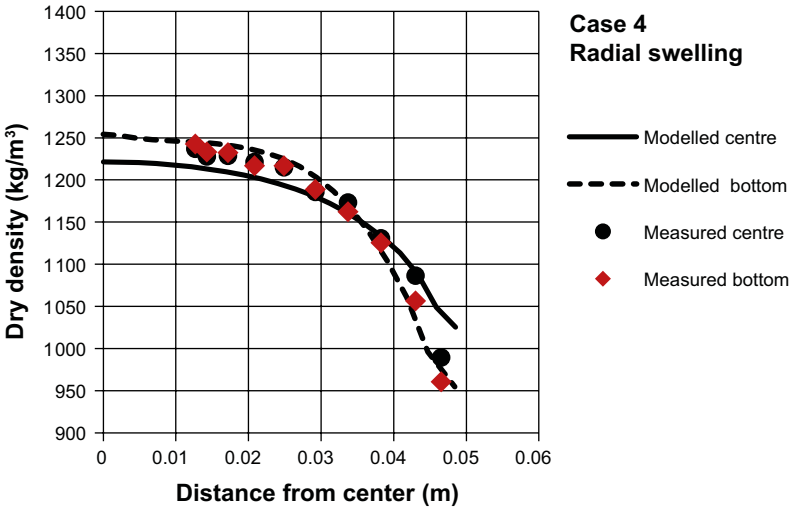

Figure 4-5. *Modelled and measured dry density distribution.*

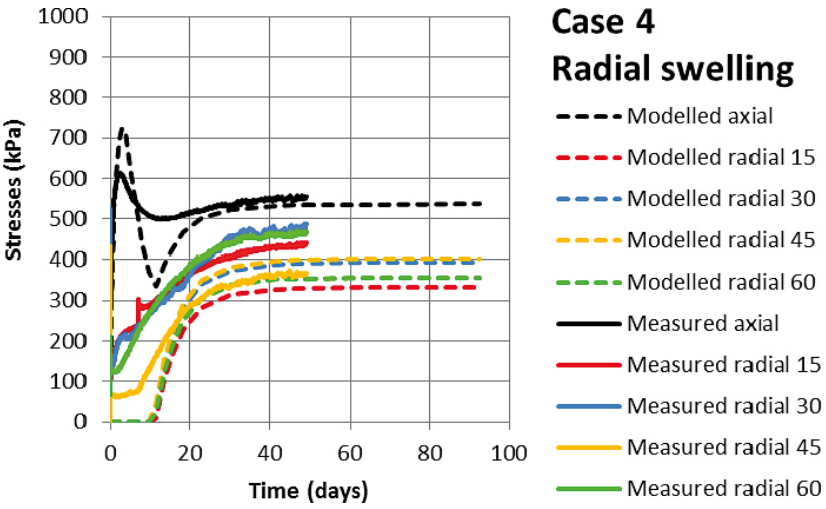

Figure 4-6. *Modelled and measured evolution of normal stress.*

4.2.4 Influence of friction

In order to investigate the influence of friction against the steel surfaces identical calculations were made with the friction angle 0°. The results showed that the external stresses and the density distribution were very little affected by friction. Only if detailed information about the stress distribution is requested (e.g. the reduction in swelling pressure in the axial direction after axial swelling) the friction must be included. Another conclusion was that the lack of external friction was compensated by the internal friction with high Mises stresses and that smooth surfaces does not reduce the density gradients significantly.

Figure 4-7 shows comparison of modelling results with and without friction for the axial swelling test.

4.2.5 Other swelling types

Two other test types have been performed and modelled. The models and the results are described in detail in Börgesson et al. (2019). Here we will only give a short summary. The radial inwards swelling test was modelled without friction against the walls. The model did not manage to get complete filling of the central hole. The reason is not clear but it is judged to be caused by numerical imperfections and has been observed in other similar calculations. Otherwise the test and the simulation agreed fairly well.

Finally, a new test with the intention to have isotropical swelling was performed and modelled, although the model was simplified as a swelling sphere instead of a filled cylinder. This simulation led to a number of observations and conclusions (Börgesson et al. 2019):

- The test does not yield isotropic swelling more than perhaps in the inner part of the specimen, the main reason being that wetting takes place from the outer boundary which generates anisotropic deformations.
- Isotropic swelling can only take place if water is modelled as being available in all nodes or if the wetting in the test is done so slowly that the water content increase takes place simultaneously in the entire specimen.
- A test that could simulate isotropic swelling might be to increase the relative humidity RH so slowly that very small gradients will occur in the specimen.
- Isotropic swelling yields too little swelling by the material model since plastic dilatancy is required and not included without deviatoric stresses.
- An improvement of the model could be to include plastic strain with dilatancy in the entire elastic zone of the p-q plane.

The overall conclusion of the calibration and evaluation models is that the model simulates bentonite swelling well within a limited density interval but also that the model does not work well for the unlikely case of completely isotropic swelling.

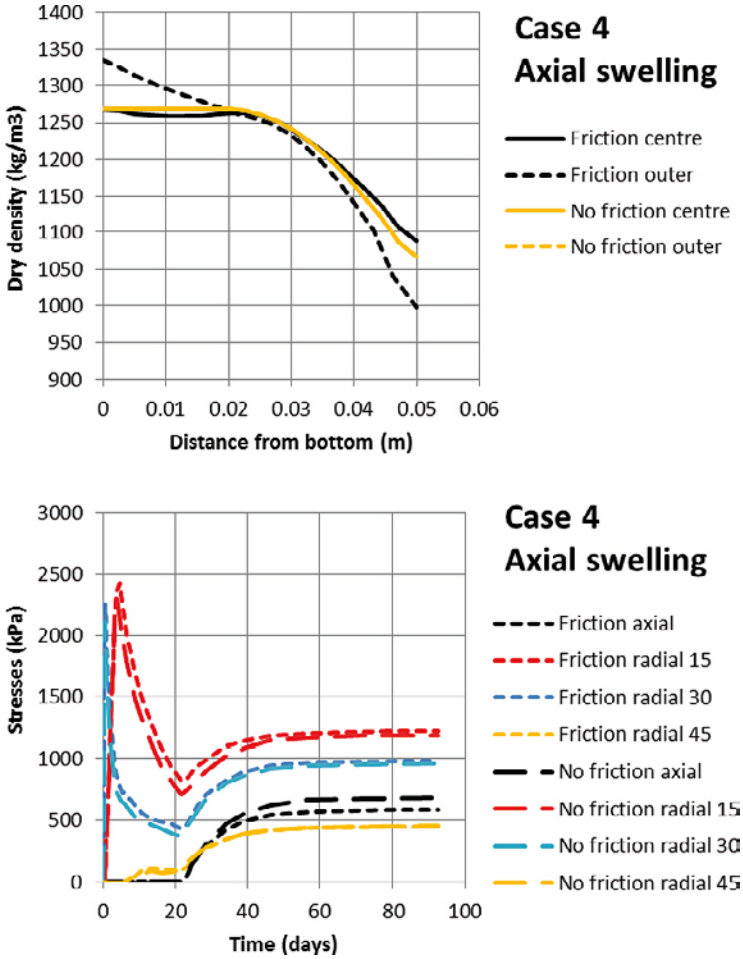

Figure 4-7. *Comparison of modelling results of the axial swelling test with and without friction between the bentonite and the cylinder. Friction outer and friction inner means the outer element column in contact with the ring and the central element column at the symmetry line.*

4.3 Modelling of the Self-Healing Test SH1

The Self-Healing test SH1 has been modelled as Subtask 2 of the homogenisation task of phase 2 of the TF EBS. The test and some results are described in Dueck et al. (2018) and in Börgesson et al. (2019). This section includes only a summary of the test, the model and the results. More detailed descriptions are found in the references.

The test was modelled with two different material models. The test concerned swelling and self-healing of two cavities with the dimensions 35 × 50 × 70 mm cut in a bentonite block with the diameter 300 mm and the height 100 mm. The test included measurement of swelling pressure in 9 positions and suction in 2 positions. The test was terminated after equilibrium and multiple samples taken. The density and water ratio of the samples were determined. The test ran for 2 years and 8 months.

A blind prediction was done and delivered before start of the test. The new Claytech Plastic Cap (P-C) material model that had been calibrated and verified in Subtask 1 of the homogenisation task was used for the prediction. The test was also modelled using the old Drucker-Prager (D-P) plastic material model that had been used for SR-Site.

Before termination of the test a number of additional calculations were made in order to improve the results, but without changing the material model or the parameters.

Large problems with convergence of the calculations were encountered in all calculations. The consequences of these problems were that the calculations stopped too early, but for the calculations referred to here the problems were overcome.

Finally, the results from the prediction and the other calculations were compared to the measured results. The modelling and the evaluation of the results are described in Börgesson et al. (2019).

The element mesh was simplified to cover only 1/8th of the bentonite block by using symmetry planes. Figure 4-8 shows the block before installation in the steel confinement and the element mesh.

The comparisons yielded the following observations and conclusions:

The calculated time to reach equilibrium of the homogenisation phase was generally 2–3 times shorter than the measured time for all calculations. The main reason is judged to be caused by the difference in modelled and actual initial conditions. The actual initial degree of saturation was S_r = 95 % – 97 % compared to the modelled S_r = 100 %, which means that some additional water must be taken up by the bentonite. In the model virtually all water needed was already in the bentonite from start. The reason for starting with full saturation is that the material model used and confirmed by the fundamental swelling tests only handles water saturated bentonite. In addition, the actual size of the bentonite block was slightly smaller than the inner boundaries of the steel cylinders, which means that some swelling was required.

All models yielded a remaining gap of a few mm in parts of the final contact between the different walls of the cavity. One reason is the element size in the model. Smaller elements would probably reduce the gap but would also mean increased number of elements and cause even larger convergence problems. The Drucker-Prager model yielded slightly smaller remaining gap than the blind prediction.

The spreading of the stresses in the measuring points was larger in the models than measured. Both the blind prediction and the Drucker-Prager model yielded the highest stress 9.5 MPa in the measuring point located furthest away from the cavity and the lowest stress 2.0 MPa in the centre of the cavity while the measurements in corresponding places were 6.0 MPa and 3.3 MPa respectively.

The blind prediction yielded higher void ratio e = 1.2 in the centre of the cavity than the measured void ratio e = 1.0. The Drucker-Prager model yielded e = 1.05, which is in better agreement with measured results. This was also generally the case for the void ratio distribution.

Figure 4-9 shows the modelled void ratio distribution at the end of the test for the two material models used. The figure shows that the void ratio differs substantially between the two models. It is clearly lower for the D-P model. The figure also shows that the D-P model yields better closing of the cavity with smaller remaining gaps.

Comparison between modelled and measured density distribution is not so easy to make, since the measured samples had volumes of about 17 × 17 × 15 mm^3 and the modelling results have a resolution that is about 1 000 times larger. In order to be able to compare the results the sample geometries need to be put into the modelling figure and then an estimate of the modelled average density in the sample volume must be made.

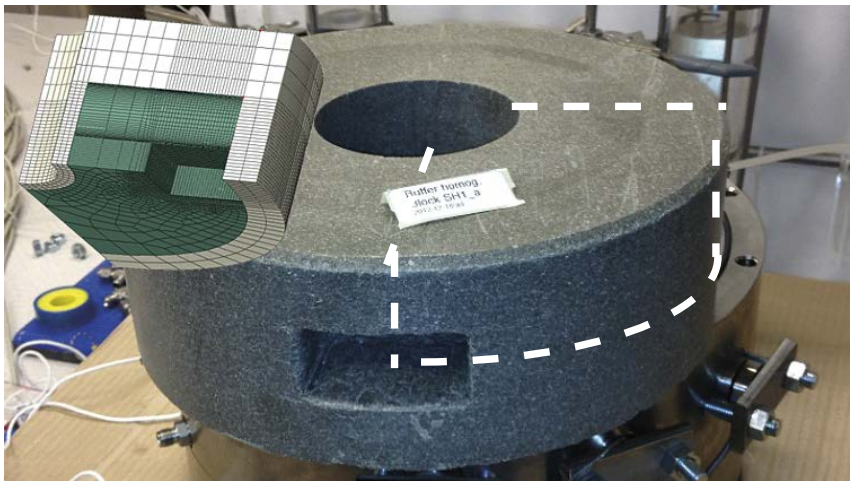

Figure 4-8. *Illustration of how the 1/8th part of the bentonite block is used in the element mesh. The mesh is shown upper left. The green part of the mesh corresponds to the bentonite.*

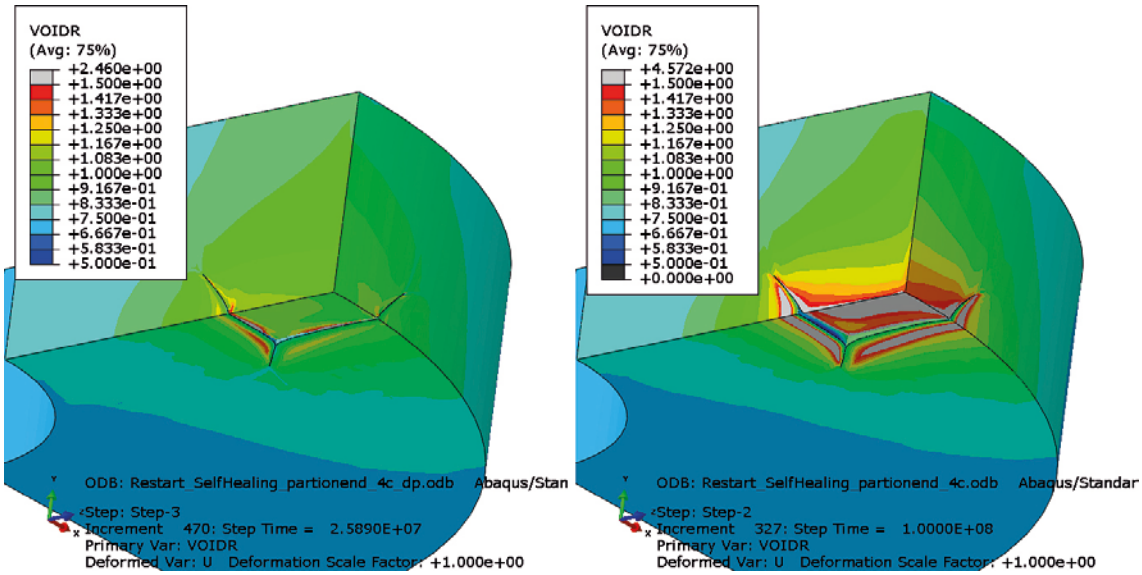

Figure 4-9. *Void ratio distribution at the end of the test. The results of the Drucker-Prager model (left) are compared to the results of the Plastic Cap model (right).*

An evaluation of the average void ratio in three sampling locations for the Drucker-Prager model is shown in Figure 4-10.

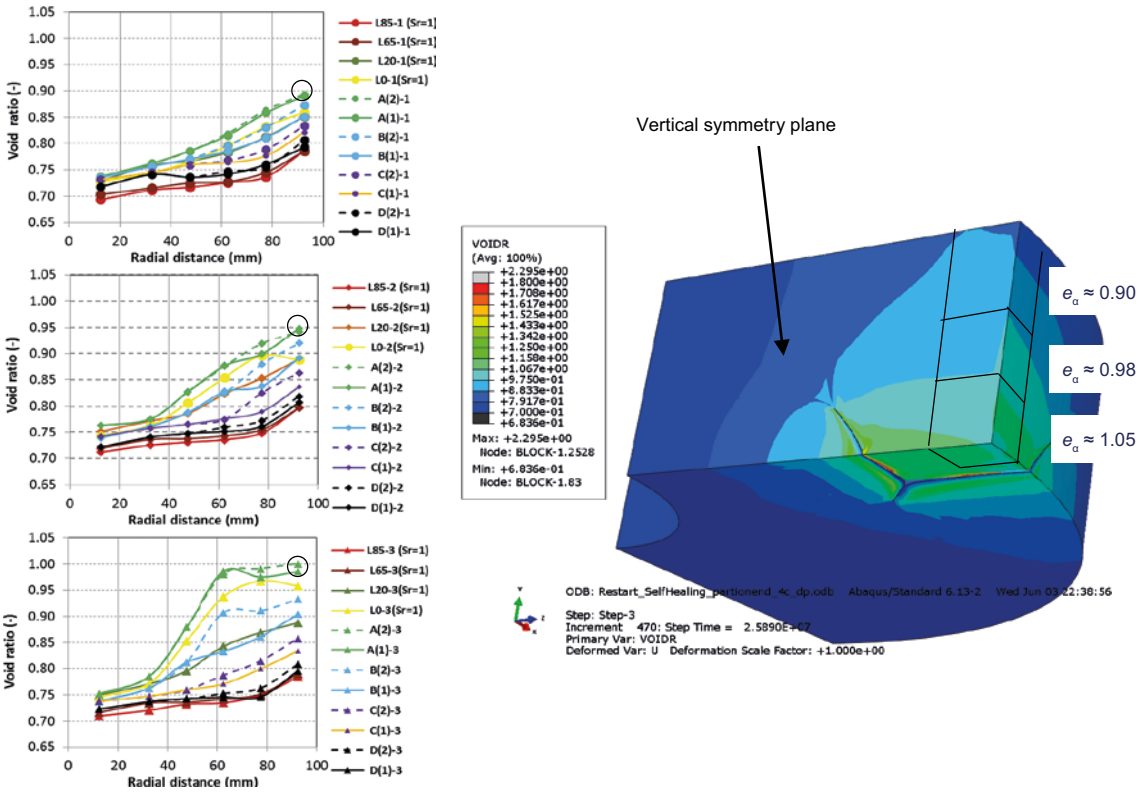

Figure 4-10. *Three sampling locations are put into the modelling results (with the D-P model) of the final void ratio distribution in the figure to the right and estimated average values of the void ratio for these volumes are shown. The left diagrams show the sampling results plotted as function of the radial distance to the inner steel tube. The green curves are the results for the sampling closest to the vertical symmetry plane. The measured void ratio in the three sample positions are encircled in the diagrams to the left.*

Figure 4-10 shows that the modelled void ratios in the three sample positions agree quite well with the measured values although slightly lower void ratios (higher densities) were measured than modelled. The modelled void ratios were 0.90, 0.98 and 1.05 for the three sampling positions while the measured were 0.89, 0.95 and 0.98.

The modelled average stress for the two material models is compared in Figure 4-11.

Although the void ratio for the two models differ (0.95 compared to 1.2 in the sample taken in the centre of the cavity) the average stress does not differ much. It is actually slightly higher for the P-C model than for the D-P model, which is unexpected considering that the void ratio is higher (lower density) for the P-C model. Both are in average slightly lower than 2.0 MPa in the volume corresponding to the sample taken in the centre of the cavity.

There is thus a disagreement in void ratio between the two models but an agreement in stress. The difference between the two models is judged to be caused by the difference in dilatancy during plastic straining. Both models underestimate the stress and the density in the cavity.

The trials to improve the results by elaborating with the element mesh (but not the material model) were not successful. No better results were achieved.

A general conclusion is thus that the Plastic Cap model underestimated the self-healing ability (or the homogenisation) of the bentonite in the test by yielding too high void ratio and too low stresses in the former cavity. The Drucker-Prager plastic model captured the homogenisation better with a void ratio distribution that agreed rather well (although still a little too high) with the measured and smaller remaining gaps in the former cavity. However, also this model yielded the same too low stresses in the cavity.

So, the test SH1 with a large scale and complicated geometry yielded better results when the Drucker-Prager model was used while the fundamental swelling tests with small scale simple swelling models yielded much better results when the Plastic Cap model was used. The reason for the better homogenisation and better results of the Drucker-Prager model for SH1 is judged to be that the material model is simpler and convergence much easier to obtain.

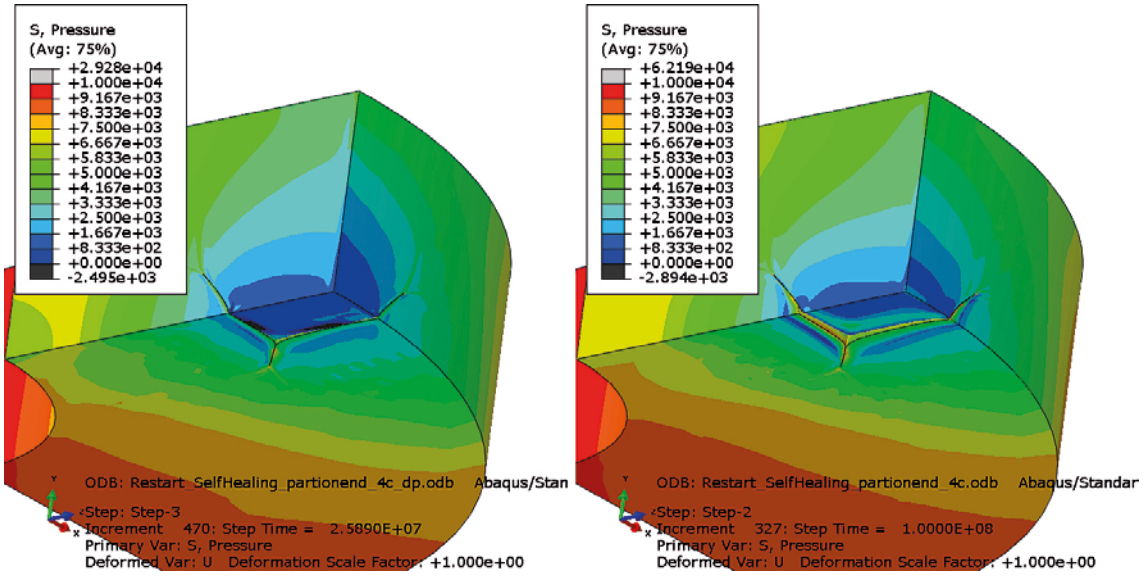

Figure 4-11. *Distribution of modelled average stress (kPa) at the end of the test. The results of the Drucker-Prager model (left) are compared to the results of the Plastic Cap model (right).*

4.4 Homogenisation in long tubes

4.4.1 General

Tests of homogenisation in long tubes are ongoing with the purpose to investigate

- The ability of bentonite to homogenise in long tunnels or boreholes.
- The influence of friction between bentonite and different surface structures.
- The long term behaviour of large density differences.

Ten tests with low density bentonite pellets in contact with high density compacted bentonite blocks installed in long steel tubes have been started. In most tests, tubes with the diameter 26 mm and the length 250 mm were used. The tests and results up to mid-2016 are reported in Dueck et al. (2018).

One of the tests (FLR5) has been terminated and sampled for determination of the density distribution two years after its start. The other tests will be terminated after different times in order to see the influence of time on the homogenisation. The results from the terminated test and the results of measured evolution of swelling pressure in one of the tubes will be analysed in this section.

4.4.2 Geometry and materials

The test set-up of FLR5 is shown in Figure 4-12. Half the tube is filled with highly compacted bentonite blocks with the diameter 25 mm and the other half with pellets. Swelling pressure is measured at four locations, two in the pellet section and two in the high density section, measuring axial and radial stress. Water is supplied through a filter at the top of the pellet section.

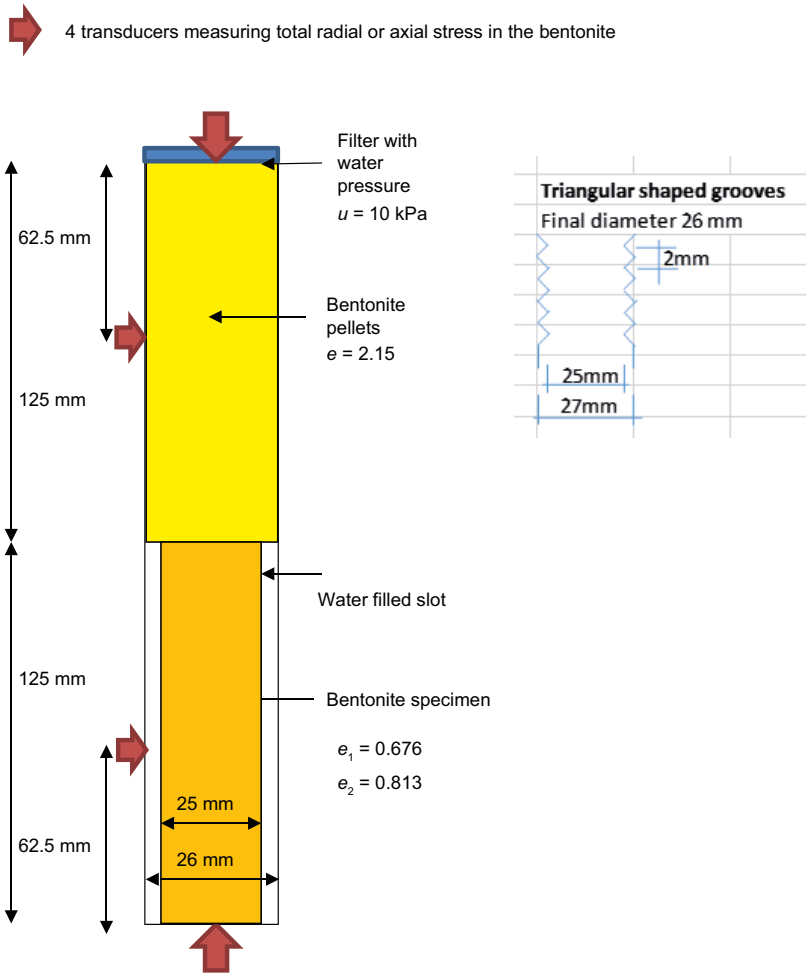

Figure 4-12. *Geometry of the set-up and void ratios of the installed bentonite in test FLR5. e_1 is the void ratio of the blocks and e_2 is the final void ratio after radial swelling. The grooves in the inner surface of the tube is also illustrated.*

The inner surface of the tube was grooved with 1 mm deep triangular groves yielding a diameter varying between 25 and 27 mm as shown in Figure 4-12. The average inner diameter of the tube is thus 26 mm.

The initial dry densities and corresponding void ratios are shown in Table 4-1.

Table 4-1. Initial conditions for the bentonite in the tubes.

Section	Dry density (kg/m^3)	Void ratio	Swelling pressure (kPa)	Remarks
Pellet section	882	2.15	120[1)]	See text in Section 4.4.3
Pellet section Values used in the model[3)]	1 051[3)]	1.65	120[2)]	See text in Section 4.4.3
High density section	1 659	0.676	12 968[2)]	Installed
High density section	1 534	0.813	4 910[2)]	After radial swelling

1) (Börgesson et al. 1995).

2) Equation 4-3.

3) Apparent density to fit Equation 4-3.

The reason for changing the initial density in the pellet filling in the model is that it is outside the validity of the model as explained in Section 4.4.3.

4.4.3 Analytical solution

The equilibrium state regarding the relation between swelling pressure and the friction between the bentonite and the walls after completed swelling and compression can be derived and described according to Equations 4-1 and 4-2 (see e.g. Åkesson et al. 2010a).

$$\sigma = \sigma_0 \cdot e^{\frac{-2z\tan\phi}{r}} \tag{4-1}$$

$$z = \frac{r}{2\tan\phi}\ln\frac{\sigma_0}{\sigma} \tag{4-2}$$

where

r = tube radius

z = axial distance from the bottom

σ_0 = swelling pressure at $z = 0$

σ = swelling pressure at z

ϕ = friction angle between the bentonite and the tube surface

The set-up is designed with the idea that the swelling of the high density bentonite and the compression of the low density bentonite will take place in the central parts of the tube and the difference in swelling pressure will be taken by the friction between the bentonite and the walls of the tube. The length of the tube is designed so that initial densities of the bentonite in the uppermost part of the pellet section and in the lowermost part of the high density section shall remain intact and the density decrease will take place along the length L also called the transition zone, without affecting the end densities. Figure 4-13 illustrates the assumed equilibrium state, which was also confirmed is the tests.

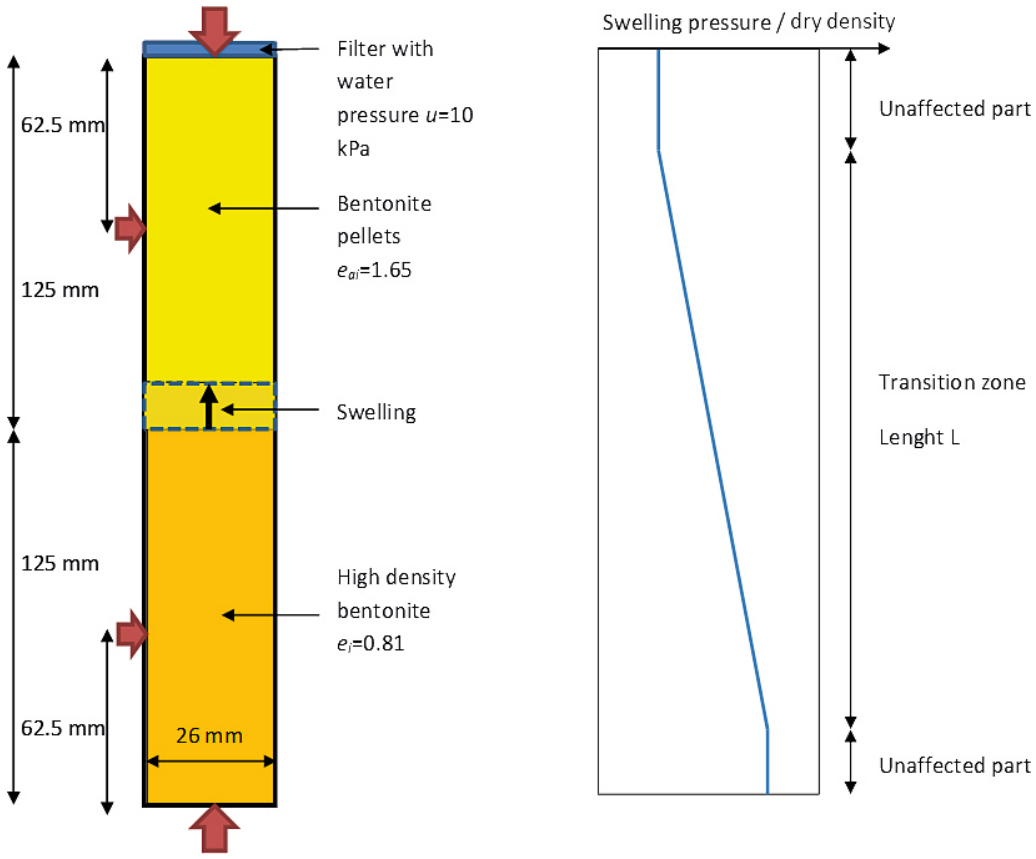

Figure 4-13. *Illustration of the transition zone and the swelling pressure and dry density distributions after completed swelling.*

In order to analyse the density distribution after equilibrium we need a relation between density and swelling pressure. The relation in Equation 4-3 was derived in Börgesson et al. (1995).

$$\sigma = \sigma_r \left(\frac{e}{e_r} \right)^{\frac{1}{\beta}} \tag{4-3}$$

where

e = void ratio

e_r = reference void ratio (= 1.1)

σ = swelling pressure (at e)

σ_r = reference swelling pressure (at e_r) (= 1 000 kPa)

β = −0.19

The validity of Equation 4-3 is limited to $0.5 < e < 1.5$. For void ratios above 1.5 the swelling pressure is higher as shown in Figure 3-15 in Börgesson et al. (1995).

The relation between void ratio and dry density is described by Equation 4-4.

$$\rho_d = \frac{\rho_s}{1+e} \tag{4-4}$$

where

ρ_d = dry density

e = void ratio

ρ_s = density of solids = 2 780 kg/m^3

Combination of Equations 4-3 and 4-4 yields the following initial swelling pressures for the high and low density sections by using the initial dry densities:

- High density section (before radial swelling) σ = 13.0 MPa.
- High density section (after radial swelling) σ = 4.9 MPa.
- Pellet section (Börgesson et al. 1995) $\sigma \approx$ 120 kPa.

In order to be able to use Equations 4-1 and 4-3 for the pellet filling we must apply an apparent density and void ratio that yields the swelling pressure 120 kPa. Table 4-1 shows those values.

The axial swelling can be modelled according to Equations 4-1 to 4-3. Combining the expressions in Equations 4-1 and 4-3 for the swelling pressure yields Equation 4-5.

$$\sigma_r \left(\frac{e}{e_r} \right)^{\frac{1}{\beta}} = \sigma_0 \cdot e^{-\frac{2z\tan\phi}{r}} \tag{4-5}$$

Applying Equation 4-4 for the relation between void ratio and dry density and

e_r = 1.1 = reference void ratio

σ_r = 1 000 kPa = reference swelling pressure at e_r = 1.1

yield Equation 4-6:

$$1000 \cdot \left(\frac{\left(\frac{\rho_s}{\rho_d} \right) - 1}{1.1} \right)^{\frac{1}{\beta}} = \sigma_0 \cdot e^{-\frac{2z\tan\phi}{r}} \tag{4-6}$$

$$\frac{\frac{\rho_s}{\rho_d} - 1}{1.1} = \left(\frac{\sigma_0}{1000} \cdot e^{-\frac{2z\tan\phi}{r}} \right)^{\beta} \tag{4-7}$$

$$\frac{\rho_s}{\rho_d} = 1.1 \cdot \left(\frac{\sigma_0}{1000} \right)^{\beta} \cdot e^{-\frac{2z\tan\phi}{r}\beta} + 1 \tag{4-8}$$

Applying β = −0.19, r = 0.013 m and ρ_s = 2.78 t/m^3 yields

$$\frac{2780}{\rho_d} = 1.1 \cdot \left(\frac{\sigma_0}{1000} \right)^{-0.19} \cdot e^{\frac{0.38 \cdot z \cdot \tan\phi}{0.013}} + 1 \tag{4-9}$$

$$\rho_d = \frac{2780}{1.1 \cdot \left(\frac{\sigma_0}{1000} \right)^{-0.19} \cdot e^{29.2 \cdot z \cdot \tan\phi} + 1} \tag{4-10}$$

Applying the initial swelling pressure at the high density zone σ_0 = 4 910 kPa yields

$$\rho_d = \frac{2780}{0.810 \cdot e^{29.2 \cdot z \cdot \tan\phi} + 1} \tag{4-11}$$

The length L of the transition zone can thus be derived by inserting the dry density of the pellet filling ρ_d = 1 051 kg/m^3.

$$0.810 \cdot e^{29.2 \cdot z \cdot \tan\phi} = \frac{2780}{\rho_d} - 1 \quad (4\text{-}12)$$

$$e^{29.2 \cdot z \cdot \tan\phi} = \left(\frac{2780}{1051} - 1 \right) / 0.810 \quad (4\text{-}13)$$

$$e^{29.2 \cdot z \cdot \tan\phi} = 2.031 \quad (4\text{-}14)$$

$$29.2 \cdot z \cdot \tan\phi = \ln 2.031 \quad (4\text{-}15)$$

$$z = L = 0.0243/\tan\phi \quad (4\text{-}16)$$

Equation 4-11 thus yields the dry density distribution along the tube axis after force equilibrium and Equation 4-16 yields the length of the transition zone. It should be noted that the dry density at void ratios higher than 1.5 (or dry densities lower than 1 112 kg/m^3) are incorrect and must be adjusted.

The void ratio distribution can be calculated with Equation 4-4 yielding

$$e = 0.810 \cdot e^{29.2 \cdot z \cdot \tan\phi} \quad (4\text{-}17)$$

and the swelling pressure distribution can be calculated with Equation 4-18 (same as Equation 4-3).

$$\sigma = \sigma_r \left(\frac{e}{e_r} \right)^{\frac{1}{\beta}} \quad (4\text{-}18)$$

The influence of the friction angle on the length of the transition zone according to Equation 4-16 is shown in Figure 4-14.The dry density distribution, the void ratio distribution and the swelling pressure distribution as function of the distance from the intact high density part (z) are shown for different friction angles in Figure 4-15, Figure 4-16 and Figure 4-17.

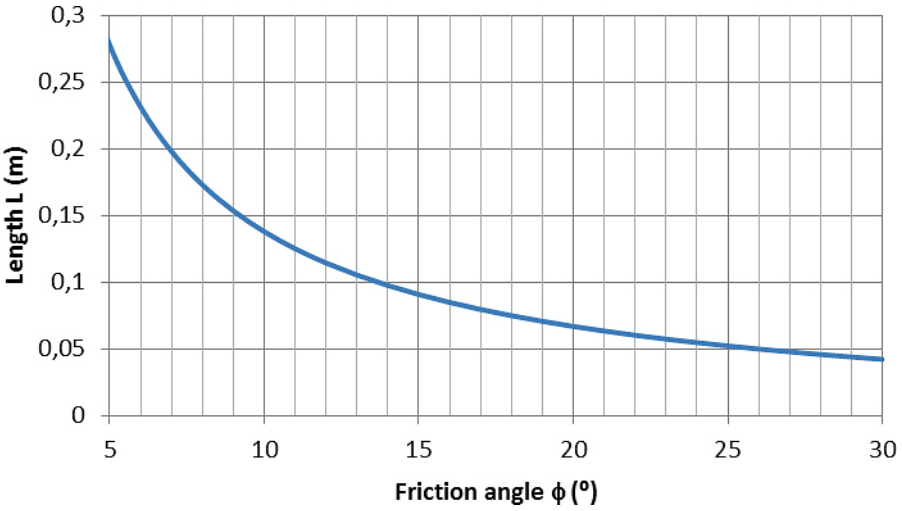

Figure 4-14. *The length of the transition zone L as a function of the friction angle according to Equation 4-16.*

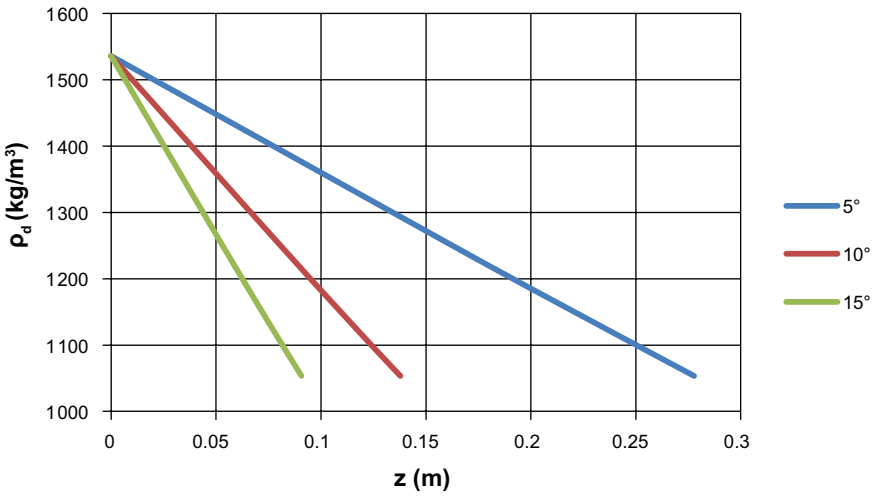

Figure 4-15. *Dry density distribution of the transition zone at different friction angles according to Equation 4-11.*

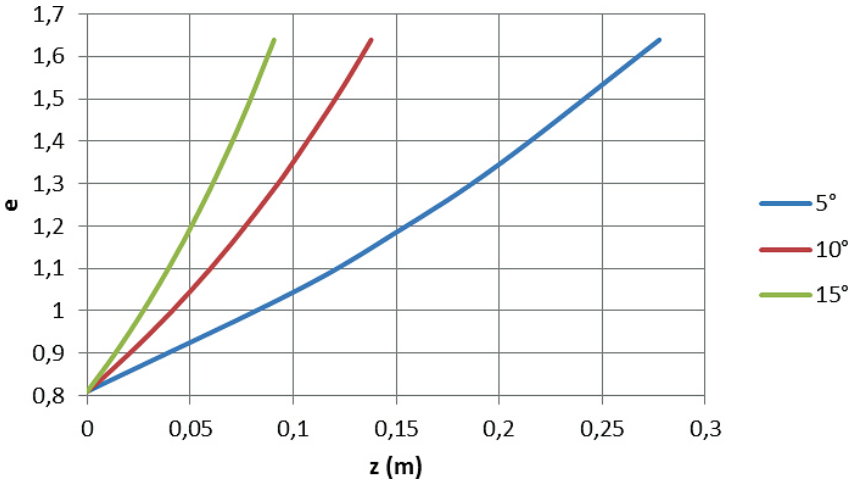

Figure 4-16. *Void ratio distribution of the transition zone at different friction angles according to Equation 4-17.*

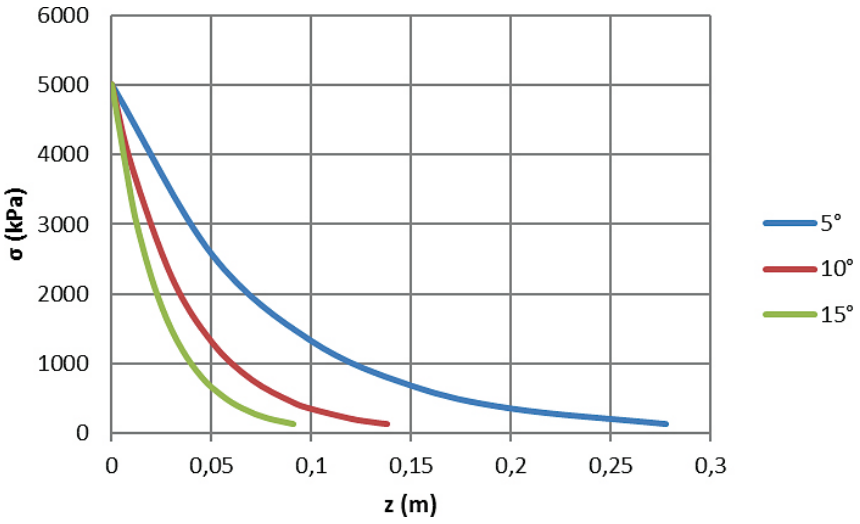

Figure 4-17. *Swelling pressure distribution of the transition zone at different friction angles according to Equations 4-3 and 4-17.*

The test FLR5 was terminated after exactly 2 years. The measured dry density distribution after sampling is shown in Figure 4-18.

Adapting a linear relation of the measured dry density distribution in Figure 4-18 yields the dashed line reaching between 27 mm and 220 mm (red hatched line) or a transition zone with the length 193 mm.

The swelling pressure was not measured in test FLR5. However, it was measured in test FLR2, which is identical to test FLR5. The measured swelling pressure up to the time for the termination of test FLR5 is shown in Figure 4-19. The swelling pressures at termination are compiled in Table 4-2.

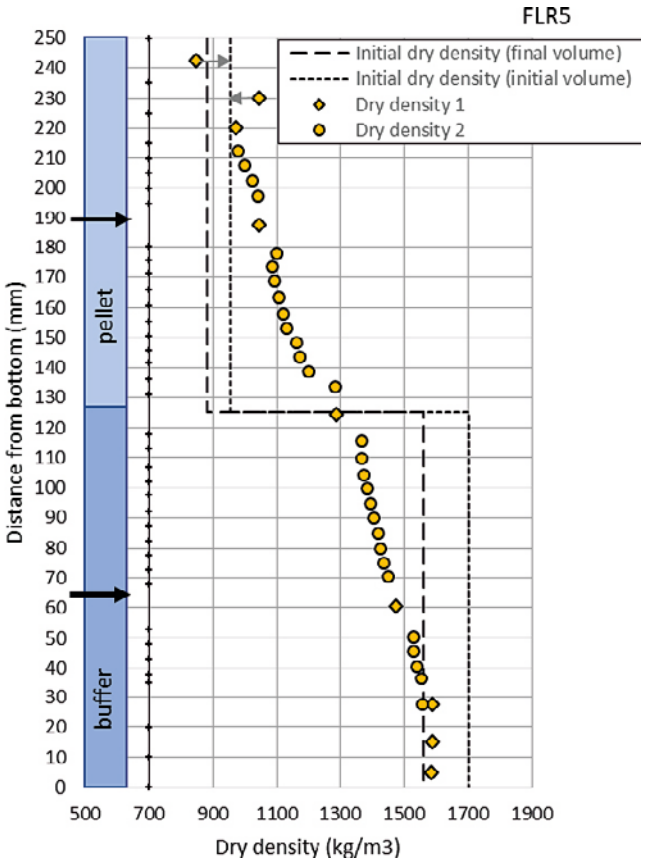

Figure 4-18. *Measured dry density distribution of test FLR5. Dry density 1 is actual measured dry density. Dry density 2 is back-calculated dry density from the water content assuming 100 % degree of saturation.*

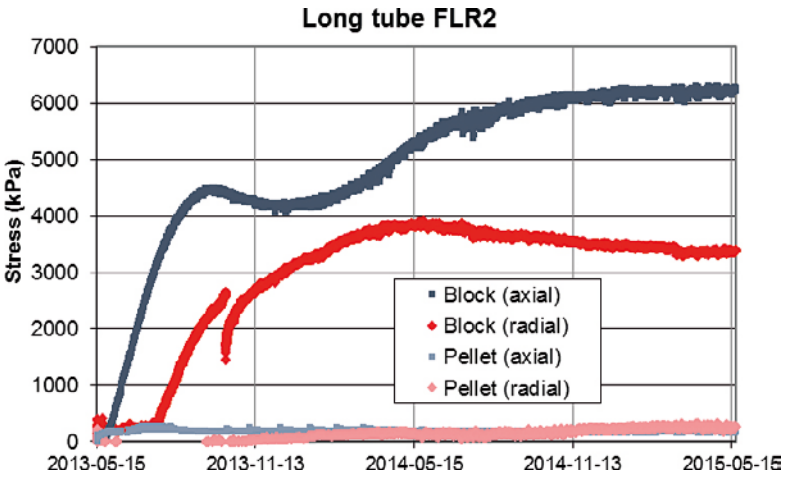

Figure 4-19. *Measured swelling pressure in test FLR2 up until the time for the termination of test FLR5. The locations of the transducers are shown in Figure 4-12.*

Table 4-2. Swelling pressure from test FLR2 measured with a similar set-up as FLR5 at a time corresponding to the termination of test FLR5.

Type	Distance (mm)	Swelling pressure (kPa)	Direction	Label
pellet	250	179	axial	FLR2 pellet (axial)
pellet	187.5	247	radial	FLR2 pellet (radial)
block	62.5	3381	radial	FLR2 block (radial)
block	0	6231	axial	FLR2 block (axial)

4.4.4 Finite element modelling

The test was also modelled with Abaqus. This modelling has not been previously reported and is described in this section.

The test was modelled with simplified initial conditions. The bentonite was assumed to be completely water saturated from start. The reason is that modelling of unsaturated bentonite with large swelling is not well developed.

The degree of saturation of the highly compacted specimen was very high and after adding water close to 100 % for both the pellet part and the compacted specimen part, so the model of saturated bentonite could be used. See Dueck et al. (2018).

The material model of the highly compacted bentonite specimen is identical to the one derived from the fundamental swelling tests and used in the modelling of the self-healing test (Börgesson et al. 2019).

The *hydraulic conductivity* relation is shown in Table 4-3.

Table 4-3. Hydraulic conductivity as a function of void ratio.

e	*k* (m/s)
0.45	0.5×10^{-14}
0.70	4.0×10^{-14}
1.00	2.0×10^{-13}
1.5	1.0×10^{-12}
2.00	0.5×10^{-11}
3.00	1.0×10^{-11}
5.00	3.5×10^{-11}
10.00	1.5×10^{-10}
20.00	0.75×10^{-9}

The mechanical model is a Porous Elastic model combined with the Claytech Plastic Cap model for the highly compacted specimen and with the Drucker-Prager model for the pellets. The reason for using Drucker-Prager for the pellets is convergence problems with the other model for the pellet part.

Porous Elastic implies a logarithmic relation between the void ratio e and the average effective stress p according to Equation 4-19.

$$\Delta e = -k \cdot \Delta \ln p \qquad (4\text{-}19)$$

where k = porous bulk modulus.

Poisson's ratio v is also required.

$k = 0.175$

$v = 0.3$

This relation is not valid for low densities (see Börgesson et al. 1995) but only in the interval $0.7 < e < 1.5$, which correspond to 1 110 kg/m^3 < ρ_d < 1 635 kg/m^3. At lower densities the porous bulk modulus is much larger so for the pellet filling another value has been used.

$k = 1.2$

The *Claytech Plastic Cap* model and its background are described in detail in Börgesson et al. (1995, 2019).

The calibrated parameters of the model (Börgesson et al. 2019) are:

a = 2.45

c = 2.20

b = 0.77

K= 1.0

γ = 0.2

R = 0.1

p_b = 30 000 kPa

p_f = −25 000 kPa

Cap hardening = see Table 4-4.

Table 4-4. Cap hardening function.

p (kPa)	$e_{\log(1+\varepsilon^{v}_{pl})}$
100	0
331	0.1133
934	0.2112
2 160	0.2904
3 247	0.3289
4 294	0.3553
8 240	0.4169
10 044	0.4356
12 530	0.4565
13 299	0.4621
17 562	0.4884
30 000	0.5390

The Drucker-Prager model is described by Börgesson et al. (2019).

The *initial conditions* used in the modelling were the following:

Highly compacted bentonite specimen

- e = 0.636
- u = −17 000 kPa
- S_r = 1.0
- p = 17 000 kPa

Bentonite pellets

- e = 2.6
- u = −80 kPa
- S_r = 1.0
- p = 80 kPa

The used void ratios differ somewhat from the final ones used in the test but the calculation was done before this test was started and was thus a true prediction.

Element model

The element model is shown in Figure 4-20. The highly compacted bentonite specimen is modelled with a radius that is 0.5 mm smaller than the inner diameter of the tube. The contact between the bentonite and the tube is modelled with contact surfaces with the friction angle $\phi = 9^{o}$.

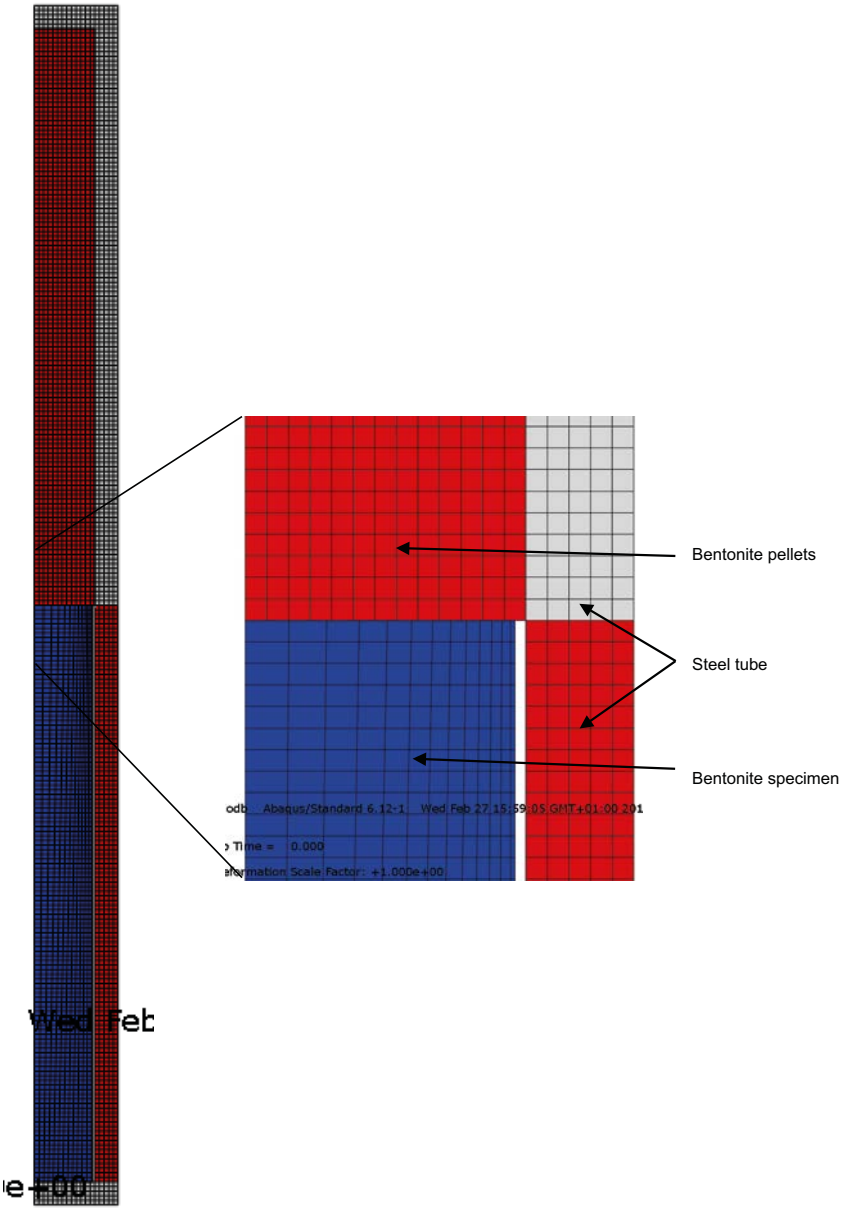

Figure 4-20. *Element mesh of the test FLR5. The model is axial symmetric with the symmetry axis around the left border. The right figure is a magnification of the contact part between the bentonite specimen and the pellets.*

Results

The modelled displacement of the boundary between the highly compacted bentonite and the pellets is shown as a function of the time from start of the test in Figure 4-21. The figure shows that the boundary has displaced a little more than 10 mm and that equilibrium had been reached at that time, which agrees rather well with the time to equilibrium of the measured stresses in the test shown in Figure 4-19.

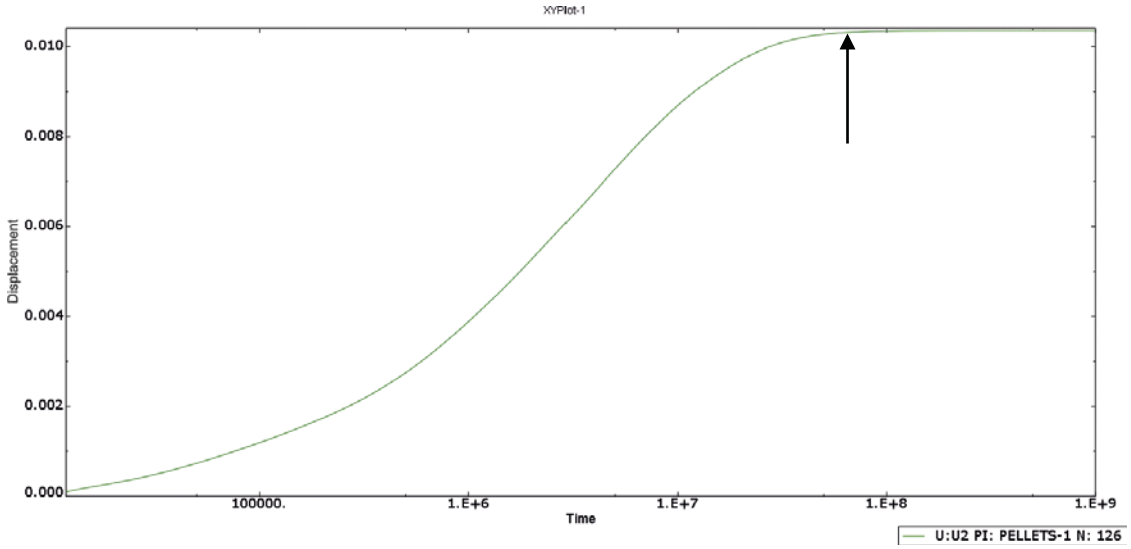

Figure 4-21. *Plot of the modelled displacement (m) of the boundary between the highly compacted bentonite and the pellets as a function of the time (s) from start of the test. The time for termination of the test (two years corresponding to* 6.3×10^7 *seconds) is marked with an arrow.*

The modelled void ratio distribution and dry density distribution at the end of the calculation (10^9 seconds) is shown in Figure 4-22 and Figure 4-23. The distribution of axial and radial stress is shown in Figure 4-24 and Figure 4-25.

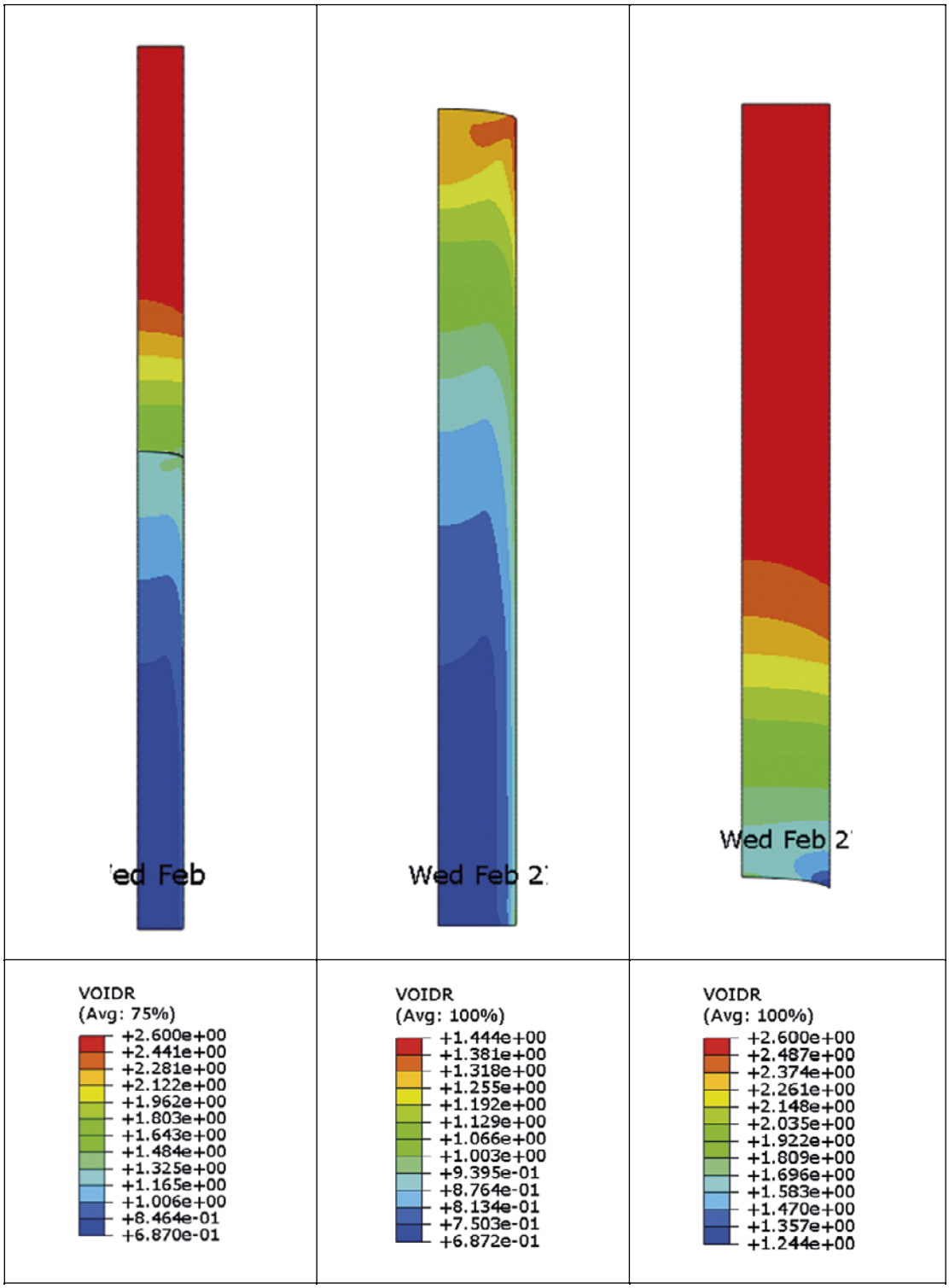

Figure 4-22. *Modelled void ratio distribution after a long time (10^9 seconds). The left figure shows the entire test while the other figures show only the highly compacted bentonite part (central) and the pellet part (right).*

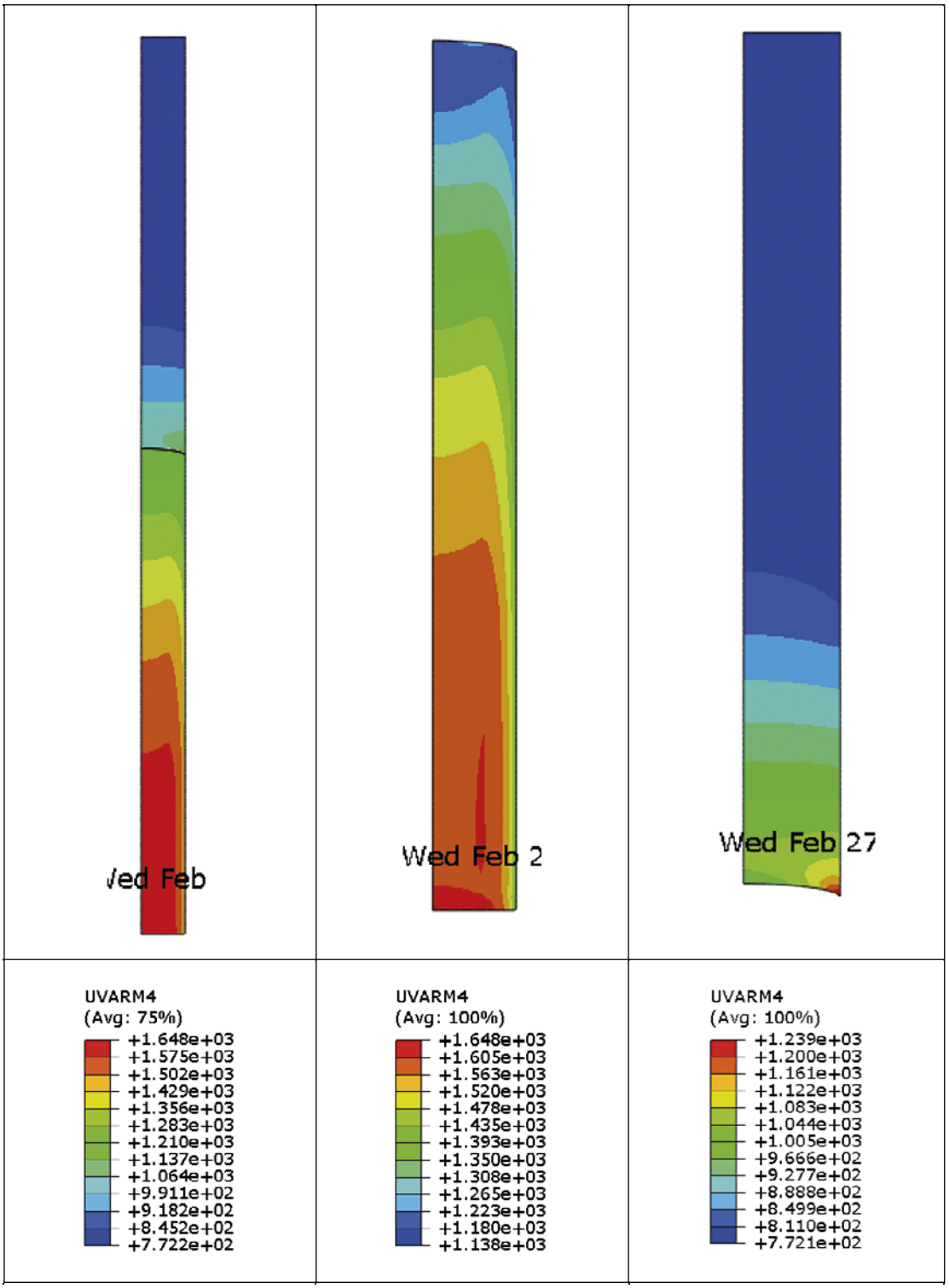

Figure 4-23. *Modelled dry density distribution (kg/m3) after a long time (10^9 seconds). The left figure shows the entire test while the other figures show only the highly compacted bentonite part (central) and the pellet part (right).*

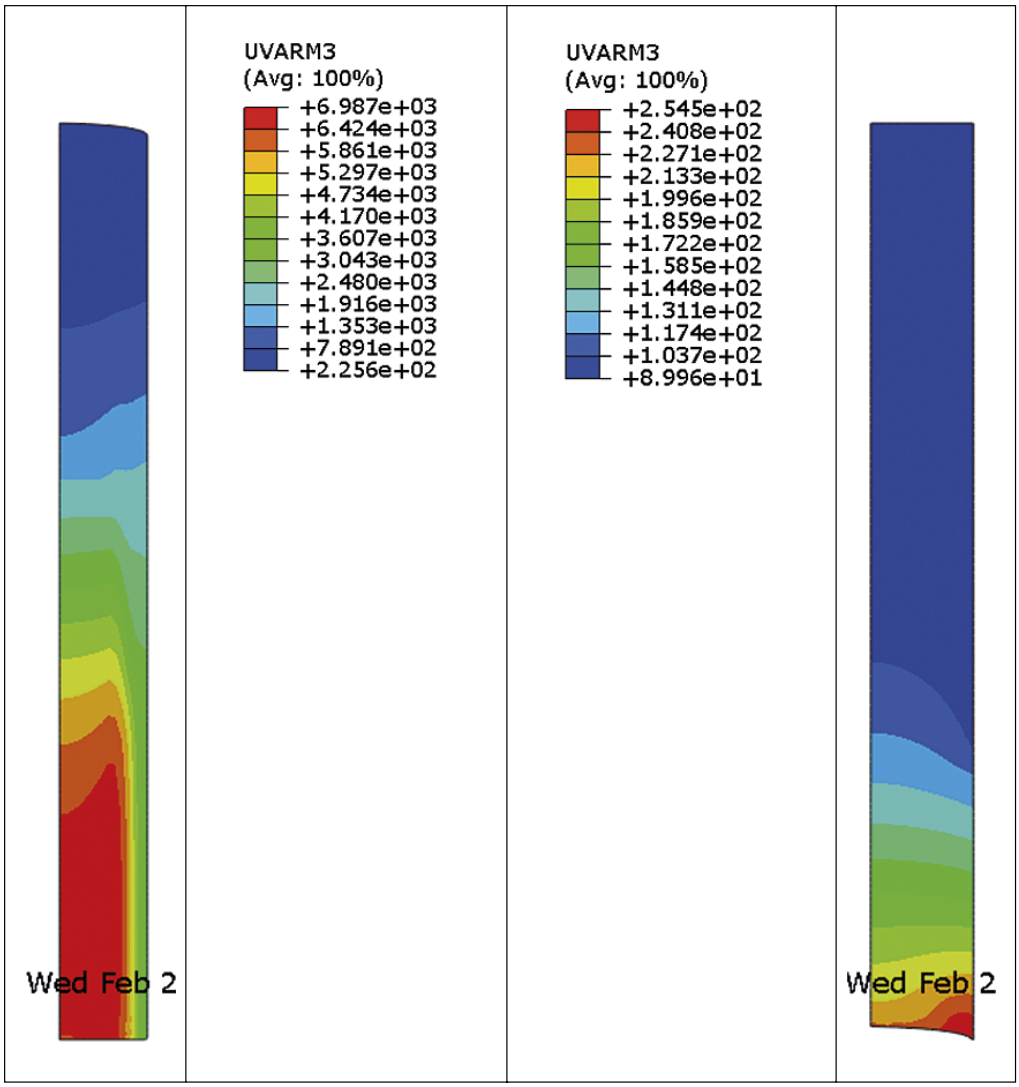

Figure 4-24. *Modelled axial stress (kPa) distribution after a long time (10^9 seconds). The left figure shows the highly compacted bentonite part and the right figure shows the pellet part (right).*

The final axial distribution of the void ratio along the centre line and the periphery is shown in Figure 4-26 as a function of the distance to the axial boundaries.

Figure 4-22 to Figure 4-25 show that the model predicts a density gradient both in radial and axial direction. That is logical since there was both axial and radial swelling of the highly compacted bentonite (HCB). Figure 4-26 shows that there is a rather large difference in void ratio in the center and in the periphery of the HCB but not in the pellets. The axially affected part (with a void ratio gradient) of the pellets goes from the contact zone at 0 m to about 0.06 m while corresponding part of the HCB goes from about 0.05 to the boundary located at 0.135. This means that the length of the affected part (the transition zone) is $L = 0.06 + (0.135–0.05) = 0.145$ m.

If the average friction angle is evaluated according to Equation 4-16 from the FEM derived $L = 0.145$ m we will have $\phi = 9.5°$, which agrees very well with the friction angle used in the FEM modelling $\phi = 9.0°$.

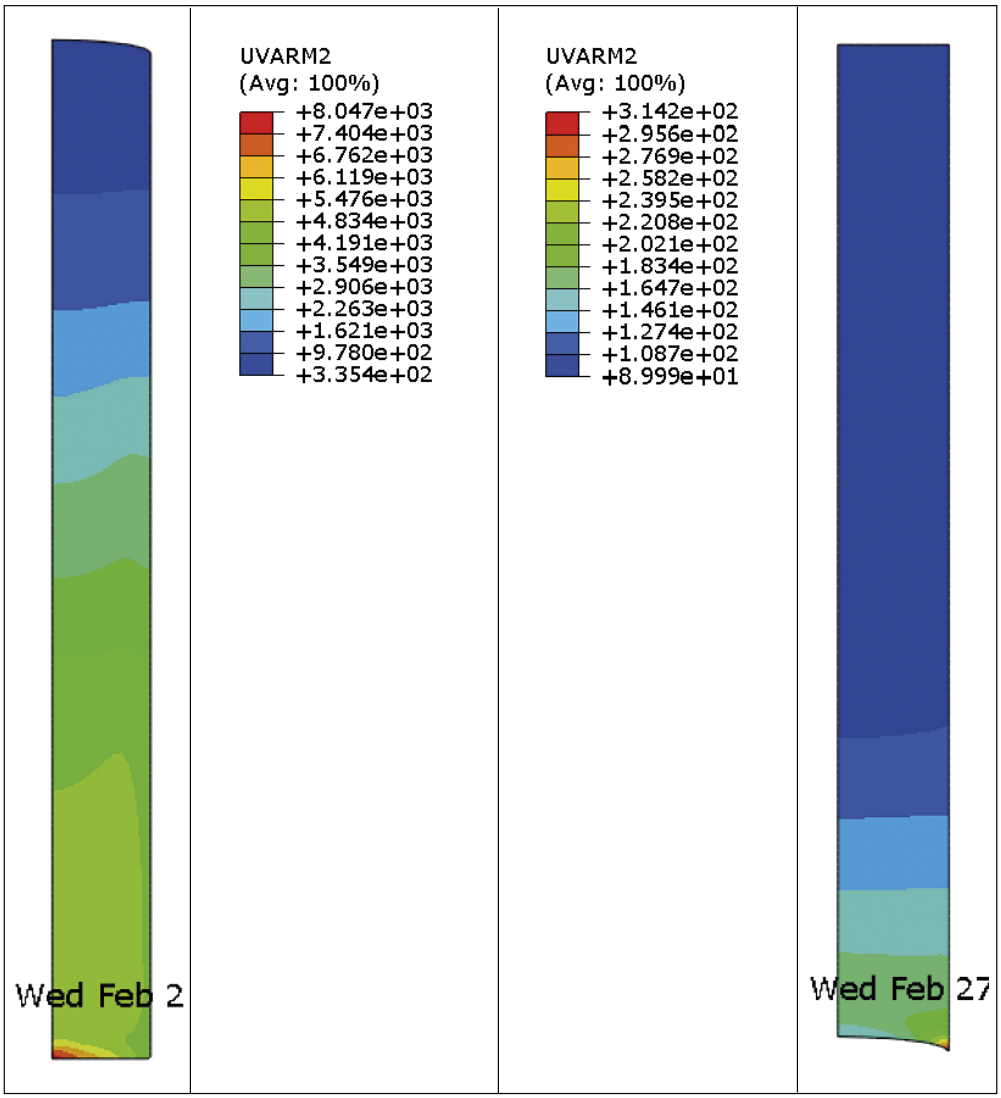

Figure 4-25. *Modelled radial stress (kPa) distribution after a long time (10^9 seconds). The left figure shows the highly compacted bentonite part and the right figure shows the pellet part (right).*

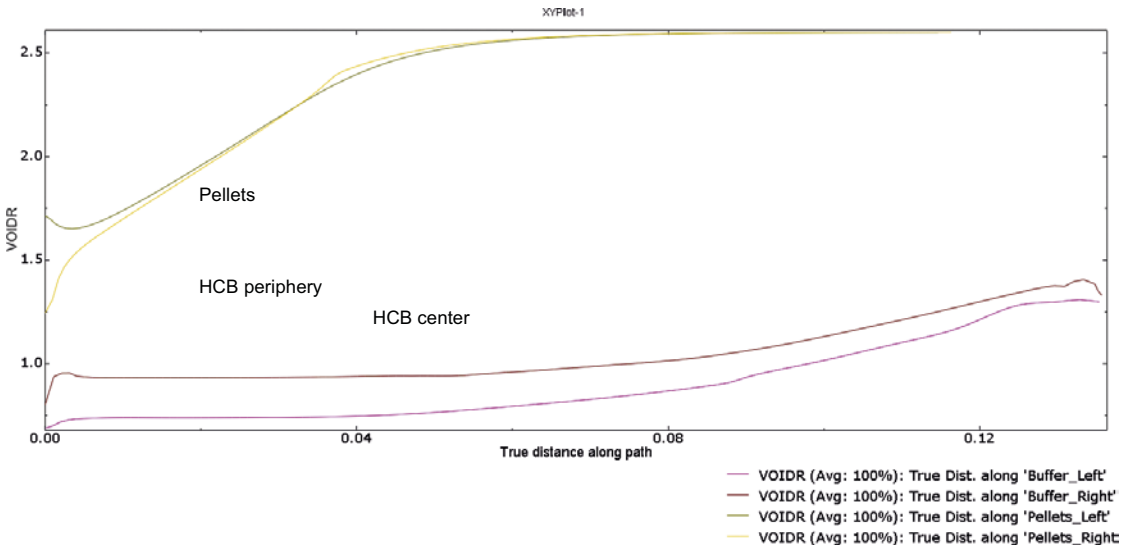

Figure 4-26. *Void ratio distribution as a function of the distance (m) from the lower boundaries for both the highly compacted bentonite (HCB) and the pellets.*

4.4.5 Discussion and conclusions

The length of the transition zone measured in test FLR5 was longer than modelled by FEM as shown in Figure 4-18 or L = 0.193 m. This measured length L = 0.193 m yields the average friction angle ϕ = 7.2º according to Equation 4-16. As such, the friction angle used in the FEM model was too high. No additional calculation has been done but ϕ = 7.2º instead of ϕ = 9.0º would yield better agreement.

The measured and FEM modelled swelling pressures are compared in Table 4-5.

Table 4-5. Modelled swelling pressure and measured from test FLR2 with a similar set-up as FLR5 at a time corresponding to the termination of test FLR5.

Section	Distance (mm)	Direction	Measured pressure (kPa)	Modelled pressure (kPa)
pellets	250	axial	179	90
pellets	187.5	radial	247	90
HCB	62.5	radial	3381	3650
HCB	0	axial	6231	≈ 6000

The measured and modelled swelling pressures do not agree very well for the pellets, mainly since a higher void ratio was used in the model. They agree better for the HCB section but also here there were some differences between the actual initial density and the modelled.

A comparison between the FEM-modelled and the analytical results are shown in Figure 4-27. In Figure 4-28 also the measured results are included.

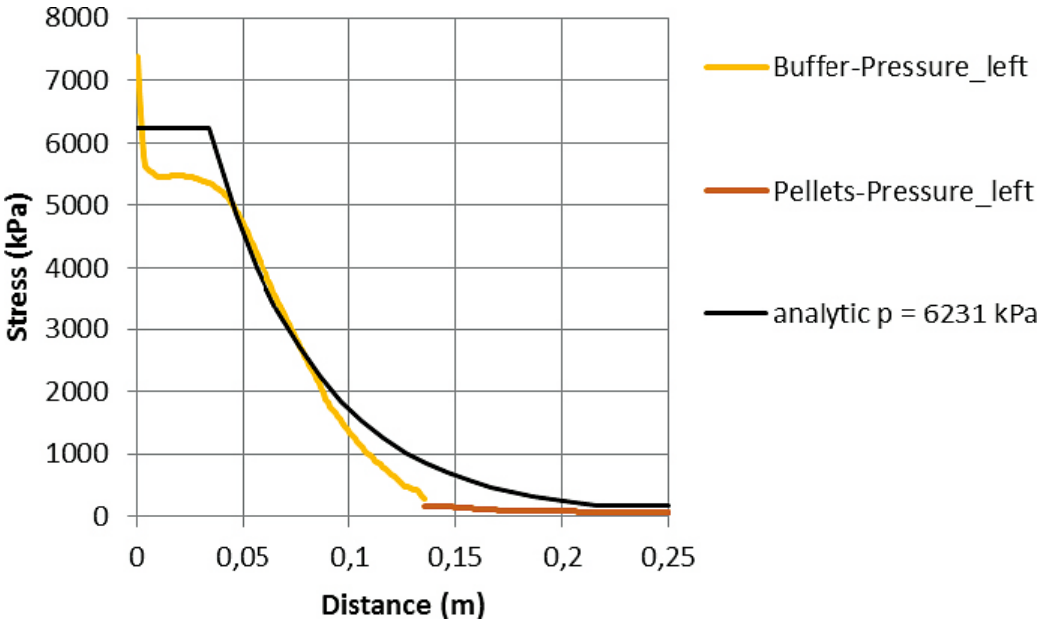

Figure 4-27. *Comparison between the analytical results and the FEM-results regarding average stress.*

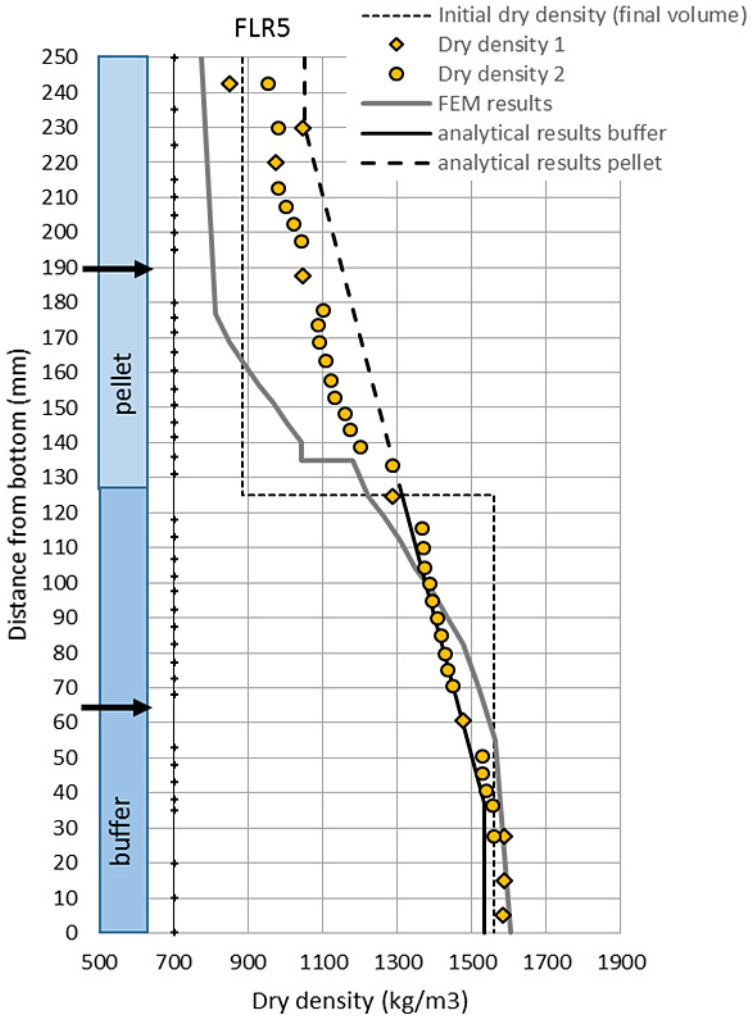

Figure 4-28. *Modelled (both analytical and FEM) and measured density distribution. See also Figure 4-18.*

The figures show that there is quite a difference between the two methods and that the measured values are in between. The analytical results of the dry density agree very well for the HCB part, while the modelled dry density of the pellets part is higher than the measured. The disagreement for the pellets part is caused by Equation 4-3, which is not valid for such low densities. In order for the stresses to agree (which is required since the relation is based on stress equilibrium) the dry density was increased as can be seen by the results.

The disagreement for the FEM-calculation is mainly caused by the too high friction angle used. In addition, the used initial dry densities in the FEM-calculation differed from the test since the pellets density used was too low and the density of the HCB used was too high.

The modelling and the comparison between modelling results and measured results from the long tube tests show that the understanding of the homogenization processes is quite good. The rather simple analytical model of the tube with a swelling of the HCB zone and compression of the pellet zone that is counteracted by friction between the bentonite and the walls of the tube seems to be a very relevant way of predicting the final state of equilibrium and the distribution of bentonite density along the tube. A back-analysis of the results using the measured length of the transition zone $L = 0.193$ m and using the relation in Equation 4-16, derived from the equilibrium equations, gave an average friction angle between the bentonite and the inner grooved surface of the steel tube $\phi = 7.2^{o}$. Figure 4-29 shows the measured friction angle between MX-80 bentonite and different surfaces (Dueck et al. 2016) as a function of the pressure.

In Figure 4-29 the evaluated results of test FLR5 are included. The surface of the steel tube in that test corresponds to the tests with grooves marked with yellow and orange marks of the friction tests. It is obvious that the peak values (marks with borders) of those grooved surfaces correspond very well to the internal friction angle of the bentonite materials, which is logical since there has to be a failure in the bentonite for start sliding. The residual values are close to half the peak values. The results of the test FLR5 agree rather well with the residual values. This is also logical since there has to be sliding in order to start swelling and homogenization.

One open question mark has been if the swelling is so slow that the peak strength of the bentonite is regained during the homogenization. The results from test FLR5 clearly indicates that this is not the case. The conclusion is thus that the residual friction angles corresponding to about half the internal friction angle in the bentonite shall be used for homogenization calculations even if a very raw surface is present.

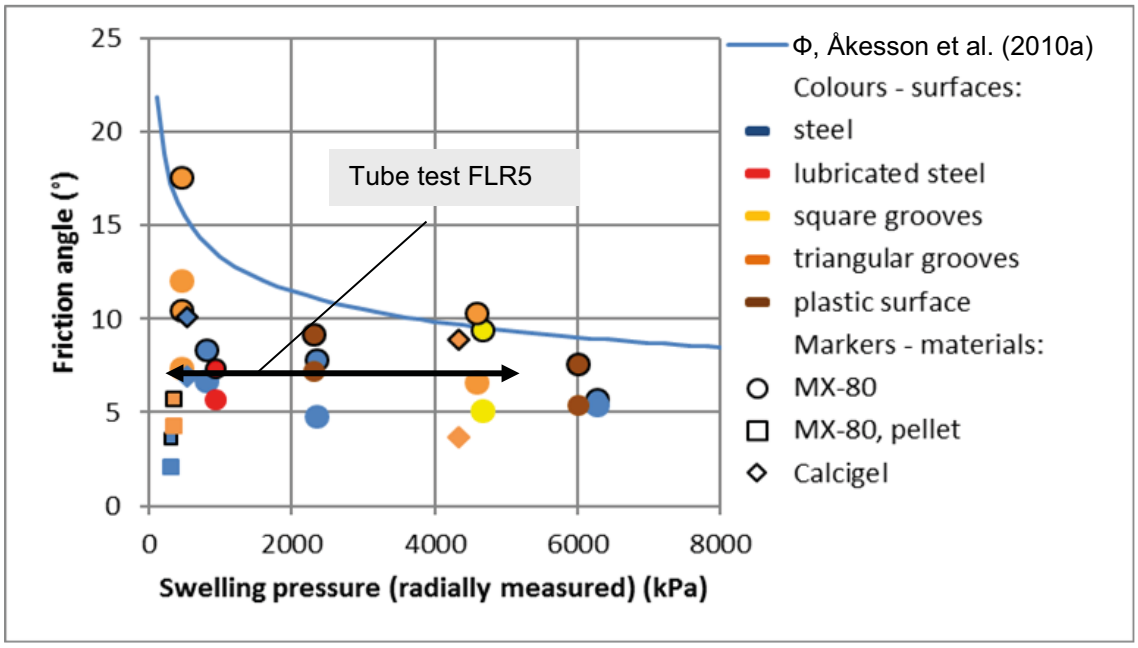

Figure 4-29. *Measured friction angle between different bentonites and different surface structures. The different colors correspond to different surfaces. The marks with borders are peak values and the marks without border are residual values. The black line arrow marks evaluated friction angle and the swelling pressure distribution along the steel tube for test FLR5.*

5 Material model development, implementation and evaluation – COMSOL

Mechanisms governing the homogenization process (of the dry density) are active on the microscopic scale of the clay. The swelling of the bentonite is caused by the hydration of the interlayer cations and the osmotic transport of water into the interlayer solution. The water affinity is in turn caused by the negative layer charge of the montmorillonite which is balanced by cations located in the interlayer space. It is important to note that these processes can occur under either unsaturated or saturated conditions, i.e. with or without the presence of a gas phase in the material.

The homogenization process however is studied on a larger, component, scale. The initial state of the systems is commonly highly heterogenic and during the homogenization process they undergo large changes in void ratios and water contents. Some level of remaining heterogeneity is generally expected also after that the system has attained equilibrium.

Reliable hydro-mechanical modelling of the evolution of the systems requires a material model that can represent the macroscopic behaviour of the bentonite for a wide range of states in order to obtain a robust modelling tool with a high predictive capability.

In the past SKB has studied the homogenization process numerically in a number of projects, e.g. SR-Site, TBT, CRT, SFR, Febex in situ test, Domplu and KBS-3H. Beside the modelling by the code Abaqus the FEM-code Code_Bright (CB) has been used. In those projects simulations have been carried out using a modified version of the Barcelona Basic material model (BBM) (Alonso et al. 1990), implemented within the numerical solver Code_Bright . It has, however, long been known that there are limits for this basis, see for instance Åkesson et al. (2010a) and Kristensson (2011), but with some modification of the BBM model present in CB, it has been possible to obtain reasonable representations for the systems and conditions/processes we have focused on in the previous work. The Barcelona Expansive Model (BExM), which was developed for expansive soils (Alonso et al. 1999), is also implemented and applicable in CB.

Still, both BBM and BExM display some major limitations (see Börgesson et al. 2019). For instance, there are generally no defined void ratio dependencies for the parameters, although both the swelling pressure and the shear strength of the bentonite are strongly related to the void ratio.

A second general limitation is that water saturated conditions cannot be represented with suction values higher than zero, although this is a normal behaviour for this type of material. Moreover, an accurate representation of loading and unloading at constant water content and saturated conditions means that the suction increment is equal to the negative value of the stress increment. In the case of BBM, such a behavior requires a tuned set of parameter values for the retention curve, the compression property (κ_i) and the swelling property (κ_s). For the BExM, however, this type of behavior follows directly from the use of effective stress as a governing variable for the micro-structure.

Finally, BBM has no mechanism for the yield surface to contract during isotropic swelling. With BExM, on the other hand, this is indirectly taken into account through the double porosity description and the interaction function. However, the strain softening, which means that the pre-consolidation stress (p_0^*) decreases, is in BExM attributed to the macro voids, even if all the pore space is water-filled. This means that the division of the void space in micro and macro voids must be defined and calibrated together with the interaction function in order to accurately describe an irreversible swelling/consolidation loop. A more adequate definition of the double porosity would however be based on the fluid in each of the void types, i.e. water in micro voids and gas in macro voids. This limits the prospects for attaining a consistent representation of swelling/consolidation processes at water-unsaturated conditions.

In order to meet the requirements that the new EBS-TF homogenization tasks demand, a model that has its basis in thermodynamics and mechanics has been developed (Börgesson et al. 2019). There have been a lot of indications and proposals in the past that a proper bentonite material model should have a basis in such a framework (e.g. Low and Andersson 1957, Kahr et al. 1990, Dueck 2004, Birgersson et al. 2010, Åkesson et al. 2010a, Kristensson 2013). For bentonite materials it turns out that when using this approach, it results in an intimate connection between swelling pressure and the retention properties, two entities which we know describe the main characteristics of the material.

The new model, denoted the Hysteresis Based Material (HBM) model, has been developed with the aim to obtain a robust hydro-mechanical model for high density bentonite materials, with a high predictive capability. The HBM model was defined for water saturated conditions by making the following three basic assumptions:

1) The model is based on an expression for the *chemical potential* of the clay water and its pressure dependence. From this follows that the sum of *suction* (s) and *pressure* (p) is equal to a quantity, denoted the *clay potential* (Ψ), which in turn is a function of the void ratio (e), $s + p = \Psi(e)$. This means that the clay potential is equal to the suction value at unconfined conditions, ($p = 0$), and also that it equals the pressure at confined conditions with free access of water, ($s = 0$). The swelling pressure curve and the water retention curve can thereby be viewed as two sides of the same coin. It can also be noted that this relation is analogous to the effective stress concept according to which the deformations are governed by changes in effective stress, i.e. the difference between the (total) stress and the pore pressure.

2) In order to obtain a description which captures the *hysteretic behaviour* (path dependency) observed in oedometer tests and water retention measurements, and the *shear strength* observed in unconfined compression tests and triaxial tests, the following assumptions have been adopted.

(i) The clay potential for a specific void ratio is assigned a value in an *allowed interval bounded by two functions*. One function during swelling conditions (Ψ_L) and the other for conditions during consolidation (Ψ_H).

(ii) The actual state between these functions for a given direction is governed by the *history of the strains* in that direction.

(iii) The difference between the states in different directions *should not exceed half the allowed interval (i.e.* $\Psi_{\Delta/2} = \frac{(\Psi_H - \Psi_L)}{2}$).

3) The *density of water* is defined as a function of suction, i.e. $\rho_w(s)$. This means that the compressibility of water ($\partial\rho_w/\partial s$) is assumed to be applicable for positive suction values as well as for positive pore pressures (which basically are equivalent to negative suction values).

Models of the homogenization process also include a hydraulic part in which the flow of water is governed by *Darcy´s law*. An empirical relation between the hydraulic conductivity and the void ratio is used for this process.

Remaining uncertainties of the model and implementation have not been addressed at the time of writing this report. The project is in a developing phase where both planned and unplanned alterations will take place in the future.

Chapter 5 contains a description of the developed material model (5.1), the implementation into COMSOL Multiphysics (5.2), and the testing/evaluation of the implementation (5.3 and 5.4). More details regarding the theoretical framework and COMSOL implementation can be found in Appendix 2 and Appendix 3, respectively.

5.1 Mechanical material model

The *chemical potential of the clay water* (μ) was used as a starting point for the mechanical material model. For isotropic conditions, this can be described as a function of the *relative humidity of the clay at free swelling conditions* (RH) and the *mechanical pressure* (p) (e.g. Birgersson et al. 2010):

$$\mu = \mu_0 + RT\ln(RH) + v_c p \ \text{[J/mol]} \tag{5-1}$$

where μ_0 is the chemical potential of a reference state, R is the universal gas constant, T is the absolute temperature and v_c is the molar volume of the clay water. The relation above can be rearranged as,

$$-\frac{\mu - \mu_0}{v_0} = -\frac{RT}{v_0}\ln(RH) - \frac{v_c}{v_0}p \tag{5-2}$$

where v_0 is the molar volume of bulk water measured in m^3/mol. The term on the left-hand side can be identified as the liquid *suction* (s), while the first term on the right side from here on is denoted the *clay potential* (Ψ [Pa]). Assuming that v_0 and v_c are equal in the compacted clay systems that we

consider (which is supported by the findings of Croney et al. (1958), Kassiff and Shalom (1971) and Dueck (2004)) the expression above can be written as:

$$s = \Psi - p \tag{5-3}$$

It should be noted that the suction corresponds to the relative humidity in an external gas phase. It also corresponds to the negative value of an external water pressure. This means that the clay potential is defined in a similar way as an *effective stress*. It should also be noted that this description is based on the assumptions that the osmotic effect of any solution in the water can be disregarded and that the temperature is constant. In this preliminary description an *isotropic* stress state is also assumed.

Now, focusing on how to design a proper expression describing the clay potential, we begin with discussing experimental findings regarding *RH*, the relative humidity of the clay at free swelling conditions. Common traits of experimental data for *RH* are: dependency on the *water content* (*w*) and presence of a hysteresis effect, i.e. path dependency. This means that *RH* depends on the current *w*-value as well as the history of *w* which the sample has experienced. To indicate that the entire history of a variable up to time *t* is to be regarded, the variable is given a superscripted *t*, e.g. w^t. Using this notation, we can write the experimentally motivated findings for the relative humidity of the clay at free swelling conditions as:

$$RH = \widetilde{RH}(w, w^t) \tag{5-4}$$

In the case of water saturated conditions, which have been considered in the present work, *w* can be substituted with the void ratio (*e*), which gives

$$RH = \widetilde{RH}(e, e^t) \tag{5-5}$$

Using the known properties of *RH* and its relation to the clay potential, i.e.

$$\Psi = -\frac{RT}{v_0}\ln(RH) \tag{5-6}$$

the clay potential function is expressed as:

$$\Psi = \widetilde{\Psi}(e, e^t) \tag{5-7}$$

When designing the actual expression for the clay potential function the following format was found to be suitable:

$$\widetilde{\Psi}(e, e^t) = \widetilde{\Psi}_M(e) + \widetilde{\Psi}_{\Delta/2}(e)\tilde{f}(e^t) \tag{5-8}$$

Ψ_M, $\Psi_{\Delta/2}$ and *f*, variables given by the corresponding function above, are denoted the *mid-line*, the *half-allowed span*, and the *path variable*, respectively. It can be noted that Ψ_M, and $\Psi_{\Delta/2}$ are defined by functions of the void ratio, whereas *f* is a variable, with values belonging to [−1,1], dependent on the void ratio history. The clay potential is thus confined to a region with two bounding lines: $\Psi_H = \Psi_M + \Psi_{\Delta/2}$ (the consolidation line obtained when $f = 1$) and $\Psi_L = \Psi_M - \Psi_{\Delta/2}$ (the swelling line obtained when $f = -1$), see Figure 5-1.

The path variable (*f*) is obtained by integration over time, starting from the initial condition $f_0 = f(\tau = t_0)$,

$$f = f_0 + \int_{t_0}^{t} \frac{\partial f}{\partial e}\dot{e}\, d\tau \tag{5-9}$$

where the differential is given by,

$$\frac{\partial f}{\partial e} = -\frac{K'}{1 + e_0}(1 + \mathrm{sgn}(\dot{e})f) \tag{5-10}$$

The unitless *K′*-parameter determine the path variable derivative at $f = 0$, the sign of the time derivative of the void ratio determines whether the value of *f* changes towards 1 or −1. The sign function is defined as:

$$\mathrm{sgn}(x) = \begin{cases} -1 & \text{if} \quad x < 0 \\ 0 & \text{if} \quad x = 0 \\ 1 & \text{if} \quad x > 0 \end{cases} \tag{5-11}$$

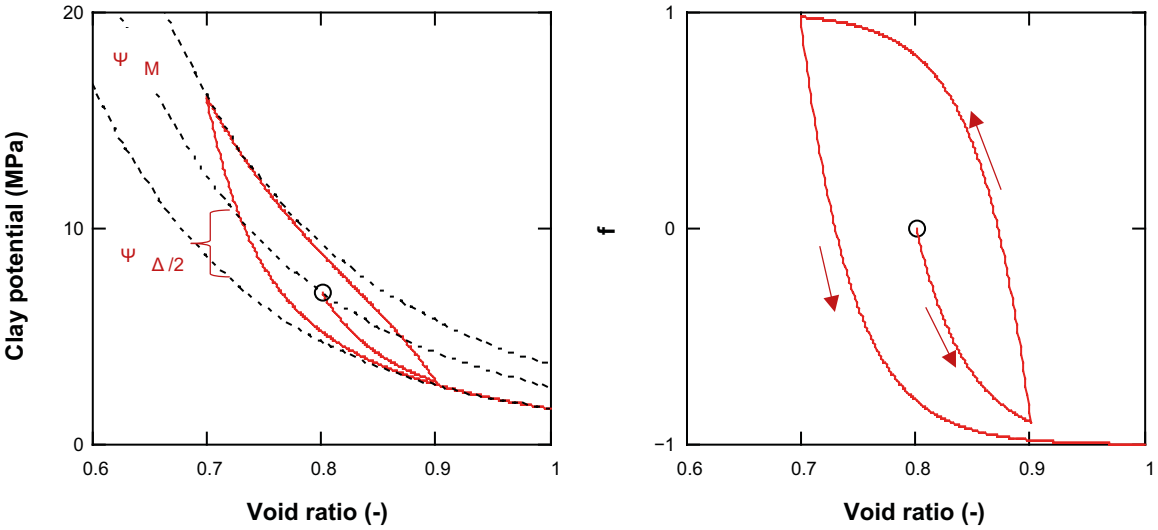

Figure 5-1. *Clay potential and path variable (f) versus void ratio. Right graph shows an example of the path variable for a case with swelling, followed by consolidation and followed by swelling. Left graph shows the same path mapped on the region for the clay potential.*

5.1.1 Clay potential function contributions

The clay potential function, $\tilde{\Psi}(e,e^t)$, is linked to experimentally motivated swelling pressure curves, $\tilde{p}_{sw}^{high}(e)$ and $\tilde{p}_{sw}^{low}(e)$, dependent on the void ratio, on the format,

$$\tilde{p}_{sw}^{\beta}(e) = 10^{c_0^{\beta}+c_1^{\beta}\frac{\rho_s}{1+e}+c_2^{\beta}\left(\frac{\rho_s}{1+e}\right)^2} \tag{5-12}$$

where β = *high, low.*

The parameters c_0^{β}, c_1^{β} and c_2^{β} are fitting parameters calibrated from the measured swelling pressures during swelling/wetting (β = *low*) and compression/drying (β = *high*). They are defined such that the exponent in Equation 5-12 is unitless.

As described above Equation 5-8 was found to be a suitable expression for the clay potential.

The mid curve variable Ψ_M and span variable $\Psi_{\Delta/2}$ in Equation 5-8 are given by,

$$\Psi_M = \frac{p_{sw}^{high} + p_{sw}^{low}}{2} \tag{5-13}$$

and

$$\Psi_{\Delta/2} = \frac{p_{sw}^{high} - p_{sw}^{low}}{2} \tag{5-14}$$

respectively. For the incremental format that is derived below we need the following derivatives,

$$\frac{\partial \Psi_M}{\partial \varepsilon_v} = \frac{\partial \Psi_M}{\partial e}\frac{\partial e}{\partial \varepsilon_v} = \frac{1}{2}\left(\frac{\partial p_{sw}^{high}}{\partial e} + \frac{\partial p_{sw}^{low}}{\partial e}\right)\frac{\partial e}{\partial \varepsilon_v} \tag{5-15}$$

and

$$\frac{\partial \Psi_{\Delta/2}}{\partial \varepsilon_v} = \frac{\partial \Psi_{\Delta/2}}{\partial e}\frac{\partial e}{\partial \varepsilon_v} = \frac{1}{2}\left(\frac{\partial p_{sw}^{high}}{\partial e} - \frac{\partial p_{sw}^{low}}{\partial e}\right)\frac{\partial e}{\partial \varepsilon_v} \tag{5-16}$$

In Equations 5-15 and 5-16 the derivative of the void ratio with respect to the volumetric strain is given by:

$$\frac{\partial e}{\partial \varepsilon_v} = 1 + e_0 \tag{5-17}$$

and the derivatives of the swelling pressure curves are:

$$\frac{\partial \tilde{p}_{sw}^{\beta}}{\partial e} = -\tilde{p}_{sw}^{\beta}(e)\ln(10)\frac{\rho_s}{(1+e)^2}\left(c_1^{\beta} + 2c_2^{\beta}\frac{\rho_s}{1+e}\right) \tag{5-18}$$

where β = *high, low.*

5.1.2 Principal direction model

A generalized version of the isotropic model described above is outlined below. To make the description compact it is not given as a stand-alone text but should be read with the isotropic formulation above in mind and the information in Appendix 2 (Model development – Theoretical framework) as support if necessary.

The model applicable for isotropic conditions has been expanded to also cover cases when the principal directions correspond to the Cartesian basis $\{\boldsymbol{e}_1, \boldsymbol{e}_2, \boldsymbol{e}_3\}$. The generalized model reads:

$$-\boldsymbol{\sigma} = \boldsymbol{\Psi} - s\mathbf{1} \tag{5-19}$$

$$\boldsymbol{\Psi} = \widetilde{\Psi}_M(\varepsilon_v)\mathbf{1} + \widetilde{\Psi}_{\Delta/2}(\varepsilon_v)\boldsymbol{f} \tag{5-20}$$

$$\boldsymbol{f} = \boldsymbol{f}_0 + \int_{t_0}^{t} \frac{\partial \boldsymbol{f}}{\partial \boldsymbol{\varepsilon}} \dot{\boldsymbol{\varepsilon}}\, dt^* \tag{5-21}$$

In this version of the model the path dependent variable $\boldsymbol{f}$ is a second order tensor,

$$\boldsymbol{f} = f_{11}\boldsymbol{e}_1 \otimes \boldsymbol{e}_1 + f_{22}\boldsymbol{e}_2 \otimes \boldsymbol{e}_2 + f_{33} \otimes \boldsymbol{e}_3 \otimes \boldsymbol{e}_3 \tag{5-22}$$

and its derivative with respect to strain is given by,

$$\frac{\partial \boldsymbol{f}}{\partial \boldsymbol{\varepsilon}} = \frac{\partial f_{11}}{\partial \varepsilon_{11}}\boldsymbol{e}_1 \otimes \boldsymbol{e}_1 \otimes \boldsymbol{e}_1 \otimes \boldsymbol{e}_1 + \frac{\partial f_{22}}{\partial \varepsilon_{22}}\boldsymbol{e}_2 \otimes \boldsymbol{e}_2 \otimes \boldsymbol{e}_2 \otimes \boldsymbol{e}_2 + \frac{\partial f_{33}}{\partial \varepsilon_{33}}\boldsymbol{e}_3 \otimes \boldsymbol{e}_3 \otimes \boldsymbol{e}_3 \otimes \boldsymbol{e}_3 \tag{5-23}$$

The differential equations for the path variable components are given by:

$$\frac{\partial f_{\alpha\alpha}}{\partial \varepsilon_{\alpha\alpha}} = -K(\tilde{\kappa}(\boldsymbol{f}, \dot{\varepsilon}_{\alpha\alpha}) + \mathrm{sgn}(\dot{\varepsilon}_{\alpha\alpha})f_{\alpha\alpha}) \tag{5-24}$$

where $\alpha = \{1, 2, 3\}$ and no summation convention is to be used. The parameter K is unitless. In the expression above,

$$\tilde{\kappa}(\boldsymbol{f}, \dot{\varepsilon}_{\alpha\alpha}) = 1 - \Phi\big(\tilde{\gamma}(\boldsymbol{f}, \dot{\varepsilon}_{\alpha\alpha})\big)\tilde{\gamma}(\boldsymbol{f}, \dot{\varepsilon}_{\alpha\alpha}) \tag{5-25}$$

where Φ is the Heaviside step function, and the $\tilde{\gamma}$-function is defined as,

$$\tilde{\gamma}(\boldsymbol{f}, \dot{\varepsilon}_{\alpha\alpha}) = f_T + \mathrm{sgn}(\dot{\varepsilon}_{\alpha\alpha})f_P \tag{5-26}$$

f_T and f_p represents the "half-distance" and "mid-point" between the largest and smallest of the diagonal f-values, respectively, i.e.

$$f_T = \frac{\max(f_{\alpha\alpha}) - \min\big(f_{\beta\beta}\big)}{2} \tag{5-27}$$

and

$$f_P = \frac{\max(f_{\alpha\alpha}) + \min\big(f_{\beta\beta}\big)}{2} \tag{5-28}$$

where $\alpha = \{1, 2, 3\}$, $\beta = \{1, 2, 3\}$ and no summation convention is to be used. The purpose of the $\tilde{\kappa}$- and the $\tilde{\gamma}$-function is to limit the maximum difference between the f-values in different directions to 1, thereby making sure that the shear strength of the material is taken into account.

5.2 Implementation in COMSOL

The equation system describing the model to implement in COMSOL is given below together with brief comments relating to the implementation of the different parts, more information can be found in Appendix 3. In the subsequent chapter the implementation of the mechanical material model (providing the stress as a function of independent variables) is outlined.

Balance of solid mass:

The solid mass balance has been implemented as a user input equation to provide the updating scheme for the porosity.

$$\dot{\phi} = (1 - \phi)\, \dot{\varepsilon}_v \tag{5-29}$$

Balance of water mass:

The water mass balance has been implemented using Comsol's built-in Darcy's law physics interface, with the necessary coupling to the mechanical evolution added manually as a weak contribution;

$$\dot{\rho}_w \phi + \rho_w \phi \, \mathrm{div}(\dot{\boldsymbol{u}}_w - \dot{\boldsymbol{u}}_s) + \rho_w \dot{\varepsilon}_v = f_w \tag{5-30}$$

Balance of forces:

COMSOL's built-in Solid Mechanics interface was used to solve the force balance The equation solved for is:

$$\mathrm{div}\boldsymbol{\sigma} + \boldsymbol{b} = \boldsymbol{0} \tag{5-31}$$

Constitutive equation for flow of water in the porous media:

Darcy's law was implemented in connection with defining the water mass balance as a user input.

$$\dot{\boldsymbol{u}}_w - \dot{\boldsymbol{u}}_s = \tilde{\boldsymbol{q}}(s) \tag{5-32}$$

Constitutive equation for the water density:

This was implemented by the user input option.

$$\rho_w = \tilde{\rho}_w(s) = \rho_{w0} \exp(-\beta s) \tag{5-33}$$

Constitutive equation for the stresses, mechanics:

This was implemented using the available "General stress-strain relation" option.

$$d\boldsymbol{\sigma} = d\tilde{\boldsymbol{\sigma}}(d\boldsymbol{u}_s, ds, \boldsymbol{f}) \tag{5-34}$$

5.2.1 Mechanical material model implementation

The implementation of the material model into COMSOL is performed by using the available user defined "General stress-strain relation socket" which is described in Figure 5-2. Using the input in form of

$$(\boldsymbol{\varepsilon}^0, \boldsymbol{\varepsilon}^1, s^0, s^1, \boldsymbol{\sigma}^0, \boldsymbol{f}^0) \tag{5-35}$$

and material parameter values, the output,

$$(\boldsymbol{\sigma}^1, \boldsymbol{f}^1, \mathbb{C}^1) \tag{5-36}$$

should be calculated within the module. A superscripted 0 means that the variable belongs to the state at the beginning of the current time step and variables with 1 as a superscript belong at the end of the current time step.

Within the module the internal variable $\boldsymbol{f}$ and stress $\boldsymbol{\sigma}$ are updated from the known state, 0, to the unknown state, 1. Due to the nonlinearity of the model the updating is accomplished by integration of the incremental relations (described in Appendix 3),

$$\begin{aligned} \boldsymbol{f}^1 = \boldsymbol{f}^0 + \int_{\boldsymbol{f}^0}^{\boldsymbol{f}^1} d\boldsymbol{f}^* = \boldsymbol{f}^0 + \int_{\boldsymbol{\varepsilon}^0}^{\boldsymbol{\varepsilon}^1} \frac{\partial \boldsymbol{f}}{\partial \boldsymbol{\varepsilon}} d\boldsymbol{\varepsilon}^* \text{ and } \boldsymbol{\sigma}^1 = \boldsymbol{\sigma}^0 + \int_{\boldsymbol{\sigma}^0}^{\boldsymbol{\sigma}^1} d\boldsymbol{\sigma}^* \\ = \boldsymbol{\sigma}^0 + \int_{\boldsymbol{\varepsilon}^0}^{\boldsymbol{\varepsilon}^1} \mathbb{C} d\boldsymbol{\varepsilon}^* + \int_{s^0}^{s^1} \boldsymbol{1} ds^* \end{aligned} \tag{5-37}$$

GENERAL STRESS-STRAIN RELATION

The **General stress-strain relation** socket implements a stress-strain relation computing a second Piola-Kirchhoff stress tensor given the current Green-Lagrange strain together with a material property vector and a vector of stored states. The expected external material function signature is:

```
int eval(double *e,            // Green-Lagrange strain, input
         double *s,            // Second Piola-Kirchhoff stress, output
         double *D,            // Jacobian of stress with respect to strain,output
         int *nPar,            // Number of material model parameters, input
         double *par,          // Material model parameters, input
         int *nStates,         // Number of states, input
         double *states) { }   // States, input/output
```

The `e` and `s` tensors are given in Voigt order; that is., the components in `e` are $\{e_{xx}, e_{yy}, e_{zz}, e_{yz}, e_{xz}, e_{xy}\}$ and similarly for `s`. The Jacobian `D` is a 6-by-6 matrix of partial derivatives of components of `s` (rows) with respect to components of `e` (columns); the matrix is stored in row-major order.

Figure 5-2. *Description of the interface of the "General stress-strain relation socket" as given in the COMSOL user manual.*

The integration is approximated using a Euler forward scheme with sub-incrementation, i.e.

$$\boldsymbol{f}^1 \approx \boldsymbol{f}^0 + \sum_{\alpha=1}^{N} \left.\frac{\partial \boldsymbol{f}}{\partial \boldsymbol{\varepsilon}}\right|_{\alpha-1} \Delta\boldsymbol{\varepsilon}_\alpha \quad \text{and} \quad \boldsymbol{\sigma}^1 \approx \boldsymbol{\sigma}^0 + \sum_{\alpha=1}^{N} \mathbb{C}|_{\alpha-1}\Delta\boldsymbol{\varepsilon}_\alpha + \sum_{\alpha=1}^{N} \mathbf{1}\Delta s_\alpha \tag{5-38}$$

Here the final solution at 1 is obtained by performing subsequent updating from 0 to 1 in N substeps. The Jacobians are calculated at the beginning of the sub step (Euler forward) which is indicated by the notation $<\cdot>|_{\alpha-1}$.

In the implementation the variables are subsequently updated to the state at the end of the αth sub-step according to:

$$\left.\begin{aligned} \boldsymbol{f}^0{}_\alpha &= \boldsymbol{f}^0{}_{\alpha-1} + \left.\frac{\partial \boldsymbol{f}}{\partial \boldsymbol{\varepsilon}}\right|_{\alpha-1} \Delta\boldsymbol{\varepsilon}_\alpha \\ \boldsymbol{\sigma}^0{}_\alpha &= \boldsymbol{\sigma}^0{}_{\alpha-1} + \mathbb{C}|_{\alpha-1}\Delta\boldsymbol{\varepsilon}_\alpha + \mathbf{1}\Delta s_\alpha \end{aligned}\right\} \text{for } \alpha = 1, 2 \cdots N \tag{5-39}$$

where $\boldsymbol{f}^0_0 = \boldsymbol{f}^0$ and $\boldsymbol{\sigma}^0_0 = \boldsymbol{\sigma}^0$. The convergence criterion, which determines whether the solution should be accepted or not, is based on that the chosen norm of the difference in the stress solution from using N and $N/2$ subincrements should be less than a given tolerance, i.e.

$$\sqrt{\left(\boldsymbol{\sigma}^0{}_N - \boldsymbol{\sigma}^0{}_{N/2}\right) \cdot \left(\boldsymbol{\sigma}^0{}_N - \boldsymbol{\sigma}^0{}_{N/2}\right)} < tol \tag{5-40}$$

If the criterion is fulfilled, the solution is accepted as the updated state, i.e. $\boldsymbol{f}^1 = \boldsymbol{f}^0{}_N$ and $\boldsymbol{\sigma}^1 = \boldsymbol{\sigma}^0{}_N$.

If the criterion is not fulfilled for $N \le N_{MAX}$, where N_{MAX} is to be specified by the user, the module sends out an erroneous (NaN) stress component so that COMSOL decreases the time step taken from the known state and the integration procedure described above restarts.

5.3 Modelling of a consolidation test

The material model implementation in COMSOL was first tested/evaluated by simulating a consolidation test reported in Börgesson et al. (2015) using COMSOL Multiphysics version 5.3. The experiment was carried out as part of the System Design of the Dome Plug experiment in order to characterise the behaviour of the bentonite to be used in the sealing blocks (Börgesson et al. 2015).

The experiment was carried out by placing a pre-compacted bentonite block in a specially constructed test cell. Water was provided to the clay via filters at the two ends to achieve full saturation while maintaining a vertical stress of 4 MPa. After saturation the vertical stress was varied in steps, while allowing the bentonite to reach a new equilibrium for each load step. During the test displacement and radial pressure were measured and after the test was finished the water content and density was determined, allowing the calculation of void ratio, degree of saturation, dry density and saturated density.

To model the consolidation-test, a simple 2D axisymmetric geometry was constructed and meshed as shown in Figure 5-3, where also the boundary conditions are illustrated. The boundary stress applied on the top of the geometry was taken from the experimentally applied axial stress.

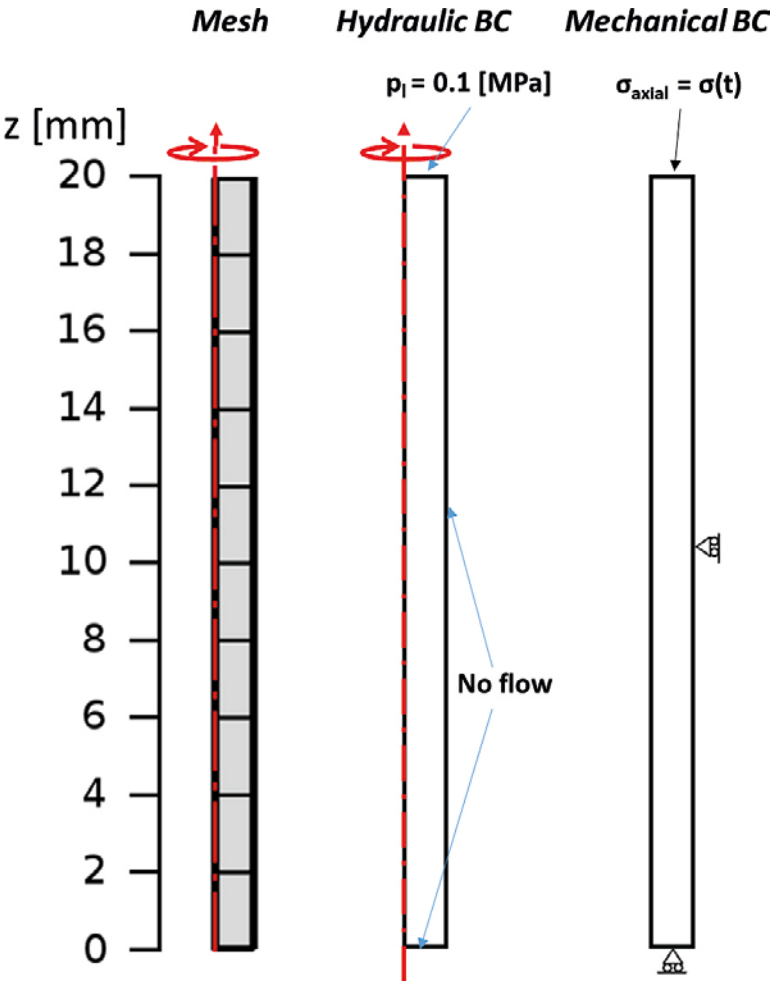

Figure 5-3. *Geometry and mesh (left), hydraulic boundary condition (middle) and mechanical boundary (right) used in the model of the consolidation test.*

The material parameters used to describe the HM behaviour are given in Table 5-1 below.

Table 5-1. Material parameters used in the modelling of the consolidation test.

Parameter		Units	Value/Expression
Hydraulic permeability	k	m^2	$1.2 \times 10^{-20}\ e^{5.33}$
Initial void ratio	e_0	-	0.906
Path variable derivative	K	-	40[1)]
Lower swelling pressure curve	c_0^{low}	-	1.259
	c_1^{low}	m^3/kg	4.117×10^{-3}
	c_2^{low}	m^6/kg^2	-3.94×10^{-7}
Upper swelling pressure curve	c_0^{high}	-	3.325
	c_1^{high}	m^3/kg	2.101×10^{-3}
	c_2^{high}	m^6/kg^2	1.669×10^{-7}

[1)] See Börgesson et al. (2019).

The results can be visualised by plotting the evolution in void ratio versus axial clay potential, as is shown in Figure 5-4. The results of the COMSOL model agrees very well with experimental results.

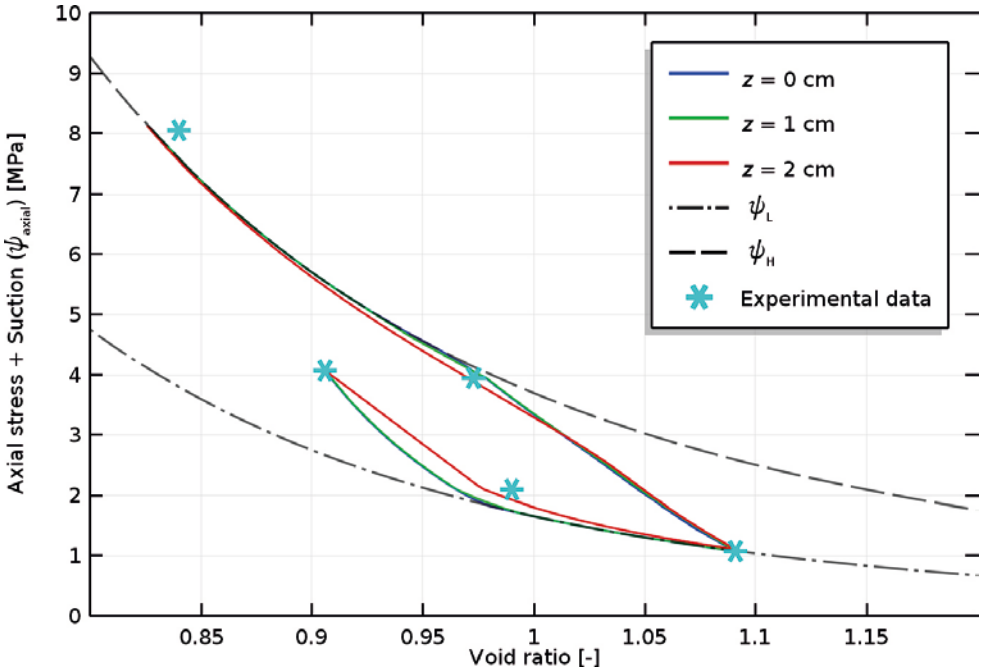

Figure 5-4. *Evolution in void ratio versus Clay potential in the axial direction (i.e. axial stress + suction).*

5.4 Modelling of EBS TF homogenisation tasks

So far, one homogenisation experiment from the EBS TF (axial swelling, HR-A1) has been modelled using COMSOL Multiphysics and the HBM model. The experiment was described in Section 4.2.2. The setup and results are described below.

5.4.1 Model setup

The geometry (see left panel of Figure 5-5) used was a 2D axisymmetric representation of the experimental setup. Since only axial swelling is studied (and wall friction is not included) the radial extent of the experiment could be ignored and hence the model representation was made very thin. Two materials were modelled: the swelling clay component (initial height of 37.4 mm) and a confining "lid" situated at z = 50 mm. The upper boundary of the clay component and the lower boundary of the lid was defined as a contact pair, in order to simulate the contact between the swelling clay and the lid. A linear elastic material model was used for the lid, while the HBM model was used for the clay. The adopted material representation of the buffer is summarised in Table 5-2 and for the lid in Table 5-3. The contact problem between the lid and buffer was handled using a penalty factor (see COMSOL Multiphysics Reference Manual) – the values are shown in Table 5-4.

The boundary conditions prescribed were:

- **H –** No flow on the lower horizontal boundary and outer vertical boundary (and by definition on the symmetry axis). On the upper horizontal boundary of the clay component atmospheric pressure was prescribed (see middle panel of Figure 5-5).
- **M –** Roller boundaries were prescribed on the lower horizontal and outer vertical boundary of the buffer component, as well as on the upper horizontal and outer vertical boundary of the lid. On the upper horizontal boundary of the clay component a boundary stress of 10 kPa was prescribed until the gap was closed, while on the lower horizontal boundary of the lid roller conditions were prescribed during the same time.

Table 5-2. Material parameters of buffer (HBM model).

Parameter		Units	Value/Expression
Hydraulic permeability	k	m^2	$1.2 \times 10^{-20}\ e^{5.33}$
Density of water	ρ_w	kg/m^3	$998 \times e^{-\alpha_w s}$
	α_w	1/Pa	4.5×10^{-10}
Initial void ratio	e_0	-	0.700
Path variable derivative	K	-	40[1)]
Lower swelling pressure curve	c_0^{low}	-	1.259
	c_1^{low}	m^3/kg	4.117×10^{-3}
	c_2^{low}	m^6/kg^2	-3.94×10^{-7}
Upper swelling pressure curve	c_0^{high}	-	3.325
	c_1^{high}	m^3/kg	2.101×10^{-3}
	c_2^{high}	m^6/kg^2	1.669×10^{-7}

[1)] See Börgesson et al. (2019).

Table 5-3. Material parameters of the lid (linear elastic material model).

Parameter		Units	Value/Expression
Young modulus	E	MPa	100
Poisson's ratio	v	-	0.2

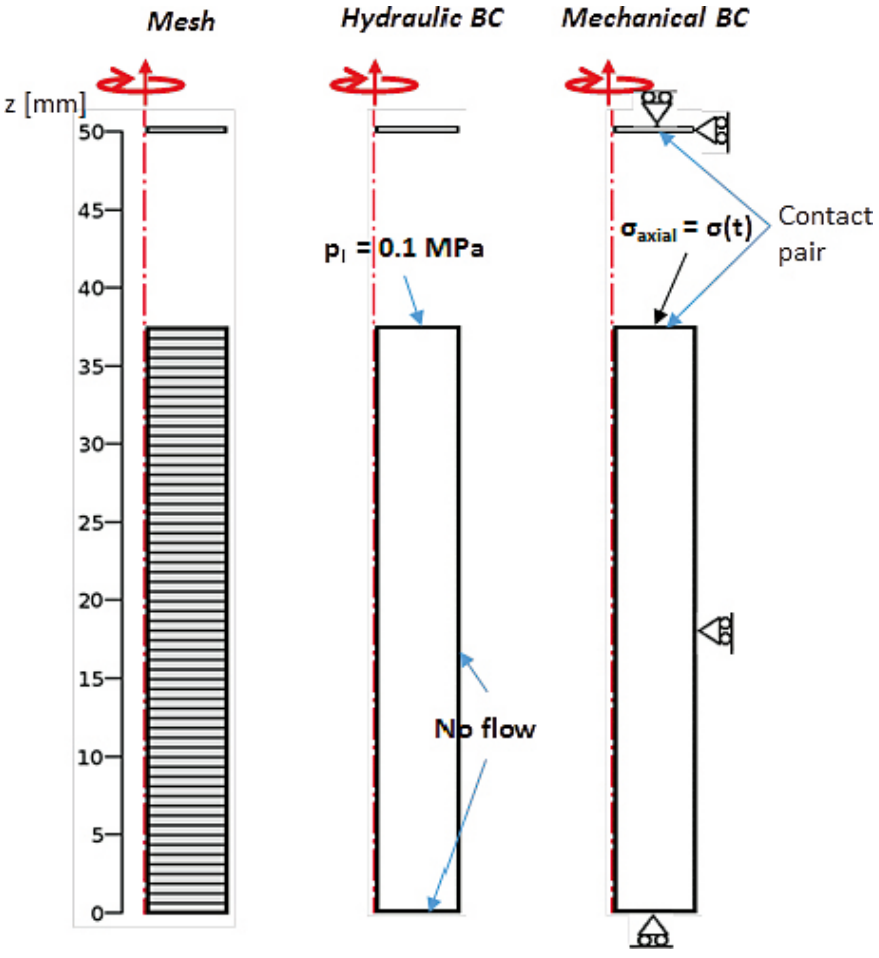

Figure 5-5. *Boundary conditions used in the model of the HR-A1 homogenisation experiment.*

Table 5-4. Material parameters of the contact pair.

Units	Value/Expression	
Contact pressure penalty mode	-	*Penalty factor*
Contact pressure penalty factor	Pa/m	10^7
Contact pressure at zero gap	Pa	0

5.4.2 Results

The results of the model are shown both in terms of the time evolution and the final state. The evolution of stress is show in Figure 5-6. The solid lines show the COMSOL solution, while the dotted lines shows the time-evolution in the actual experiment. The dashed lines show the results from a numerical solution for simple 1D-geometries, developed in the advanced spreadsheet software MathCad, presented by Börgesson et al. (2019). As can be seen, the COMSOL model agrees well with both the Mathcad solution and experimental data.

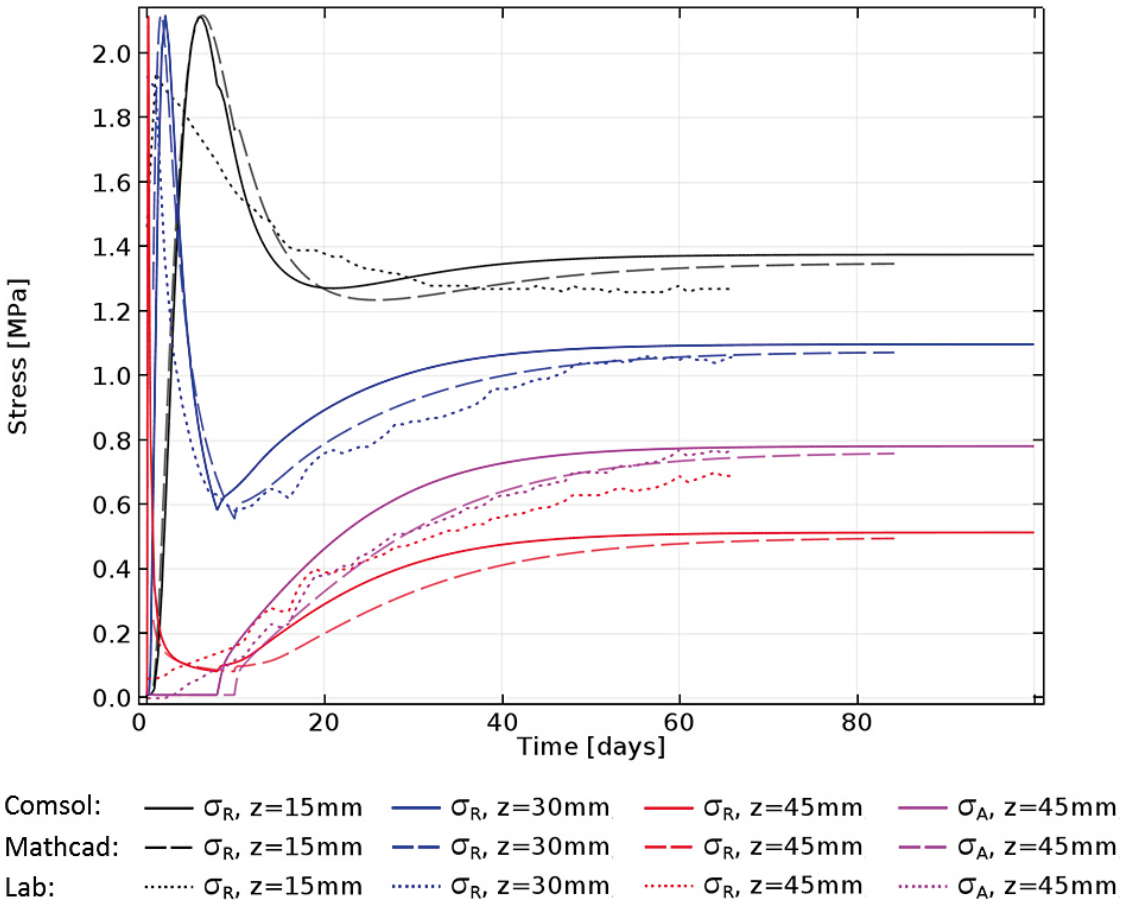

Figure 5-6. *Stress evolution in the COMSOL and Mathcad model.*

The HBM model postulates that during swelling the path in the void ratio vs clay potential plane should follow the lower clay potential curve asymptotically (identified by the grey dash-dotted line in Figure 5-7) while during compression the path should move towards the upper clay potential curve (grey dashed line in Figure 5-7). In the model the upper parts of the clay swell until the top reaches the lid of the container. Thereafter the top parts undergo compression due to swelling of the clay further down.

This behaviour can be clearly seen in Figure 5-7 where the evolution in several points in the buffer component is shown (coloured solid lines). In the upper part of the buffer (blue, green and red solid lines) the axial clay potential as function of void ratio moves towards the lower clay potential curve during the swelling phase, and during the following compression (due to swelling in the lower parts) it moves towards the upper clay potential curve. Further down in the buffer (cyan and purple solid lines) only swelling occurs. In the final state all points have the same axial clay potential (due to zero suction in all points) and hence lie on a straight vertical line in the axial clay potential – void ratio diagram.

In Figure 5-8 the final dry-density state is shown, where the red solid line identifies the COMSOL solution. The blue line represents a numerical solution performed in Mathcad using the same material model. Finally, the black stars identify the experimental results.

As can be seen the COMSOL model agrees relatively well with the Mathcad solution, while these two in turn differs somewhat from the experimental data. The latter may be due to a range of factors, such as the liquid inflow, friction against the container wall and material parameterisation – so far these factors have not been investigated.

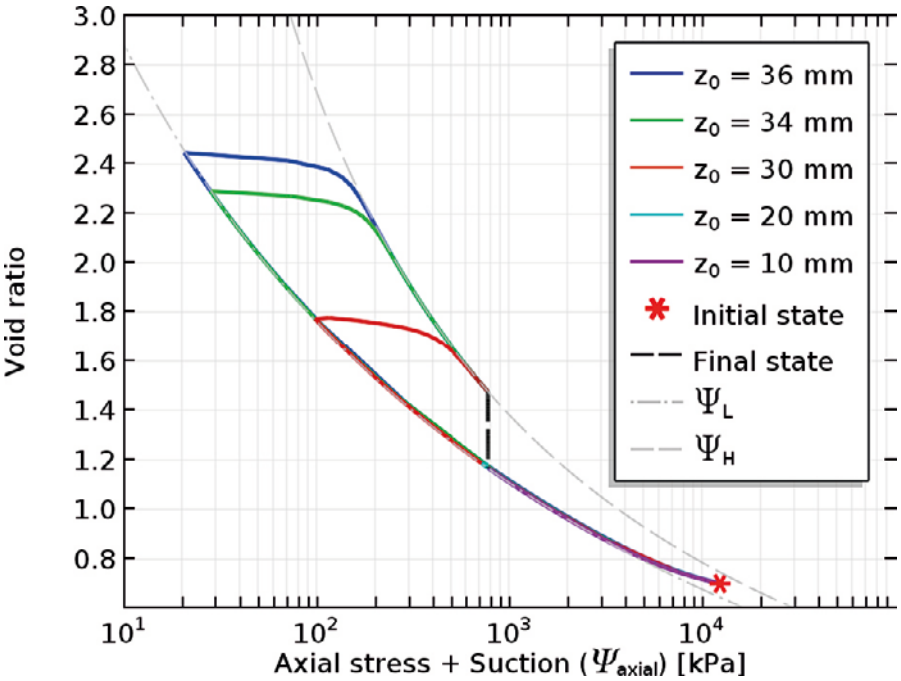

Figure 5-7. *Clay potential (axial direction) versus void ratio evolution in the model of the HR-A1 axial swelling experiment. The coloured solid lines illustrates the evolution at different heights in the model, while the black dashed line shows the final state.*

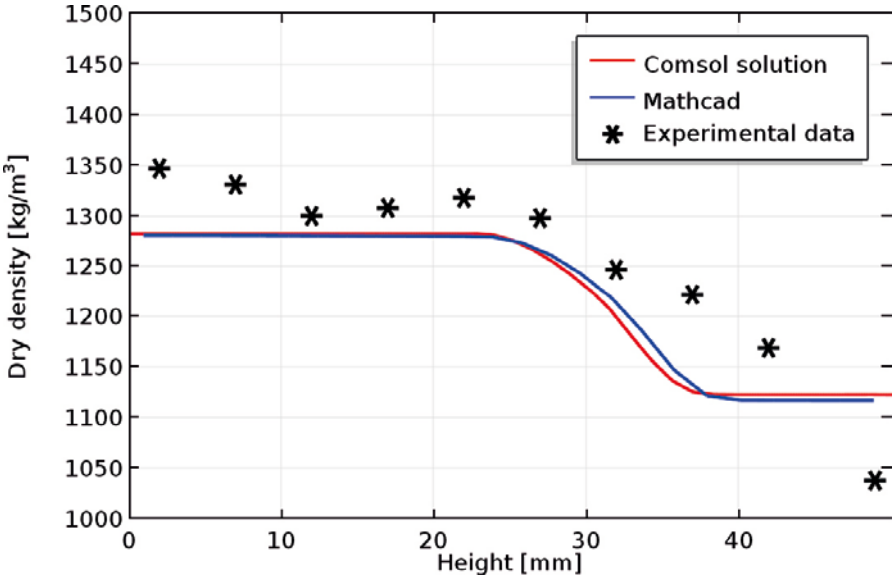

Figure 5-8. *Final state of the COMSOL model (red line), analytical MathCad solution (blue line) and experimental data (black stars).*

5.5 Comparison between Abaqus and COMSOL

In order to visualize differences obtained when using the Abaqus or COMSOL material model implementations, Figure 5-9 and Figure 5-10 show final state dry density profiles and evolutions in void ratio – axial clay potential (or effective stress), respectively.

In Figure 5-9 the Abaqus (solid black line) and Comsol (red line) final state dry density profiles may be compared with each other as well as with the experimental data (symbols). It should be remembered that as shown in Chapter 4.2.4, the Abaqus solution at the centre is not significantly affected by using friction. The response from the frictionless model in Comsol should therefore be compared with the response obtained at the centre position in the Abaqus model.

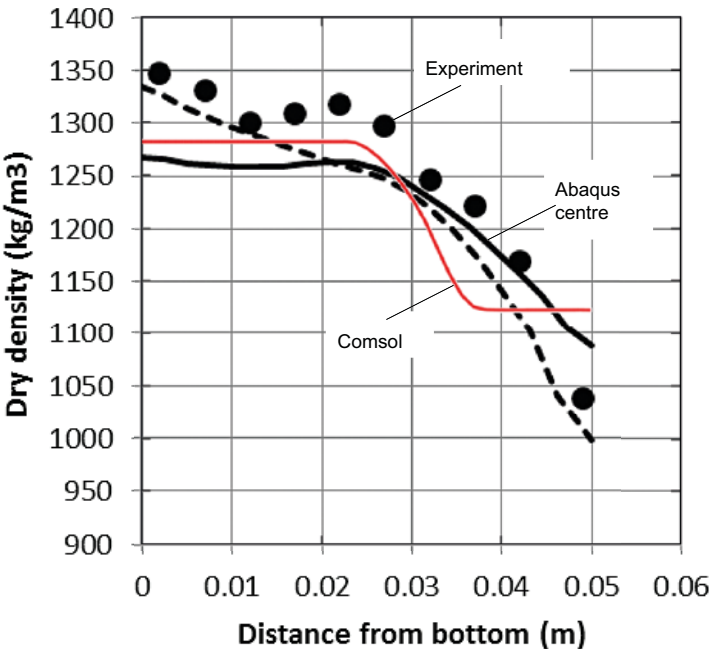

Figure 5-9. *Dry density profiles at the final state of the HR-A1 axial swelling experiment. Experimental (black symbols), Abaqus centre (solid black line), Abaqus outer (dotted black line) and COMSOL data (red line) are shown together.*

The most significant difference between the profiles is the horizontal/constant plateaus vs varying profile, for the Comsol and Abaqus responses, respectively. When compared to experimental data a varying profile seems most appropriate. It is expected that by incorporating friction between the clay and container in the Comsol model, a dry density profile with less horizontal appearance will develop as well. However, the results from the Abaqus model showed that the inclusion of friction did not influence the density profile along the center line (see Figure 4-7).

In Figure 5-10 evolutions of void ratio – axial clay potential are shown for different initial heights in the Abaqus (hatched lines) and Comsol model (solid lines). This enables a comparison of how the mechanical process evolves for the two models. The lower (swelling) and higher (consolidation) bound curves in the Comsol model (grey hatched lines), evaluated from experimental findings, are also indicated.

During the initial phase of swelling both model evolutions approximately follow each other and the lower bound curve. At higher levels of swelling the Abaqus model evolutions start to deviate from the lower bound curve and ends up below this. This is most evident for z_0 = 35 mm. This is an indication that a limit in the Abaqus model has been reached. It is intended for use for void ratios from 0.7 to 1.5.

The evolution paths for the two models have different appearances when going into consolidation. The Comsol model generates scan-lines, when leaving the lower bound curve, with lower initial derivative as compared to the Abaqus model. As the Comsol scan-line approaches the upper bound curve, see the response for z_0 = 35 mm, the derivative increases gradually towards that of the upper bound curve which makes the response follow this curve. This is not so for Abaqus which shows no tendency to follow the upper bound curve when approaching this, see the response for z_0 = 35 mm.

As already mentioned above and shown in Figure 5-9, the final state of the models differs. Both models end up at states with constant clay potential (axial stress), i.e. a vertical line in Figure 5-10. For Comsol, the same, or very similar, void ratios might be obtained at different positions in the model if the states coincide with the upper or lower bound curves. Thus, we may end up with the plateaus in dry density observed in Figure 5-9. The Abaqus model on the other hand does not have this internal mechanism ending up at an upper or lower bound curve, and the final dry density profile is therefore less prone to form plateaus.

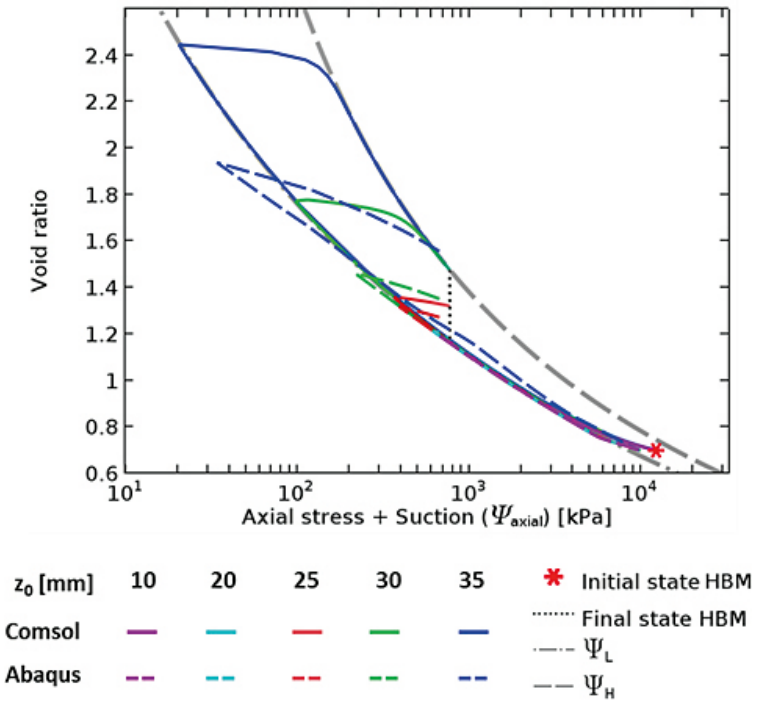

Figure 5-10. *Comparison of COMSOL (HBM) and Abaqus model responses for different initial distances from the bottom. Clay potential (axial direction) versus void ratio evolution in the model of the HR-A1 axial swelling experiment. The coloured lines illustrates the evolution at different initial heights in the model, solid and dashed for the COMSOL and Abaqus responses, respectively.*

6 Conclusions

6.1 General

Gaps, holes or inhomogeneous density distributions may be present in the buffer or backfill material due to loss of bentonite material by piping and erosion during the installation and saturation phases or by colloid erosion during glacial groundwater conditions. Heterogeneous initial conditions prevail due to the installation technique with blocks with gaps between them, gaps filled with pellets, and mechanical interaction between e.g. the buffer and the backfill. How well the bentonite self-seals and homogenises have been studied in this project. The laboratory tests have mainly been made on specimens that have been water saturated or close to water saturated from the start, which means that the saturation process has not been included in the tests.

The purposes of the homogenisation project and the tests have been to:

- Understand how homogenisation evolves and ends.
- Investigate the different factors influencing homogenisation.
- Understand how much inhomogeneity remains within the bentonite.
- Be a base for creating hydro-mechanical models for the homogenisation process.
- Evaluate models, model parameters and modelling tools.

The objective with this report has been to compile the findings from this study which include to 1) point out the most important test results from the fundamental laboratory tests, 2) analyse the laboratory test results with different material models and calculation tools, 3) determine mechanical parameters for modelling the homogenisation behaviour of bentonite buffer material and 4) develop a new hydro-mechanical bentonite material model.

6.2 Laboratory tests

The following observations were made on the fundamental laboratory test results shown in Chapter 3.

Swelling pressure – dry density relation (Section 3.3.1)

After swelling, mainly between 0 and 50 %, and subsequent homogenisation the test results of MX-80 show:

- That the average stress together with the average density represented the conditions of the buffer well in the sense that they agreed with the expected relations from constant volume swelling pressure tests.
- That the swelling pressure together with the dry density at the corresponding position agreed well with the model presented by Börgesson et al. (1995) except at positions where the largest swelling took place where higher swelling pressure than expected was seen.

The corresponding test results of Calcigel show:

- That if plotted with the average dry density the average stress was in the same range as that of MX-80 at high dry density but less at lower dry density.

Gradients in dry density after swelling (Section 3.3.2)

The results from the laboratory tests on MX-80 specimens, of two different sizes which swelled in different directions and homogenised during 11–172 days, show:

- That time influences the density gradient but still after long time and with negligible small changes in the measured stresses density gradients were observed.

- An indication of a linear trend between the normalized dry density gradient and the swelling, however with a relatively large scatter.
- That the results from similar tests on Calcigel seem to follow the same trend, however based on less number of specimens.

Influence of water pressure (Section 3.3.3)

From the laboratory tests where a water pressure was applied in the final part of the tests the following were seen:

- Compared to the swelling pressure measured before the applied water pressure no change or a small increase was seen in the measured stress after removal of the water pressure.
- The response in measured stress to an adjustment of the water pressure was mainly less than the adjustment.
- No clear effect of water pressure on the density gradient of the specimens was seen.

Friction (Section 3.3.4)

From the laboratory tests where a saturated bentonite specimen was forced through a confining ring having a specially prepared inner surface the results show:

- That friction between bentonite and a surface with grooves, evaluated as a friction angle at peak stress, corresponded well to the model of the bentonite internal friction angle presented by Åkesson et al. (2010b) and that the corresponding friction angle when other surfaces were used yielded lower values.
- That the measured maximum shear stress as a function of dry density followed the relationship represented by half the maximum deviatoric stress from the model presented by Börgesson et al. (1995) and that the residual values were lower.

Accuracy, uncertainties and limitations (Section 3.3.5)

The limitations of the test results are related to:

- The measurement of radial swelling pressure which was done by use of small pistons.
- Difficulties to take representative samples for the determination of base variables in specimens with large density gradients over small distances.
- What extent the test conditions and the equilibrium state are good enough to give unique results which can be generalized.

6.3 Analyses from modelling with the FE-program Abaqus and with simplified analytical solutions

The FE-program Abaqus has been used to model three very different types of homogenisation tests.

The HR (high resolution) tests have been modelled with two different mechanical material models. The models have the same porous elastic model for simulating the non-linear isotropic swelling and compression of bentonite, but they have different plastic models for simulating the effect of deviatoric stresses. The Drucker-Prager model is a classic material model included in the model library of Abaqus. The other model (Claytech Plastic Cap model) has been implemented in Abaqus.

The HR-test with only axial swelling was used to check and calibrate the parameters of the models. Then the HR-test with only radial swelling was modelled with the calibrated parameters. Both tests were very well modelled with the cap model but less good with the Drucker-Prager model.

The conclusion of these exercises and additional tests that were modelled, was that the Plastic Cap model simulates bentonite swelling well within a limited density interval but also that the model probably does not work well for the unlikely case of completely isotropic swelling. In addition closing of cylindrical and spherical holes are not well modelled due to numerical problems with strongly deformed elements.

The Cap Model was then used to model (true prediction) the Self-healing Test SH1, which included swelling and homogenisation of a large bentonite block with two cavities. The modelling worked well but the Plastic Cap model underestimated the self-healing ability (or the homogenisation) of the bentonite in the test by yielding too high void ratio (20 %) and too low stresses (40 %) in the former cavity. The Drucker-Prager plastic model captured the void ratio distribution better (although still a little too high) but also this model yielded the same too low stresses in the cavity.

Ten almost identical tests of the homogenisation of two bentonites with large density differences placed in long tubes with raw surfaces have been running for 4–5 years with the purpose to study the long term homogenisation process. Predictive modelling of these tests were performed with the Plastic Cap model. The results have been compared with measured stresses and measured density distribution for the one test that has been terminated and sampled. The results showed that the homogenisation process was well captured with remaining unaffected initial densities at both ends of the tube. However, the length of the transition zone with a density gradient between the unaffected parts was underestimated. This length is strongly dependant on the assumed friction angle between the bentonite and the tube surface and the interpretation is that a too high friction angle ($\phi = 9.0^{o}$) was used in the modelling. Another reason is that the initial densities of the bentonites used in the prediction differed from the actual ones.

The long tube test was also modelled with a simplified analytical model that studies the equilibrium after completed homogenisation. Back-calculating the friction angle from this model yielded the value $\phi = 7.2^{o}$, which gave very good agreement between modelled and measured density distribution. This value also agrees with the average residual friction angle received from friction tests that measure the shear resistance between bentonite and the same type of raw surface, where raw surface is defined as a surface with so large irregularities that the slip takes place in the bentonite.

The final and very important conclusion from these tests is thus that it is the residual friction angle and not the peak value that is valid between a bentonite and a surface even when the surface is so raw that the slip takes place in the bentonite itself.

6.4 Material model development – COMSOL

The new bentonite material model was successfully implemented in COMSOL Multiphysics using the External Material function and was used to simulate fully coupled hydro-mechanical problems. In order to evaluate the model implementation (and the material model itself) two laboratory experiments were simulated:

1. A consolidation test carried out as part of the System Dome Plug design project (Börgesson et al. 2015).
2. The HR-A1 experiment (described in Section 4.2.2).

Both experiments were modelled successfully, and the simulation results agreed well with laboratory data.

It should be remembered that the new material model is in its initial state of development and much work remains to make it more general and the implementation more efficient. It is therefore not very meaningful trying to identify remaining uncertainties at this stage.

6.5 Final comments

The purpose of the project as described in Section 6.1 has to a large extent been fulfilled. The results from the fundamental laboratory tests, the more advanced laboratory tests, the modelling, the model development and the evaluation of all results have yielded an increase in our knowledge on homogenisation processes of bentonite materials and how to model them. The ongoing laboratory tests and model development will additionally increase the knowledge and the skill to predict and understand different homogenisation scenarios. Especially the modelling in COMSOL has to be further developed and evaluated.

7 References

SKB's (Svensk Kärnbränslehantering AB) publications can be found at www.skb.com/publications.

Alonso E E, Gens A, Josa A, 1990. Constitutive model for partially saturated soils. Géotechnique 40, 405–430.

Alonso E E, Vaunat J, Gens A, 1999. Modelling the mechanical behaviour of expansive clays. Engineering Geology 54, 173–183.

Birgersson M, Karnland O, Nilsson U, 2010. Freezing of bentonite. Experimental studies and theoretical considerations. SKB TR-10-40, Svensk Kärnbränslehantering AB.

Birgersson M, Karnland O, 2015. Flow and pressure response in compacted bentonite due to external fluid pressure. SKB TR-14-28, Svensk Kärnbränslehantering AB.

Börgesson L, Johannesson L-E, Sandén T, Hernelind J, 1995. Modelling of the physical behaviour of water saturated clay barriers. Laboratory tests, material models and finite element application. SKB TR-95-20, Svensk Kärnbränslehantering AB.

Börgesson L, Dueck A, Johannesson L-E, 2010. Material model for shear of the buffer – evaluation of laboratory test results. SKB TR-10-31, Svensk Kärnbränslehantering.

Börgesson L, Sandén T, Andersson L, Johannesson L-E, Goudarzi R, Åkesson M, 2015. System design of Dome Plug. Preparatory modelling and tests of the sealing and draining components. SKB R-14-25, Svensk Kärnbränslehantering AB.

Börgesson L, Hernelind J, Åkesson M, 2019. EBS TF – THM modelling. Homogenisation task. SKB P-18-05, Svensk Kärnbränslehantering AB.

Croney D, Coleman J D, Black W P M, 1958. Movement and distribution of water in soil in relation to highway design and performance. Highway Research Board Special Report 40, 226–252.

Dueck A, 2004. Hydro-mechanical properties of a water unsaturated sodium bentonite: laboratory study and theoretical interpretation. PhD thesis. Lund University.

Dueck A, Goudarzi R, Börgesson L, 2011. Buffer homogenisation, status report. SKB TR-12-02, Svensk Kärnbränslehantering AB.

Dueck A, Goudarzi R, Börgesson L, 2014. Buffer homogenisation, status report 2. SKB TR-14-25, Svensk Kärnbränslehantering AB.

Dueck A, Goudarzi R, Börgesson L, 2016. Buffer homogenisation, status report 3. SKB TR-16-04, Svensk Kärnbränslehantering AB.

Dueck A, Goudarzi R, Börgesson L, 2018. Buffer homogenisation – status report 4. SKB TR-17-04, Svensk Kärnbränslehantering AB.

Kahr G, Kraenbuehl F, Stoekli H F, Müller-Vonmoos M, 1990. Study of the water-bentonite system by vapour adsorption, immersion calorimetry and X-ray techniques: II. Heats of immersion, swelling pressures and thermodynamic properties. Clay Minerals 25, 499–506.

Karnland O, Olsson S, Nilsson U, 2006. Mineralogy and sealing properties of various bentonites and smectite-rich clay materials. SKB TR-06-30, Svensk Kärnbränslehantering AB.

Karnland O, Nilsson U, Weber H, Wersin P, 2008. Sealing ability of Wyoming bentonite pellets foreseen as buffer material – Laboratory results. Physics and Chemistry of the Earth, Parts A/B/C 33, S472–S475.

Kassif G, Ben Shalom A, 1971. Experimental relationship between swell pressure and suction. Géotechnique 21, 245–255.

Kristensson O, 2011. Report on the modeling with initially available data. PEBS Deliverable (D3.3-2). Available at: https://www.pebs-eu.de/PEBS/EN/Downloads/downloads_node_en.html;jsessionid=C62688D9CAC30FF2C0FBB0702B7B12CD.1_cid284

Kristensson O, 2013. Extrapolation of the models developed to the repository long-term evolution and evaluation of uncertainties – Review of thermomechanical continuum mixture theories applicable for EBS materials. PEBS Deliverable (D3.5-4a). Available at: https://www.pebs-eu.de/PEBS/EN/Downloads/downloads_node_en.html;jsessionid=C62688D9CAC30FF2C0FBB0702B7B12CD.1_cid284

Low P F, Anderson D M, 1958. Osmotic pressure equations for determining thermodynamic properties of soil water. Soil Science 86, 251–253.

Svensson D, Dueck A, Nilsson U, Olsson S, Sandén T, Lydmark S, Jägerwall S, Pedersen K, Hansen S, 2011. Alternative buffer material. Status of the ongoing laboratory investigation of reference materials and test package 1. SKB TR-11-06, Svensk Kärnbränslehantering AB.

Åkesson M, Kristensson O, Börgesson L, Dueck A, Hernelind J, 2010a. THM modelling of buffer, backfill and other system components. Critical processes and scenarios. SKB TR-10-11, Svensk Kärnbränslehantering AB.

Åkesson M, Börgesson L, Kristensson O, 2010b. SR-site Data report, THM modelling of buffer, backfill and other system components. SKB TR-10-44, Svensk Kärnbränslehantering AB.

Appendix 1

Compilation of laboratory tests

The following tables show all tests presented in the project, i.e. mainly from the reports TR-14-25, TR-16-04 and TR-17-04 (Dueck et al. 2014, 2016, 2018). In addition, some specimens from the first report TR-02-12 are also mentioned.

The materials used, i.e. MX-80 or Calcigel, are mentioned in the tables below and for the tests presented in this report and in TR-16-04 the year of the delivery is also given; MX-80#2010[b], MX-80#2012, Calcigel#2006 or Calcigel#2014. The material MX-80#2012[b] was delivered before 2010.

Table A1-1. Tests made in the series A0.

Specimen ID	Material	Report
A01-09, A01-10	MX-80	TR-12-02
A01-12, A01-13	MX-80	TR-14-25
A01-14, A01-15, A01-16	MX-80#2010[b]	TR-16-04
A04-1, A04-2	Calcigel#2006	TR-16-04

Table A1-2. Tests made in the series R1.

Specimen ID	Material	Report
R11-10, R11-11	MX-80	TR-12-02
R11-17, R11-18, R11-19, R11-20, R11-21	MX-80	TR-14-25
R11-22, R11-23	MX-80#2010[b]	TR-16-04
R11-24	MX-80#2012	TR-16-04
R14-1, R14-2	Calcigel#2006	TR-16-04

Table A1-3. Tests made in the series R2.

Specimen ID	Material	Report
R21-09, R21-10, R21-11, R21-12	MX-80	TR-14-25
R21-13, R21-14	MX-80#2010[b]	TR-16-04
R24-1, R24-2	Calcigel#2006	TR-16-04

Table A1-4. All tests made in the series HR-A, HR-Ro, HR-Ri and HR-Iso.

Specimen ID	Material	Report
HR-A1	MX-80	TR-14-25
HR-A2, HR-A3, HR-A4	MX-80#2010[b]	TR-16-04
HR-A6	Calcigel#2006	TR-16-04
HR-A7	Calcigel#2006	TR-17-04
HR-A8	Calcigel#2014	TR-17-04
HR-Ro1	MX-80	TR-14-25
HR-Ro2	Calcigel#2006	TR-16-04
HR-Ro3	Calcigel#2014	TR-17-04
HR-Ri1	MX-80#2010[b]	TR-16-04
HR-Ri2	Calcigel#2014	TR-17-04
HR-Iso	MX-80#2010[b]	TR-16-04

Table A1-5. All tests made in the series Fr.

Specimen ID	Material	Report
Fr1-1 to Fr1-5, Fr1-7 to Fr1-9	MX-80	TR-14-25
Fr1-10, Fr1-12, Fr1-13	MX-80#2010[b]	TR-16-04
Fr1-11, Fr1-14	MX-80 pellet	TR-16-04
Fr1-15 to Fr1-17, Fr-19, Fr1-20	MX-80#2012	TR-16-04
Fr2-1	Calcigel#2006	TR-16-04
Fr2-2	Calcigel#2006	TR-17-04

Table A1-6. All tests made in the series W.

Specimen ID	Material	Report
W1-2, W1-3, W1-4	Calcigel#2006	TR-17-04

Table A1-7. Two tests in the series SH.

Specimen ID	Material	Report
SH1	MX-80#2012	TR-16-04 and TR-17-04
SH2	MX-80#2012	TR-16-04

Table A1-8. All tests in the series FLR.

Specimen ID	Material lower part	Material upper part	Report
FLR1-4 on going	MX-80#2012	MX-80 pellet#2011	TR-17-04
FLR5	MX-80#2012	MX-80 pellet#2011	TR-17-04
FLR6 to FRL10 on going	MX-80#2012	MX-80 pellet#2011	TR-17-04

Appendix 2

Model development – Theoretical framework

In order to set the stage properly before the description of the material model in Chapter 5.1, the theoretical framework in which this is to be included is first described. First the nomenclature and basic entities are described in A2.1 which is followed in A2.2 by the assumptions made of the material structure. Finally in A2.3 the fundamental balance equations, in which the constitutive laws are to be inserted, are described.

A2.1 Preliminaries

Index free notation is used to the major part, but sometimes index notation is used. A Cartesian coordinate frame, consisting of a reference point (the origin) and a positive orthonormal basis $\{\boldsymbol{e}_1, \boldsymbol{e}_2, \boldsymbol{e}_3\}$, is used. Using this a vector $\boldsymbol{v}$ can be expressed,

$$\boldsymbol{v} = v_1\boldsymbol{e}_1 + v_2\boldsymbol{e}_2 + v_2\boldsymbol{e}_2 = v_i\boldsymbol{e}_i \tag{A2-1}$$

and a second order tensor T can be expressed as,

$$\boldsymbol{T} = \begin{matrix} T_{11}\boldsymbol{e}_1 \otimes \boldsymbol{e}_1 + T_{12}\boldsymbol{e}_1 \otimes \boldsymbol{e}_2 + T_{13}\boldsymbol{e}_1 \otimes \boldsymbol{e}_3 + \\ T_{21}\boldsymbol{e}_2 \otimes \boldsymbol{e}_1 + T_{22}\boldsymbol{e}_2 \otimes \boldsymbol{e}_2 + T_{23}\boldsymbol{e}_2 \otimes \boldsymbol{e}_3 + = T_{ij}\boldsymbol{e}_i \otimes \boldsymbol{e}_j \\ T_{31}\boldsymbol{e}_3 \otimes \boldsymbol{e}_1 + T_{32}\boldsymbol{e}_3 \otimes \boldsymbol{e}_2 + T_{33}\boldsymbol{e}_3 \otimes \boldsymbol{e}_3 \end{matrix} \tag{A2-2}$$

where $\otimes$ denote the tensor product between vectors so that $\boldsymbol{e}_i \otimes \boldsymbol{e}_j$ is a second order tensor. As can be seen in the right-hand sides above, summation convention is used to compress the index notation. The second order unit tensor $\mathbf{1}$ is defined by $\mathbf{1}\boldsymbol{v} = \boldsymbol{v}$, and the following is used when using index notation,

$$\mathbf{1} = \delta_{ij}\boldsymbol{e}_i \otimes \boldsymbol{e}_j \,, \delta_{ij} = \begin{cases} 1 \text{ if } i = j \\ 0 \text{ if } i \neq j \end{cases} \tag{A2-3}$$

Position vectors $\boldsymbol{X}$ of material points in a body in the reference configuration together with a function $\boldsymbol{\chi}$ describing the motion of the points give position vectors $\boldsymbol{x} = \boldsymbol{\chi}(\boldsymbol{X}, t)$, in the deformed configuration. For a fixed time the inverse mapping $\boldsymbol{X} = \boldsymbol{\chi}^{-1}(\boldsymbol{x}, t)$ exists. Displacements are defined by $\boldsymbol{u} = \boldsymbol{x} - \boldsymbol{X}$.

Taking the partial time derivative of the motion gives the velocity,

$$\dot{\boldsymbol{\chi}}(\boldsymbol{X}, t) = \frac{\partial \boldsymbol{\chi}(\boldsymbol{X}, t)}{\partial t} \tag{A2-4}$$

which, by using the inverse map, also can be given by,

$$\boldsymbol{v}(\boldsymbol{x}, t) = \dot{\boldsymbol{\chi}}(\boldsymbol{\chi}^{-1}(\boldsymbol{x}, t), t) \tag{A2-5}$$

In line with the above, fields may be defined over the body in both configurations, thus a field φ may be given as $\varphi(\boldsymbol{X}, t)$ or $\varphi(\boldsymbol{x}, t)$, being the material description and spatial description, respectively.

The material time derivative $\dot{\varphi}$ and spatial time derivative φ' of the φ-field are defined by:

$$\dot{\varphi}(\boldsymbol{X}, t) = \frac{\partial \varphi(\boldsymbol{X}, t)}{\partial t} \text{ (holding } \boldsymbol{X} \text{ fixed)} \tag{A2-6}$$

and

$$\varphi'(\boldsymbol{x}, t) = \frac{\partial \varphi(\boldsymbol{x}, t)}{\partial t} \text{ (holding } \boldsymbol{x} \text{ fixed)} \tag{A2-7}$$

respectively. When φ is a spatial field (given in terms of $\boldsymbol{x}$) its material time derivative is given by,

$$\dot{\varphi}(\boldsymbol{x}, t) = \varphi'(\boldsymbol{x}, t) + \frac{\partial \varphi(\boldsymbol{x}, t)}{\partial \boldsymbol{x}} \cdot \boldsymbol{v}(\boldsymbol{x}, t) \tag{A2-8}$$

The deformation gradient,

$$\boldsymbol{F} = \frac{\partial \boldsymbol{x}}{\partial \boldsymbol{X}} = \frac{\partial (\boldsymbol{X} + \boldsymbol{u})}{\partial \boldsymbol{X}} = \mathbf{1} + \frac{\partial \boldsymbol{u}}{\partial \boldsymbol{X}} \tag{A2-9}$$

is a kinematical entity linking an infinitesimal material fibre in the reference (undeformed) configuration, $d\boldsymbol{X}$ to an infinitesimal material fibre in the deformed configuration, $d\boldsymbol{x} = d\boldsymbol{X} + d\boldsymbol{u}$.

In this paragraph a definition of the small strain tensor ε and the underlying approximation made is given. The Lagrangean (large) strain tensor,

$$\boldsymbol{E} = \frac{1}{2}(\boldsymbol{F}^T\boldsymbol{F} - \boldsymbol{1}) \tag{A2-10}$$

is used as a basis for describing the small strain approximation. Using the relation between the deformation gradient and the displacement gradient makes it possible to write,

$$\boldsymbol{E} = \frac{1}{2}\left(\left(\boldsymbol{1} + \frac{\partial \boldsymbol{u}}{\partial \boldsymbol{X}}\right)^T\left(\boldsymbol{1} + \frac{\partial \boldsymbol{u}}{\partial \boldsymbol{X}}\right) - \boldsymbol{1}\right) = \frac{1}{2}\left(\frac{\partial \boldsymbol{u}}{\partial \boldsymbol{X}} + \left(\frac{\partial \boldsymbol{u}}{\partial \boldsymbol{X}}\right)^T + \left(\frac{\partial \boldsymbol{u}}{\partial \boldsymbol{X}}\right)^T\frac{\partial \boldsymbol{u}}{\partial \boldsymbol{X}}\right) \tag{A2-11}$$

If the displacement gradient is small, i.e. $\frac{\partial \boldsymbol{u}}{\partial \boldsymbol{X}} = \boldsymbol{F} - \boldsymbol{1}$ is small, the last higher order term of the Lagrangean strain tensor becomes insignificant in relation to the first order terms. The Lagrangean strain may then be approximated by the small (infinitesimal) strain:

$$\boldsymbol{E} \approx \boldsymbol{\varepsilon} \equiv \frac{1}{2}\left(\frac{\partial \boldsymbol{u}}{\partial \boldsymbol{X}} + \left(\frac{\partial \boldsymbol{u}}{\partial \boldsymbol{X}}\right)^T\right) \tag{A2-12}$$

Here, the conventional continuum mechanics sign convention is used, e.g. when a material fibre undergoes elongation the strain is positive. The stress is also defined using the same convention, i.e. it is positive for tensile conditions.

The stress and strain tensors can be decomposed in a spherical part and a deviatoric part according to,

$$\boldsymbol{\sigma} = \frac{1}{3}\mathrm{tr}\boldsymbol{\sigma}\,\boldsymbol{1} + \boldsymbol{s} = -p\,\boldsymbol{1} + \boldsymbol{s} \quad \text{and} \quad \boldsymbol{\varepsilon} = \frac{1}{3}\mathrm{tr}\boldsymbol{\varepsilon}\,\boldsymbol{1} + \boldsymbol{e} = \frac{1}{3}\varepsilon_v\,\boldsymbol{1} + \boldsymbol{e} \tag{A2-13}$$

where tr denotes the trace of the tensor, i.e. $\mathrm{tr}\boldsymbol{\sigma} = \boldsymbol{\sigma} \cdot \boldsymbol{1}$.

Pressure, p, (positive in compression) and volumetric strain, ε_v, (positive for an increase in volume) are defined using the spherical part of the tensors according to,

$$p \equiv -\frac{1}{3}\mathrm{tr}\boldsymbol{\sigma} \tag{A2-14}$$

and

$$\varepsilon_v \equiv \mathrm{tr}\boldsymbol{\varepsilon} \tag{A2-15}$$

respectively.

In the following a tilde above an entity indicate that the entity should be considered a function, i.e.

$$\psi = \tilde{\psi}(e, f) \tag{A2-16}$$

should be understood as the variable ψ is given by the function $\tilde{\psi}$ having the inputs variables e and f.

A2.2 Structural representation of the material

The material model is based on an additive division of a material volume element dv into a solid volume element dv_s and a pore volume element dv_p according to,

$$dv = dv_s + dv_p \tag{A2-17}$$

In the present version of the model, where only fully saturated conditions are considered, the pore volume element is equal to the water volume element, i.e. $dv_p = dv_w$. The solid and water volume elements have mass elements dm_s and dm_w, respectively, which makes it possible to introduce corresponding mass densities,

$$\rho_s = \frac{dm_s}{dv_s} \tag{A2-18}$$

and

$$\rho_w = \frac{dm_w}{dv_w} \tag{A2-19}$$

The water content *w*, void ratio *e* and the porosity ϕ are variables present in the formulation; these are defined as:

$$w = \frac{dm_w}{dm_s} \tag{A2-20}$$

$$e = \frac{dv_p}{dv_s} = \frac{dv_w}{dv_s} \tag{A2-21}$$

$$\phi = \frac{dv_p}{dv} = \frac{dv_w}{dv} \tag{A2-22}$$

The current void ratio, *e*, can be estimated by using the approximate expression,

$$e \approx \varepsilon_v(1 + e^0) + e^0 \tag{A2-23}$$

valid when the small strain assumption is used.

A2.3 Fundamental balance equations and constitutive equations

The solid mass per mixture volume can be expressed,

$$\frac{dm_s}{dv} = \frac{dm_s}{dv_s}\frac{dv - dv_p}{dv} = \rho_s(1 - \phi) \tag{A2-24}$$

The Reynold's transport relation[1] gives us the *solid mass balance equation*,

$$\dot{\rho}_s(1 - \phi) - \rho_s\dot{\phi} + \rho_s(1 - \phi)\,\mathrm{div}\dot{\boldsymbol{u}}_s = 0 \tag{A2-25}$$

and if assuming a constant solid density one obtains,

$$\dot{\phi} = (1 - \phi)\,\mathrm{div}\dot{\boldsymbol{u}}_s \tag{A2-26}$$

The water mass per mixture volume can be expressed as,

$$\frac{dm_w}{dv} = \rho_w\frac{dv_w}{dv} = \rho_w\phi \tag{A2-27}$$

Again, the Reynold's transport relation, and introducing a source term, f_w, the *water mass balance equation* reads,

$$\dot{\rho}_w\phi + \rho_w\dot{\phi} + \rho_w\phi\,\mathrm{div}\dot{\boldsymbol{u}}_w = f_w \tag{A2-28}$$

The quasi-static version of *balance of momentum*, i.e. the *balance of forces*, for the porous media reads,

$$\mathrm{div}\boldsymbol{\sigma} + \boldsymbol{b} = \boldsymbol{0} \tag{A2-29}$$

where $\boldsymbol{\sigma}$ denotes the Cauchy stress tensor and $\boldsymbol{b}$ denotes a body force vector.

Altogether, for a constant solid density, the balance equations to be solved are:

$$\dot{\phi} = (1 - \phi)\,\mathrm{div}\dot{\boldsymbol{u}}_s \tag{A2-30}$$

$$\dot{\rho}_w\phi + \rho_w\dot{\phi} + \rho_w\phi\,\mathrm{div}\dot{\boldsymbol{u}}_w = f_w \tag{A2-31}$$

$$\mathrm{div}\boldsymbol{\sigma} + \boldsymbol{b} = \boldsymbol{0} \tag{A2-32}$$

In order to establish a complete formulation and describing the material behaviour for the specific system to simulate, *constitutive equations* have to be formulated. When formulating the constitutive equations, *dependent variables* are given by *independent variables*, for which the then obtained system of equations are solved.

[1] $\frac{\partial}{\partial t}\Big|_{\boldsymbol{X}}\left(\int_{\mathcal{P}} \varphi dv\right) = \int_{\mathcal{P}} (\dot{\varphi} + \varphi\mathrm{div}\dot{\boldsymbol{u}})dv$

In the present formulation the balance equations above are reconfigured somewhat to obtain a suitable set of variables. First it should be noted that, with $\boldsymbol{\varepsilon} = \boldsymbol{\varepsilon}_s$, (i.e. dropping the solid phase index for the strain):

$$\mathrm{div}\dot{\boldsymbol{u}}_s = \frac{\partial}{\partial t}\left(\mathrm{tr}\left(\frac{\partial \boldsymbol{u}_s}{\partial \boldsymbol{x}}\right)\right) = \frac{\partial}{\partial t}(\mathrm{tr}\boldsymbol{\varepsilon}) = \dot{\varepsilon}_v \tag{A2-33}$$

Inserting the first balance equation, describing the porosity evolution, in the second, concerning the water mass, and using the relation $\mathrm{div}\dot{\boldsymbol{u}}_s = \dot{\varepsilon}_v$ the following set of equations are obtained,

$$\dot{\phi} = (1-\phi)\,\dot{\varepsilon}_v \tag{A2-34}$$

$$\dot{\rho}_w\phi + \rho_w\phi\,\mathrm{div}(\dot{\boldsymbol{u}}_w - \dot{\boldsymbol{u}}_s) + \rho_w\dot{\varepsilon}_v = f_w \tag{A2-35}$$

$$\mathrm{div}\boldsymbol{\sigma} + \boldsymbol{b} = \boldsymbol{0} \tag{A2-36}$$

The solid displacements, $\boldsymbol{u}_s$, and suction, s, are chosen as the independent variables, for which the system of equations are solved. The dependent variables can then be chosen as:

$$\dot{\boldsymbol{u}}_w - \dot{\boldsymbol{u}}_s = \tilde{\boldsymbol{q}}(s) \tag{A2-37}$$

$$d\boldsymbol{\sigma} = d\tilde{\boldsymbol{\sigma}}(d\boldsymbol{u}_s, ds, \boldsymbol{f}) \tag{A2-38}$$

$$\rho_w = \tilde{\rho}_w(s) \tag{A2-39}$$

Here the functions, indicated by the tildes above, are containing the constitutive equations describing the specific material behaviour. As indicated in the constitutive relation from which the stress is obtained, the "mechanical" material model, an internal variable, $\boldsymbol{f}$, is introduced. This is responsible for the path dependency (hysteresis representation) in the material model.

Appendix 3

Model development – The COMSOL implementation

Information of how the model described in Chapter 5.1.2 were implemented in COMSOL are here given. For details about the general framework to which the model belongs and definitions of entities see Appendix 2 and for a description of the model see Chapter 5.1.

A3.1 Incremental form of the mechanical material model

For recapitulation, the model can be described by:

$$-\boldsymbol{\sigma} = \boldsymbol{\Psi} - s\mathbf{1} \tag{A3-1}$$

$$\boldsymbol{\Psi} = \widetilde{\Psi}_M(\varepsilon_v)\mathbf{1} + \widetilde{\Psi}_{\Delta/2}(\varepsilon_v)\boldsymbol{f} \tag{A3-2}$$

$$\boldsymbol{f} = \boldsymbol{f}_0 + \int_{t_0}^{t} \frac{\partial \boldsymbol{f}}{\partial \boldsymbol{\varepsilon}} \dot{\boldsymbol{\varepsilon}}\, dt^* \tag{A3-3}$$

which may be reformulated as,

$$\boldsymbol{\sigma} = \widetilde{\boldsymbol{\sigma}}(\boldsymbol{\varepsilon}, \boldsymbol{f}, s) \tag{A3-4}$$

The time derivative can then be written,

$$\dot{\boldsymbol{\sigma}} = \frac{\partial \boldsymbol{\sigma}}{\partial \boldsymbol{\varepsilon}}\dot{\boldsymbol{\varepsilon}} + \frac{\partial \boldsymbol{\sigma}}{\partial \boldsymbol{f}}\dot{\boldsymbol{f}} + \frac{\partial \boldsymbol{\sigma}}{\partial s}\dot{s} \tag{A3-5}$$

where,

$$\frac{\partial \boldsymbol{\sigma}}{\partial \boldsymbol{\varepsilon}} = \frac{\partial \boldsymbol{\sigma}}{\partial \boldsymbol{\psi}}\frac{\partial \boldsymbol{\psi}}{\partial \boldsymbol{\varepsilon}} \quad \text{and} \quad \frac{\partial \boldsymbol{\sigma}}{\partial \boldsymbol{f}} = \frac{\partial \boldsymbol{\sigma}}{\partial \boldsymbol{\psi}}\frac{\partial \boldsymbol{\psi}}{\partial \boldsymbol{f}}.$$

The ingoing derivatives are given by,

$$\frac{\partial \boldsymbol{\sigma}}{\partial \boldsymbol{\psi}} = -\mathbb{I} \tag{A3-6}$$

where $\mathbb{I}$ denotes the fourth order unit tensor,

$$\frac{\partial \boldsymbol{\psi}}{\partial \boldsymbol{\varepsilon}} = \frac{\partial \psi_M}{\partial \varepsilon_v}\mathbf{1} \otimes \mathbf{1} + \frac{\partial \psi_{\Delta/2}}{\partial \varepsilon_v}\boldsymbol{f} \otimes \mathbf{1} \tag{A3-7}$$

$$\frac{\partial \boldsymbol{\psi}}{\partial \boldsymbol{f}} = \psi_{\Delta/2}\mathbb{I} \tag{A3-8}$$

$$\dot{\boldsymbol{f}} = \frac{\partial \boldsymbol{f}}{\partial \boldsymbol{\varepsilon}}\dot{\boldsymbol{\varepsilon}} \tag{A3-9}$$

and

$$\frac{\partial \boldsymbol{\sigma}}{\partial s} = \mathbf{1} \tag{A3-10}$$

Using all the above gives,

$$\dot{\boldsymbol{\sigma}} = \left[-\frac{\partial \psi_M}{\partial \varepsilon_v}\mathbf{1} \otimes \mathbf{1} - \frac{\partial \psi_{\Delta/2}}{\partial \varepsilon_v}\boldsymbol{f} \otimes \mathbf{1} - \psi_{\Delta/2}\frac{\partial \boldsymbol{f}}{\partial \boldsymbol{\varepsilon}}\right]\dot{\boldsymbol{\varepsilon}} + \mathbf{1}\dot{s} = \mathbb{C}\dot{\boldsymbol{\varepsilon}} + \mathbf{1}\dot{s} \tag{A3-11}$$

when expressed on index free notation and

$$\dot{\sigma}_{ij} = \left[-\frac{\partial \psi_M}{\partial \varepsilon_v}\delta_{ij}\delta_{kl} - \frac{\partial \psi_{\Delta/2}}{\partial \varepsilon_v}f_{ij}\delta_{kl} - \psi_{\Delta/2}\left(\frac{\partial \boldsymbol{f}}{\partial \boldsymbol{\varepsilon}}\right)_{ijkl}\right]\dot{\varepsilon}_{kl} + \delta_{ij}\dot{s} = C_{ijkl}\dot{\varepsilon}_{kl} + \delta_{ij}\dot{s} \tag{A3-12}$$

when expressed on index notation. Comparing the mid-expression and right-hand side the stiffness tensor $\mathbb{C}$ (C_{ijkl}) can be identified.

A3.2 Matrix format

In COMSOL second order tensors are represented by column arrays where components are given in Voigt order. It should be noted that in the implementation the ”shear components” of the stiffness matrix, $[\mathbb{C}]$, are given by $C_{1111} \cdot ratio$, where *ratio* is to be specified by the user.

$$[\boldsymbol{\sigma}] = \begin{bmatrix} \sigma_{11} \\ \sigma_{22} \\ \sigma_{33} \\ \sigma_{23} \\ \sigma_{13} \\ \sigma_{12} \end{bmatrix}, \qquad [\boldsymbol{f}] = \begin{bmatrix} f_{11} \\ f_{22} \\ f_{33} \\ 0 \\ 0 \\ 0 \end{bmatrix}, \qquad [\boldsymbol{\varepsilon}] = \begin{bmatrix} \varepsilon_{11} \\ \varepsilon_{22} \\ \varepsilon_{33} \\ \varepsilon_{23} \\ \varepsilon_{13} \\ \varepsilon_{12} \end{bmatrix} \tag{A3-13}$$

$$[\mathbb{C}] = \begin{bmatrix} C_{1111} & \cdots & C_{1112} \\ \vdots & \ddots & \vdots \\ C_{1211} & \cdots & C_{1212} \end{bmatrix} = \begin{bmatrix} [\mathbb{c}] & [0] \\ [0] & [\mathbb{d}] \end{bmatrix} \tag{A3-14}$$

$$[\mathbb{c}] = \begin{bmatrix} -\frac{\partial \psi_M}{\partial \varepsilon_v} - \frac{\partial \psi_{\Delta/2}}{\partial \varepsilon_v} f_{11} - \psi_{\frac{\Delta}{2}} \frac{\partial f_{11}}{\partial \varepsilon_{11}} & -\frac{\partial \psi_M}{\partial \varepsilon_v} - \frac{\partial \psi_{\frac{\Delta}{2}}}{\partial \varepsilon_v} f_{11} & -\frac{\partial \psi_M}{\partial \varepsilon_v} - \frac{\partial \psi_{\frac{\Delta}{2}}}{\partial \varepsilon_v} f_{11} \\ -\frac{\partial \psi_M}{\partial \varepsilon_v} - \frac{\partial \psi_{\frac{\Delta}{2}}}{\partial \varepsilon_v} f_{22} & -\frac{\partial \psi_M}{\partial \varepsilon_v} - \frac{\partial \psi_{\Delta/2}}{\partial \varepsilon_v} f_{22} - \psi_{\frac{\Delta}{2}} \frac{\partial f_{22}}{\partial \varepsilon_{22}} & -\frac{\partial \psi_M}{\partial \varepsilon_v} - \frac{\partial \psi_{\frac{\Delta}{2}}}{\partial \varepsilon_v} f_{22} \\ -\frac{\partial \psi_M}{\partial \varepsilon_v} - \frac{\partial \psi_{\frac{\Delta}{2}}}{\partial \varepsilon_v} f_{33} & -\frac{\partial \psi_M}{\partial \varepsilon_v} - \frac{\partial \psi_{\frac{\Delta}{2}}}{\partial \varepsilon_v} f_{33} & -\frac{\partial \psi_M}{\partial \varepsilon_v} - \frac{\partial \psi_{\frac{\Delta}{2}}}{\partial \varepsilon_v} f_{33} - \psi_{\frac{\Delta}{2}} \frac{\partial f_{33}}{\partial \varepsilon_{33}} \end{bmatrix} \tag{A3-15}$$

$$[\mathbb{d}] = C_{1111} \cdot ratio \begin{bmatrix} 1 & 0 & 0 \\ 0 & 1 & 0 \\ 0 & 0 & 1 \end{bmatrix} \tag{A3-16}$$

A3.3 Approximate state variable evolution law

The sign function,

$$\mathrm{sgn}(x) = \begin{cases} -1 & \text{if} \quad x < 0 \\ 0 & \text{if} \quad x = 0 \\ 1 & \text{if} \quad x > 0 \end{cases} \tag{A3-17}$$

appears in the formulation. Such discontinuous function could be problematic in a numerical solution scheme and therefore availability of ”smoothed” approximate sgn-functions, $\mathrm{sgn}^{\alpha}(x) \approx \mathrm{sgn}\,(x)$, is beneficial for convergence purposes. The following three alternatives show possible ways to accomplish the sought smoothness. The third one has been implemented.

Alternative I: getting sharper as $\varepsilon \to 0$,

$$\mathrm{sgn}^{\alpha}{}_{I}(x) = \frac{x}{\sqrt{x^2 + \varepsilon^2}} \tag{A3-18}$$

Alternative II: where $k \gg 1$

$$\mathrm{sgn}^{\alpha}{}_{II}(x) = \tanh(kx) \tag{A3-19}$$

Alternative III: where δ determines the width of the smooth transition

$$\mathrm{sgn}^{\alpha}{}_{III}(x) = \begin{cases} -1 & \text{if} \quad x < -\frac{\delta}{2} \\ 1 & \text{if} \quad x > \frac{\delta}{2} \\ \sin\left(x \frac{\pi}{\delta}\right) & \text{otherwise} \end{cases} \tag{A3-20}$$

The Heaviside function $\Phi(x)$ is also used in the formulation, it is related to the sgn-function according to:

$$\Phi(x) = \frac{\mathrm{sgn}(x) + 1}{2} \tag{A3-21}$$

and an approximation can therefore be obtained by using the approximate sgn-function,

$$\Phi^{a}{}_{i}(x) = \frac{\mathrm{sgn}^{a}{}_{i}(x) + 1}{2} \tag{A3-22}$$

When describing how the implementation of the state variable (path dependency variable) was accomplished, for convenience, the evolution law is first rearranged according to,

$$-\frac{1}{K}\frac{\partial f_{\alpha\alpha}}{\partial \varepsilon_{\alpha\alpha}} = \tilde{\kappa}(\boldsymbol{f}, \dot{\varepsilon}_{\alpha\alpha}) + \mathrm{sgn}(\dot{\varepsilon}_{\alpha\alpha}) f_{\alpha\alpha} \tag{A3-23}$$

where $\alpha = \{1, 2, 3\}$ and no summation convention should be used. The K-parameter is unitless. Unpacking this equation, and thereby show the formulation on the format used in the code, begins with reviewing the ingoing functions:

$$\tilde{\kappa}(\boldsymbol{f}, \dot{\varepsilon}_{\alpha\alpha}) = 1 - \Phi\big(\tilde{\gamma}(\boldsymbol{f}, \dot{\varepsilon}_{\alpha\alpha})\big)\tilde{\gamma}(\boldsymbol{f}, \dot{\varepsilon}_{\alpha\alpha}) \tag{A3-24}$$

and

$$\tilde{\gamma}(\boldsymbol{f}, \dot{\varepsilon}_{\alpha\alpha}) = \frac{\max(f_{ij}) - \min(f_{ij})}{2} + \mathrm{sgn}(\dot{\varepsilon}_{\alpha\alpha})\frac{\max(f_{ij}) + \min(f_{ij})}{2} \tag{A3-25}$$

In order to establish a transparent and yet slimmed format the entities are evaluated for the different conditions. We have,

$$\tilde{\gamma}(\boldsymbol{f}, \dot{\varepsilon}_{\alpha\alpha}) = \begin{cases} \max(f_{ij}) & \dot{\varepsilon}_{\alpha\alpha} > 0 \\ -\min(f_{ij}) & \dot{\varepsilon}_{\alpha\alpha} < 0 \end{cases} \tag{A3-26}$$

giving

$$\tilde{\kappa}(\boldsymbol{f}, \dot{\varepsilon}_{\alpha\alpha}) = \begin{cases} 1 - \Phi\big(\max(f_{ij})\big)\max(f_{ij}) & \dot{\varepsilon}_{\alpha\alpha} > 0 \\ 1 - \Phi\big(-\min(f_{ij})\big)\big(-\min(f_{ij})\big) & \dot{\varepsilon}_{\alpha\alpha} < 0 \end{cases} \tag{A3-27}$$

which can be rewritten as

$$\tilde{\kappa}(\boldsymbol{f}, \dot{\varepsilon}_{\alpha\alpha}) = \begin{cases} 1 - \max(f_{ij}) & \max(f_{ij}) > 0 \\ 1 & \max(f_{ij}) < 0 \end{cases} \quad \dot{\varepsilon}_{\alpha\alpha} > 0$$
$$\begin{cases} 1 - \big(-\min(f_{ij})\big) & -\min(f_{ij}) > 0 \\ 1 & -\min(f_{ij}) < 0 \end{cases} \quad \dot{\varepsilon}_{\alpha\alpha} < 0 \tag{A3-28}$$

Inserting this into the rearranged the evolution law gives,

$$-\frac{1}{K}\frac{\partial f_{\alpha\alpha}}{\partial \varepsilon_{\alpha\alpha}} = \begin{cases} 1 + f_{\alpha\alpha} - \max(f_{ij}) & \max(f_{ij}) > 0 \\ 1 + f_{\alpha\alpha} & \max(f_{ij}) < 0 \end{cases} \quad \dot{\varepsilon}_{\alpha\alpha} > 0$$
$$\begin{cases} 1 - f_{\alpha\alpha} + \min(f_{ij}) & -\min(f_{ij}) > 0 \\ 1 - f_{\alpha\alpha} & -\min(f_{ij}) < 0 \end{cases} \quad \dot{\varepsilon}_{\alpha\alpha} < 0 \tag{A3-29}$$

An approximate formulation with ”smoothing” is used in the implementation. This is obtained using shape functions defined by $\tilde{\alpha}(x) \equiv \Phi^{\alpha}{}_{III}(x)$ and $\tilde{\beta}(x) \equiv 1 - \Phi^{\alpha}{}_{III}(x) = \Phi^{\alpha}{}_{III}(-x)$. In the first step the ”inner conditions” expressed in terms of $\max(f_{ij})$ and $\min(f_{ij})$ are approximated so that,

$$-\frac{1}{K}\frac{\partial f_{\alpha\alpha}}{\partial \varepsilon_{\alpha\alpha}} \approx \begin{cases} \tilde{a}(f_{ij}) = 1 + f_{\alpha\alpha} - \tilde{\alpha}\big(\max(f_{ij}) - \delta_f/2\big)\max(f_{ij}) & \dot{\varepsilon}_{\alpha\alpha} > 0 \\ \tilde{b}(f_{ij}) = 1 - f_{\alpha\alpha} + \tilde{\beta}\big(\min(f_{ij}) + \delta_f/2\big)\min(f_{ij}) & \dot{\varepsilon}_{\alpha\alpha} < 0 \end{cases} \tag{A3-30}$$

Thus, the influence from $\max(f_{ij})$ or $\min(f_{ij})$ is smoothly increased from $\max(f_{ij}) = 0$ and $-\min(f_{ij}) = 0$, respectively. In the next step the ”outer condition” acting on $\dot{\varepsilon}_{\alpha\alpha}$ is approximated using the same shape functions as defined above, which results in,

$$-\frac{1}{K}\frac{\partial f_{\alpha\alpha}}{\partial \varepsilon_{\alpha\alpha}} \approx \tilde{\alpha}(\dot{\varepsilon}_{\alpha\alpha})\tilde{a}(f_{ij}) + \tilde{\beta}(\dot{\varepsilon}_{\alpha\alpha})\tilde{b}(f_{ij}) \tag{A3-31}$$

Thus, the functions $\tilde{a}$ and $\tilde{b}$ are smoothly blended from $\dot{\varepsilon}_{\alpha\alpha} = -\delta_{\dot{\varepsilon}}/2$ to $\dot{\varepsilon}_{\alpha\alpha} = \delta_{\dot{\varepsilon}}/2$, at zero strain rate $-\frac{1}{K}\frac{\partial f_{\alpha\alpha}}{\partial \varepsilon_{\alpha\alpha}} = \big(\tilde{a} + \tilde{b}\big)/2$.

In order to prevent drift of the state variable $f_{\alpha\alpha}$ into "forbidden" states, defined by the set $\{\dot{\varepsilon}_{\alpha\alpha}, f_{ij}\}_0$, the evolution law is subjected to an additional condition given by,

$$\widetilde{\frac{\partial f_{\alpha\alpha}}{\partial \varepsilon_{\alpha\alpha}}}\left(\dot{\varepsilon}_{\alpha\alpha}, f_{ij}\right) = 0 \text{ for } \left(\dot{\varepsilon}_{\alpha\alpha}, f_{ij}\right) \in \left\{\dot{\varepsilon}_{\alpha\alpha}, f_{ij}\right\}_0 \tag{A3-32}$$

This is accomplished by introducing two additional shape functions $\tilde{\zeta}(x, y)$ and $\tilde{\xi}(x, y)$. The combined property when multiplying the two is that it becomes zero when $(x, y) \in \{\dot{\varepsilon}_{\alpha\alpha}, f_{\alpha\alpha}\}_0$. The new approximate state variable evolution equation becomes,

$$-\frac{1}{K}\frac{\partial f_{\alpha\alpha}}{\partial \varepsilon_{\alpha\alpha}} \approx \left[\tilde{\alpha}(\dot{\varepsilon}_{\alpha\alpha})\tilde{a}\left(f_{ij}\right) + \tilde{\beta}(\dot{\varepsilon}_{\alpha\alpha})\tilde{b}\left(f_{ij}\right)\right]\tilde{\zeta}(\dot{\varepsilon}_{\alpha\alpha}, f_{\alpha\alpha})\tilde{\xi}(\dot{\varepsilon}_{\alpha\alpha}, f_{\alpha\alpha}) \tag{A3-33}$$

The set defining the forbidden states can be expressed by the union of two subsets,

$$\left\{\dot{\varepsilon}_{\alpha\alpha}, f_{ij}\right\}_0 = \left\{\dot{\varepsilon}_{\alpha\alpha} > 0, f_{ij} < f^-\right\} \cup \left\{\dot{\varepsilon}_{\alpha\alpha} < 0, f_{ij} > f^+\right\} \tag{A3-34}$$

where

$$f^- = \max\left[\max\left(f_{ij}\right) - 1, -1\right] \quad \text{and} \quad f^+ = \min\left[\min\left(f_{ij}\right) + 1, 1\right] \tag{A3-35}$$

The shape functions are then defined by,

$$\tilde{\zeta}(\dot{\varepsilon}_{\alpha\alpha}, f_{\alpha\alpha}) = \max\left[\tilde{\beta}(\dot{\varepsilon}_{\alpha\alpha} + \delta_\varepsilon/2), \tilde{\alpha}\left(f_{\alpha\alpha} - \delta_f/2 - f^-\right)\right] \tag{A3-36}$$

$$\tilde{\xi}(\dot{\varepsilon}_{\alpha\alpha}, f_{\alpha\alpha}) = \max\left[\tilde{\alpha}(\dot{\varepsilon}_{\alpha\alpha} - \delta_\varepsilon/2), \tilde{\beta}\left(f_{\alpha\alpha} + \delta_f/2 - f^+\right)\right] \tag{A3-37}$$

Arkitektkopia AB, Bromma, 2019

SKB is responsible for managing spent nuclear fuel and radioactive waste produced by the Swedish nuclear power plants such that man and the environment are protected in the near and distant future.

skb.se